IONOSPHERIC THREATS TO THE INTEGRITY OF AIRBORNE GPS USERS

A DISSERTATION
SUBMITTED TO THE DEPARTMENT OF AERONAUTICS AND ASTRONAUTICS
AND THE COMMITTEE ON GRADUATE STUDIES
OF STANFORD UNIVERSITY
IN PARTIAL FULFILLMENT OF THE REQUIREMENTS
FOR THE DEGREE OF
DOCTOR OF PHILOSOPHY

Seebany Datta-Barua
April 2008

I certify that I have read this dissertation and that, in my opinion, it is fully adequate in scope and quality as a dissertation for the degree of Doctor of Philosophy.

(Todd Walter) Principal Co-Advisor

I certify that I have read this dissertation and that, in my opinion, it is fully adequate in scope and quality as a dissertation for the degree of Doctor of Philosophy.

(Per Enge) Principal Co-Advisor

I certify that I have read this dissertation and that, in my opinion, it is fully adequate in scope and quality as a dissertation for the degree of Doctor of Philosophy.

(Umran Inan)

Approved for the University Committee on Graduate Studies.

Abstract

The Global Positioning System (GPS) has both revolutionized and entwined the worlds of aviation and atmospheric science. As the largest and most unpredictable source of GPS positioning error, the ionospheric layer of the atmosphere, if left unchecked, can endanger the safety, or "integrity," of the single frequency airborne user. An augmentation system is a differential-GPS-based navigation system that provides integrity through independent ionospheric monitoring by reference stations. However, the monitor stations are not in general colocated with the user's GPS receiver. The augmentation system must protect users from possible ionosphere density variations occurring between its measurements and the user's.

This study analyzes observations from ionospherically active periods to identify what types of ionospheric disturbances may cause threats to user safety if left unmitigated. This work identifies when such disturbances may occur using a geomagnetic measure of activity and then considers two disturbances as case studies. The first case study indicates the need for a non-trivial threat model for the Federal Aviation Administration's Local Area Augmentation System (LAAS) that was not known prior to the work. The second case study uses ground- and space-based data to model an ionospheric disturbance of interest to the Federal Aviation Administration's Wide Area Augmentation System (WAAS). This work is a step in the justification for, and possible future refinement of, one of the WAAS integrity algorithms.

For both WAAS and LAAS, integrity threats are basically caused by events that may be occurring but are unobservable. Prior to the data available in this solar cycle, events of such magnitude were not known to be possible. This work serves as evidence that the ionospheric threat models developed for WAAS and LAAS are warranted and that they are sufficiently conservative to maintain user integrity even under extreme ionospheric behavior.

Acknowledgements

There are many people who have supported me on this journey. I humbly thank all of them for their help. My advisor Professor Per Enge I thank for allowing me both the opportunity to join the GPS lab at Stanford in the first place and the intellectual freedom to investigate an area of interest that borders other fields. I thank my advisor Dr. Todd Walter for encouraging my research interests and for being so approachable and available to discuss the research. I thank both Per and Todd for setting an example of brilliance and professionalism coupled with respect for others.

Thanks to Professors Umran Inan, Steve Rock, and Sarah Church for serving on my defense committee. I am grateful to Professor Inan also for providing insights and reviewing this dissertation. I appreciate Fiona Walter's comments and suggestions in reviewing this dissertation. Thanks in particular to Doug Archdeacon, Sherann Ellsworth, Dana Parga, Lynn Kaiser, Ralph Levine, Liza Julian, Robin Murphy, and Sally Gressens for their help in systems, financial, logistical, and academic administration.

The GPS lab members and alums have not only been good colleagues in helping me to improve the quality of my work, they have become good friends. Sam Pullen, Ming Luo, Jiyun Lee, Juan Blanch, Hiro Konno, Godwin Zhang, Alex Ene, Grace Gao, Sriram Rajagopal, Sherman Lo, Eric Phelts, Tsung-Yu Chiou, Lee Boyce, Dave De Lorenzo, Di Qiu, Shankar Ramakrishnan, Young Shin Park, Juyong Do, Jiwon Seo, Eui-ho Kim, Alan Chen, Alan Zorn, Sarah Atwater Abbott, Mike Koenig, Ung-Suok Kim, Sasha Mitelman, Takeyasu Sakai, Sharon Houck, Guttorm Opshaug, Chad Jennings, and Professors Jason Rife, Demoz Gebre-Egziabher, Shau-Shiun James Jan, Dennis Akos, Dave Powell, Jim Spilker, Boris Pervan, Penny Axelrad, Gabe Elkaim, and Brad Parkinson: thank you all. There are many more members of this GPS family who have touched my life than I can name here. I am grateful to them all.

Thanks to Patricia Doherty, Susan Delay, Attila Komjathy, Tony Mannucci, Eric Altshuler, and Professor Glen Mattioli for providing and processing data, as well as providing professional advice and mentoring. I thank the friends of the Aeronautics and Astronautics Department: Teresa Miller, Misty Davies, Jen Bower, Siina Haapanen, Paul Urbanczyk, and Kristof Richmond for their helpful feedback and for their friendship.

I appreciate the kindness of my cousin Pranami Dutta Mazumdar, my family friends Ron and Rukmini Pennathur Das, and my close friends Sonya Chang and Mandy Khoshnevisan for hosting me at their homes after late nights on campus. Thanks also to Sumita Pennathur, Tom Roberts, and Katrina Sostek for being great carpool buddies during early mornings and late nights to and from campus.

To my parents Lohit and Manjula Datta-Barua, I am grateful beyond words for all the personal sacrifices they have so willingly made in order to encourage me to strive and to make so many opportunities available to us. I thank my sister Indrany for her years of love and understanding, and wish her all the best in her endeavors. Howard, Elise, and Susannah Masur, thank you for always welcoming me into the family and encouraging me in my scholarly pursuits.

And to Jonathan, who understands the siren call of the intellectual pursuit, and the patience and persistence it requires: thank you for loving me and supporting me all these years.

Contents

List of Tables

List of Figures

Chapter 1

Introduction

1.1 Overview

This is a tale of two disciplines: landing airplanes and understanding the ionosphere. Although both were born in the early 1900s, they have followed fairly independent paths until recently. The incredible success of GPS as a navigational tool has brought them together as symbiotic fields of study. The use of GPS as a means of monitoring space weather has flourished [Coster *et al.*, 2003]. It has simultaneously emerged as a primary navigation aid for the aviation community.

The layer of the atmosphere known as the ionosphere is of great importance to civilian aviators using single-frequency GPS. It is the largest and most variable source of positioning error. Therefore, a greater understanding of the ionosphere is helpful to the aviation community in designing GPS-based navigation systems. At the same time, the specific safety-driven needs of aviators can motivate and give focus to the direction of ionospheric research.

The topics discussed in this work yield some surprising answers about ionospheric behavior with implications for how to deal with them safely for aviation. They also show some ionospheric behavior for which the underlying physical processes are not yet fully explained and modeled from beginning to end by the ionospheric community.

This chapter provides some background on the GPS-based navigation methods either in use or under development for the aviation community, discusses ionospheric behavior briefly, and summarizes the new insights brought to the fore in the remaining chapters of this work.

1.2 GPS Augmentation Systems: Navigation for Aviation

The Global Positioning System (GPS) is a prime example of a global navigation satellite system (GNSS) [Misra and Enge, 2006]. GPS consists of a constellation of satellites orbiting Earth and transmitting signals to ground-, sea-, air- and space-based receivers. The signal's special structure allows receivers to compute their position with few-meter-level accuracy, based on the transit time of the signal from multiple satellites. Though initially developed by the United States (US) Department of Defense as a military service, the civilian use of GPS has grown so rapidly that in a 1998 Presidential Decision Directive, it was named a "critical infrastructure" for the dazzling array of both technological advances and cross-disciplinary research it has enabled [Clinton, 1998].

The US Federal Aviation Administration (FAA) has led the way in developing GPS for use in the civil aviation community, through development and implementation of GPS augmentation systems ([Enge *et al.*, 1996] and [Enge, 1999]). These systems fall under two main categories: Space-Based (SBAS) and Ground-Based (GBAS). Whether a GBAS or SBAS, an augmentation system improves user accuracy by employing differential corrections from reference receivers at known locations. This general concept is called differential GPS (DGPS).

A civilian pilot using only GPS, or "stand-alone GPS," receives a spread-spectrum signal from the GPS satellites centered at the L1 frequency. Part of this GPS message includes a simple model of the error source discussed throughout this text, the "ionospheric delay" [ICD-GPS-200C, 1993]. With this model for the ionospheric error, a user can eliminate about 50% of his or her error [Feess and Stephens, 1987]. The premise behind a DGPS system is that a GPS reference station on the ground at a known location experiences nearly the same ionospheric delay error as the nearby DGPS user. By taking the difference between the range measurements of the user and reference station, the ionospheric error can be nearly eliminated.

While accuracy is a necessary condition for en route and precision approach navigation, there are additional performance parameters "beyond accuracy," including: integrity, availability, and continuity [Lee, 2005]. These requirements are outlined by Kelly and Davis [1994]. Briefly, integrity is a bound, or "error ellipse," on a position estimate that accounts for all possible error sources and fault modes. If no such bound can be provided, the user must receive a warning not to perform the maneuver. Integrity is an assurance to the user

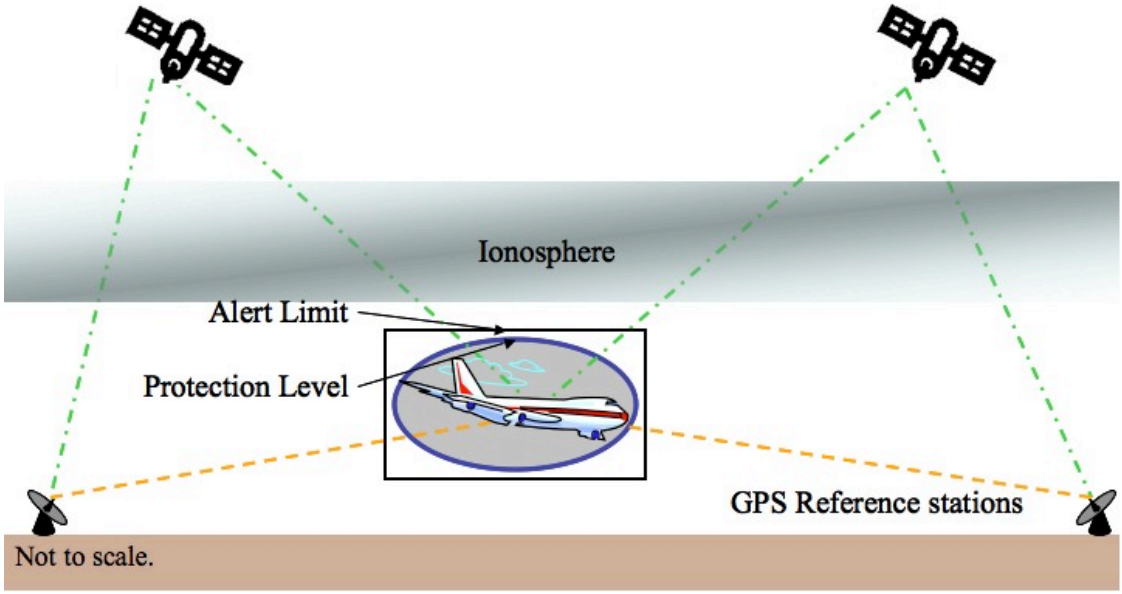

Figure 1.1: A GPS Augmentation System provides accuracy as well as integrity.

on how near to the true position the estimate can be guaranteed to be with an extremely high degree of confidence or a timely warning that no such guarantee can be made [Enge *et al.*, 1996]. Availability is the overall percent of time that a navigation service can be provided to the user. Continuity is a requirement that the service remain available to the user once he or she has started an approach to a runway. Jan [2003] provides a useful table that summarizes these requirements for different types of navigation service. Typically, the closer a maneuver brings an aircraft to a runway (i.e., the ground), the more stringent the requirements on integrity.

Integrity, a very high-confidence ellipse bounding the position estimate, is not provided by stand-alone GPS. Therefore, a GPS Augmentation System not only improves user accuracy by eliminating errors common to the user and reference stations but also provides integrity. To do this, the reference stations monitor the error sources — including satellite ephemeris, clock, ionosphere, and troposphere — and also place bounds on the uncertainty of these sources. Once the user receives these error bounds he or she may compute the overall Protection Level (PL), shown as a blue ellipse in Figure 1.1, in the vertical direction (VPL) and the horizontal direction (HPL). The user then compares these PLs to Alert Limits (ALs) in the vertical (VAL) and horizontal (HAL) directions. The VAL and HAL are pre-determined thresholds (black rectangle in Figure 1.1) ensuring safety for the particular

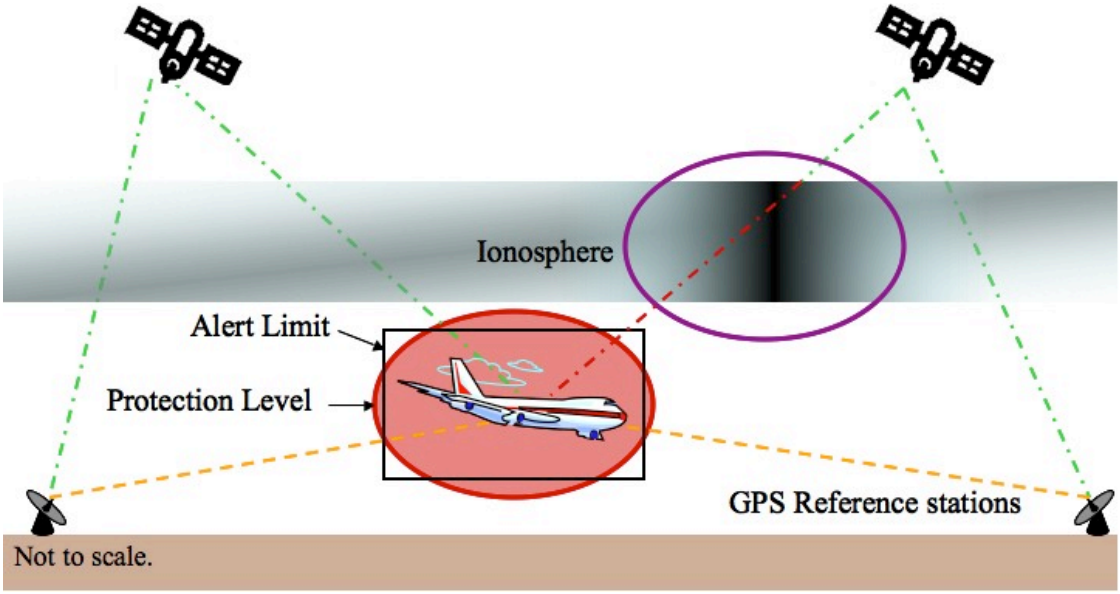

Figure 1.2: Even if the Augmentation System does not sense variations in the ionosphere that the user may be experiencing, the system must still provide integrity.

type of aircraft operation. For approach and landing procedures, the vertical limits are more stringent due to safety considerations.

Most of the time the ionosphere is smoothly and slowly varying (gray region in Figure 1.1). In some cases the ionosphere may not vary smoothly, though, as illustrated by the region circled in purple in Figure 1.2. In such situations, the ionospheric error suffered by the user may be very different from the error suffered at the ground station. For integrity, the augmentation system must still provide a PL that bounds the possible behavior of the ionosphere in this case. In some cases, bounding the error may result in a larger PL that then may exceed the AL. When the PL is greater than the AL, the service is not available.

Can the situation illustrated in Figure 1.2 really happen or is it merely an artificial construct, the stuff of aviation safety nightmares? This dissertation focuses on the behavior of the ionosphere in the worst-case conditions observed in the past solar cycle to show that such a circumstance *has* happened and to support the algorithms that ensure integrity for the FAA's SBAS and GBAS. The next sections discuss the architecture of these two systems in more detail.

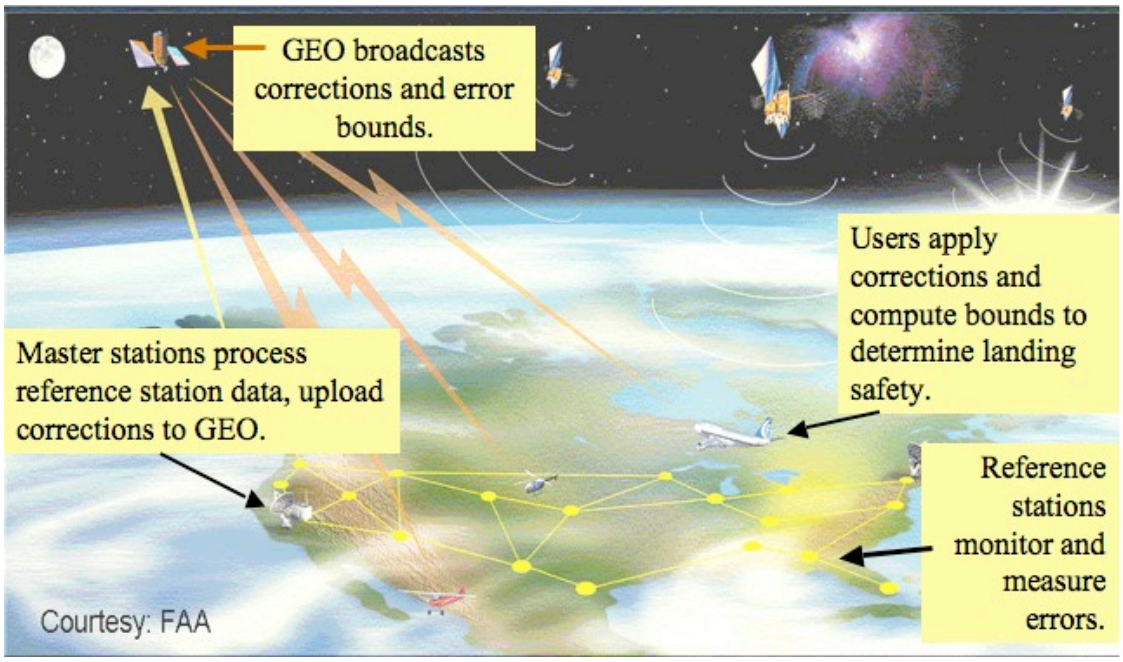

Figure 1.3: Wide Area Augmentation System (WAAS) architecture. Image courtesy FAA.

1.2.1 Space-Based Augmentation System

The Wide Area Augmentation System (WAAS) was commissioned by the Federal Aviation Administration (FAA) on 10 July 2003 [NSTB/WAAS Test and Evaluation Team, 2003]. Its function is to provide high-accuracy, high-integrity navigation service to aircraft operating within the conterminous United States (CONUS) as well as Canada and Mexico. The WAAS system is illustrated in Figure 1.3. Its architecture consists of: reference stations (WRS), each of which has three colocated dual frequency GPS receivers; master stations (WMS); geostationary satellites (GEO) that broadcast the corrections; and users who have WAAS-enabled GPS receivers. The primary function of WAAS is not only to provide error corrections to GPS measurements of users, but also to provide confidence bounds on those corrections. WAAS provides several levels of service for navigation both en route and while landing. Of these levels, the most stringent integrity is required for precision approach to a runway and is known as LPV (Lateral Precision with Vertical guidance).

Each WRS monitors the GPS satellite clocks and ephemeris and estimates the ionospheric delay to each satellite in view. These data are sent to the WMS for processing. Finally, the WMS uploads the error corrections and bounds to the GEO, which broadcasts

them over North America. The computation of these corrections and bounds is discussed in [GIVE-ADD, 2001]. The WAAS-enabled user applies the corrections and computes the VPL and HPL. The user compares the VPL to the VAL and the HPL to the HAL for the desired navigation service level to determine whether it is safe to perform the procedure. In this way, WAAS provides ionospheric corrections for users who may be as much as a few hundred kilometers away from the stations themselves [Klobuchar and Kunches, 2000]. In order to make real-time estimates of the ionosphere that can be quickly computed and broadcast with limited bandwidth, WAAS modeling of the ionosphere involves a number of simplifications and assumptions. These simplifications provide service with high availability, but there are instances when the model may not reflect actual ionospheric behavior, particularly because the data do not sample the anomalous aspects of the ionospheric behavior. This dissertation aims to understand the ionospheric conditions when such circumstances occur because these are the potential threats to integrity. A further goal is to mitigate any such residual threats.

1.2.2 Ground-Based Augmentation System

The FAA is also developing a Ground-Based Augmentation System (GBAS) known as the Local Area Augmentation System (LAAS). One of the functions of LAAS is to provide differential GPS (DGPS) corrections to users within tens of kilometers of a single airport [Enge, 1999]. Moreover, LAAS must meet the demands in accuracy, availability, and integrity needed for Category II/III landings. Many of the integrity issues have been studied in detail by Pervan [1996].

The LAAS architecture consists of the LAAS Ground Facility (LGF), which is a reference location equipped with four dual-frequency GPS receivers typically placed near the runway. As a DGPS system, it broadcasts ionospheric corrections and bounds to the user via a VHF data broadcast (VDB). The architecture is illustrated in Figure 1.4.

Bounds must be placed on the difference in ionospheric errors between an incoming aircraft and the LGF with minimal loss in availability. Because the ionosphere typically varies smoothly for a user and LGF who are typically separated by only a few kilometers, the nominal ionospheric error bound broadcast is only a few mm of delay difference per km of user-LGF separation distance [Lee *et al.*, 2006b].

This dissertation discusses the earliest findings that spatial decorrelation of the ionospheric error could be much much greater during geomagnetic storm conditions. This work

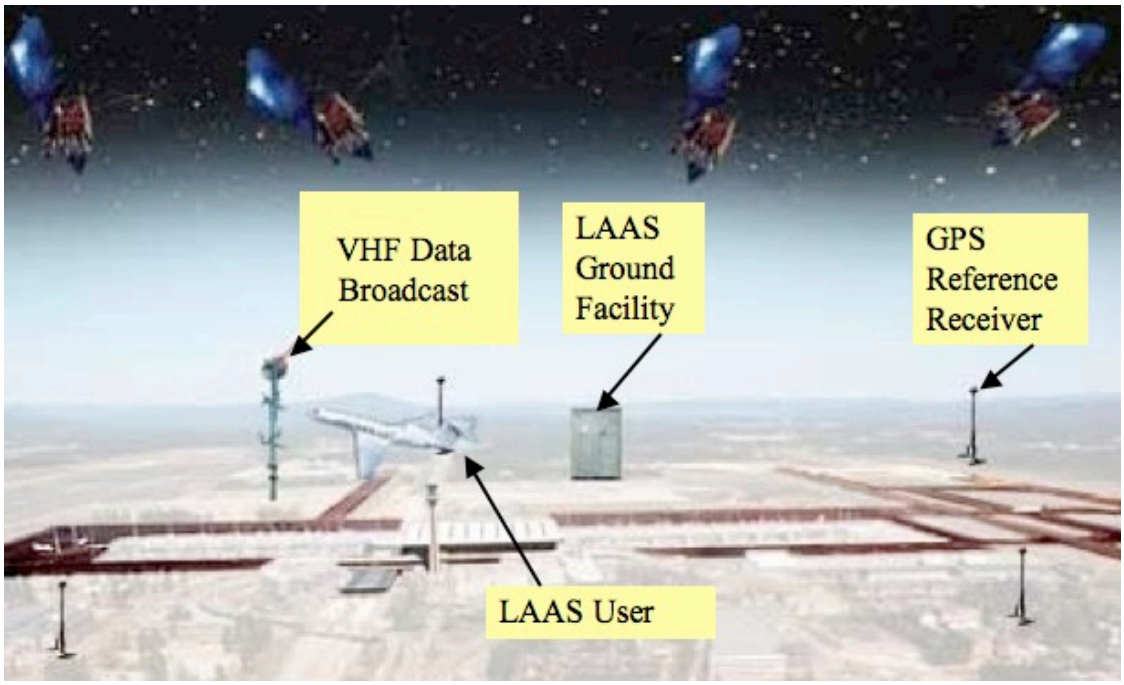

Figure 1.4: Local Area Augmentation System (LAAS) architecture. Image courtesy FAA.

has led to the development of a LAAS ionospheric model that treats the ionosphere delay as a linear function of the aircraft and user separation. The model of delay is a ramp parameterized by slope, width, maximum delay, and ground speed of the ramp ([Luo *et al.*, 2003] and [Luo *et al.*, 2004a]). The domains of the threat model parameters have been refined by Ene at al. [2005], and availability studies resulting from mitigating these threats have been pursued by Lee et al. [2006a].

1.3 Ionosphere and Space Weather

The ionosphere is a region of the upper atmosphere of Earth ionized primarily by solar ultraviolet (UV) radiation. It has no fixed boundaries but is typically considered to exist within 50–2000 km altitude [Tascione, 1994]. Due to the free electrons in this region, electromagnetic signals such as the GPS satellite broadcast are refracted as they traverse the ionosphere. The main effect of this refraction is that the signal arrival time is delayed with respect to an identical signal traveling through free space. The cumulative delay is proportional to the total electron content (TEC), which is the density of electrons integrated

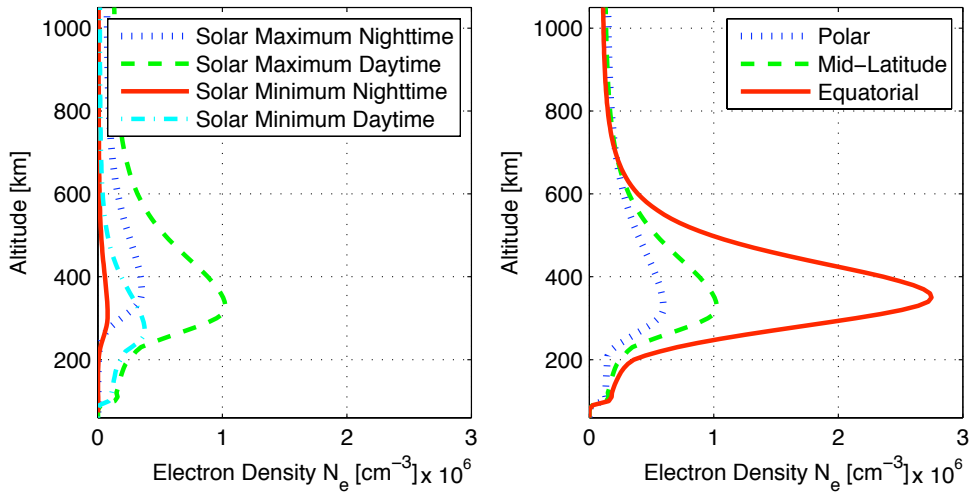

Figure 1.5: Typical ionosphere electron densities (x-axis) as a function of height (y-axis) for: (a) different times at mid-latitudes; (b) different latitude regions.

along the signal path. The several-meter-level error introduced by the ionosphere into the GPS signal is highly variable with location, season, and level of solar activity. Figure 1.5(a) shows ionosphere electron density as a function of height for a mid-latitude location at different times of day and solar cycle. The typical daytime altitudinal variation of electron density is illustrated for different latitudes in Figure 1.5(b).

The electrons and ions in the ionosphere form a plasma whose motion is dictated by magnetic fields. The dominant field is the geomagnetic field due to Earth's core. This field can be modeled as an Earth-centered dipole whose axis is tilted with respect to Earth's rotational axis. An eccentric dipole model, which displaces the dipole axis 500 km away from the center of Earth towards the longitude of Japan (away from the longitude of eastern Brazil), provides a better approximation [Schunk and Nagy, 2000].

Magnetic fields are also produced by currents in the region of Earth's space environment known as the magnetosphere. This region, from about two to several Earth radii away, includes the inner and outer radiation belts of energetic particles. Interactions of the magnetosphere with the solar wind affect the behavior of the ionosphere.

Solar activity can produce atypical magnetospheric, and hence ionospheric, conditions. X-ray flares and radio bursts can affect GPS navigation by appearing as broadband noise ([Cerruti, 2006] and [Carrano and Groves, 2007]). These effects threaten continuity of navigation service and are not discussed further in this work. The threats to integrity

have so far been related to phenomena known as coronal mass ejections (CMEs). A CME is a large quantity of magnetized charged particles blasted outward from the sun's lower atmosphere. An Earthward-directed CME may take several hours to a few days to reach the planet. Through processes not yet completely understood, the CME interacts with Earth's magnetosphere and ionosphere. The interaction distorts the shape of the magnetic field boundaries, injecting energetic particles and enhancing precipitation of particles onto the ionosphere. The data considered in this dissertation, particularly those involving the greatest integrity threats for WAAS and LAAS, were collected during storms following CME events that impacted Earth.

Additional effects of the ionosphere include bending of the signal during propagation, an effect which Brunner and Gu [1991] showed to introduce errors at the mm level. Scintillation is the rapid signal amplitude and phase fluctuation due to small-scale irregularities. Preliminary modeling by Pullen et al. [1998] and more recent studies using WAAS-certified receivers by Seo [2007] showed scintillation to be a possible continuity risk for WAAS and LAAS reference stations, which track the L2 frequency. These topics are beyond the scope of this dissertation, as the focus is on spatial variation in ionospheric error for aviation integrity.

1.3.1 Geographic Variability

Characteristic ionospheric behavior varies with geomagnetic latitude. The three primary zones are the equatorial zone ($< 20°$ magnetic latitude), mid-latitude zone (20–55°), and the polar region (55–90°). Each region is typified by certain behavior. Figure 1.6 illustrates the ionospheric zones, which follow geomagnetic latitude lines.

Polar Region

The polar region (55–90° latitude) includes the auroral band around 67° latitude. Typically, daytime ionospheric delays are low in this region due to lower solar UV ionizing flux. However, energetic events such as geomagnetic storms can feed particles into the auroral zone, causing it to extend toward the equator [Tascione, 1994].

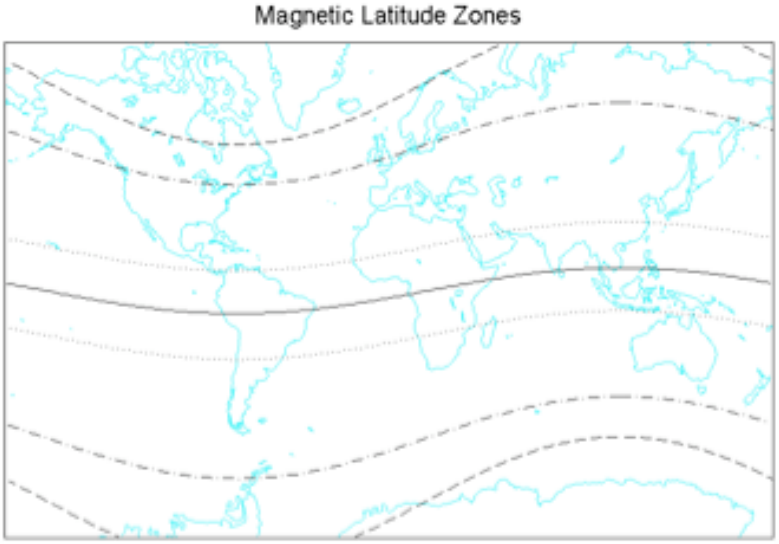

Figure 1.6: Magnetic latitude zones

Mid-Latitude Region

The ionosphere in geomagnetic mid-latitude regions (20–55° magnetic latitude) includes the US, Europe, and much of Japan and Australia. It tends to vary smoothly with time and location. This smooth variation allows for the simplicity of both the WAAS real-time ionosphere modeling and the LAAS assumption of highly correlated ionospheric delays between user and LGF during nominal conditions. However, during the worst solar-induced geomagnetic storms, the mid-latitude region contracts as the auroral oval expands equatorward and the equatorial electron content extends poleward. Ionospheric data from the mid-latitudes are the focus of the remaining chapters. An example of typical mid-latitude ionosphere is illustrated in Chapter 2. The emphasis in the remaining chapters is on extremely active ionosphere. Ionospheric scintillation can accompany small-scale irregular structure and has been observed in the mid-latitudes [Ledvina *et al.*, 2002]. It is known to occur more often at local dusk in equatorial and mid-latitude regions [Basu *et al.*, 2001]. However, this topic is not addressed further in this work because it does not impact integrity so much as continuity of navigation service.

Equatorial Region

The equatorial ionosphere covers Brazil, Saharan Africa, and much of India. It is characterized by high daytime ionospheric delays, and the equatorial, or Appleton, anomaly. This phenomenon is named an "anomaly" even though it happens daily because the highest delays do not appear at the geomagnetic equator, but are offset by 20–30°. The anomaly occurs due to the so-called fountain effect [Hanson and Moffett, 1966]. The fountain effect is a well-known daily occurrence in which an eastward E field produced by charge convection in a northward B field produces an E x B drift in the plasma that pushes electrons upward to higher altitudes on the dayside [Tascione, 1994]. From the high altitudes at the equator, they then drift to produce delay maxima around 20–30°.

In addition to the equatorial anomaly, the phenomenon known as the South Atlantic Anomaly also occurs in the equatorial region but is confined to the American sector. As a result of the apparent offset of the geomagnetic dipole axis away from the center of Earth and toward Japan, charged particles that travel along field lines of equal equatorial-field strength reach lower altitudes over the South Atlantic. In addition to being a cause of space-borne equipment malfunctions, the South Atlantic Anomaly has also been posited as a possible cause for the large storm-time delays seen in the American mid-latitude sector during the storms considered in subsequent chapters [Tsurutani *et al.*, 2004].

1.3.2 Temporal Variability

The primary source of the ionosphere is solar ionizing radiation. The ionosphere can be considered as basically fixed in the Sun-Earth frame with Earth rotating underneath it. For this reason the main periodicity is diurnal. Delays usually vary by an order of magnitude from night to day. The range errors experienced by a mid-latitude GPS receiver looking directly overhead would increase during the morning, peak shortly after noon, decrease during the evening as electrons recombine with ions, and then reach a nearly constant nighttime value of no more than a meter. Even so, the delays induced can vary by 25% at the one-sigma level from the monthly mean [Klobuchar, 1996].

There are seasonal variations observed in the ionosphere as well. It is also thought that geomagnetic storms caused by solar events may be more severe during the equinoxes [Kunches and Klobuchar, 2002]. The occurrence of solar events in turn are linked to the phase of the 11-year solar cycle. Solar activity waxes and wanes, as evidenced by the number

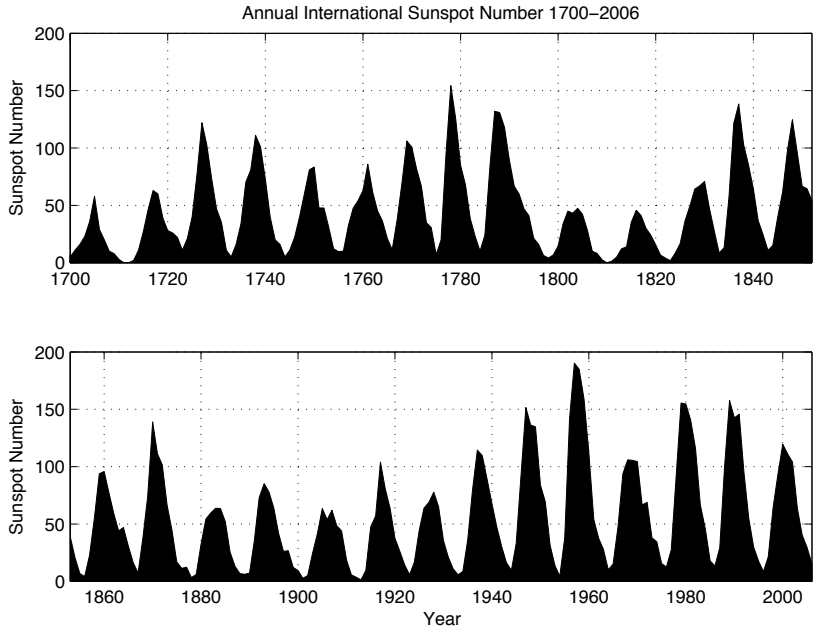

Figure 1.7: Sunspot number for the solar cycles through the current cycle 23.

of sunspots on the visible surface of the sun. Figure 1.7 shows the historical sunspot number through Solar Cycle Number 23, which peaked around 2000. During periods of maximum solar activity, solar energetic events such as coronal mass ejections (CMEs) are much more common than during solar minima. These are the periods on which the remaining chapters will focus, because they have produced the most anomalous ionospheric delays of the most recent solar cycle.

Solar activity produces geomagnetic activity, which then can induce ionospheric activity. The definition of a solar, geomagnetic, or ionospheric "storm" depends on the physical processes involved. For WAAS, a "storm" is defined operationally. In the cases to be examined, the severity of space weather activity was high enough and the impact on WAAS service availability significant enough that they were "storms" by both the physical and operational definitions. The connection between the physical and operational definitions of a storm will be made more directly in this work.

1.4 Previous Work

Geomagnetic Activity as a Measure of Regional Ionospheric Irregularity

Levels of geomagnetic activity have been monitored and quantified in a number of ways for decades. However, the relationship between geomagnetic activity and the relatively new application of GPS for aviation has not been fully addressed. Prior to this work, the Federal Aviation Administration commonly reported the geomagnetic index K_p alongside WAAS availability to try to identify days that would be ionospherically active over the US ([NSTB/WAAS Test and Evaluation Team, 2003], [NSTB/WAAS Test and Evaluation Team, 2004a], [NSTB/WAAS Test and Evaluation Team, 2004b], [NSTB/WAAS Test and Evaluation Team, 2004c], and [NSTB/WAAS Test and Evaluation Team, 2004d]). Kunches and Klobuchar [2002] studied geomagnetic storms using the geomagnetic index A_p to show a seasonal variation in geomagnetic activity. The geomagnetic measure D_{st} has historically been considered a measure of equatorial ring current activity more than a mid-latitude measure of activity [Campbell, 1996]. This thesis uses data to show that mid-latitude activity may have the equatorial region as its source, and that D_{st} can serve as a proxy for ionospheric activity over CONUS.

Ionospheric Modeling of Storms

Much more work has been done on ionospheric physics over the past hundred years than can be briefly reviewed here. Regional and global climatological models of the ionosphere such as the IRI model have been developed [Bilitza, 2001]. While the models do not predict transient activity, a great deal of effort has gone into understanding storms and is reviewed by Buonsanto [1999]. With the recent abundance of GPS total electron content (TEC) data, tomography has been used for imaging the ionosphere. Franke et al. [2003] have used TEC data to image the equatorial anomaly region. Tomographic inversion has also been performed for storm-time conditions ([Yin and Mitchell, 2005] and [Bust *et al.*, 2007]). As Hansen [2002] has pointed out, the most important challenge in using GPS TEC data is the lack of diversity in lines of sight. The low observability of vertical variations results in matrices that are ill-conditioned for inversion.

Additional evidence that the mid-latitude storm may be fed by equatorial events lies in recent studies discussing the possibility of a super-fountain effect: uplift caused by an unusually large electric field causing E x B drift to even higher altitudes than the usual

equatorial anomaly [Tsurutani *et al.*, 2004]. Even higher uplift takes plasma to a higher L-shell (surface of constant B field strength at the equator) such that recombination happens very slowly and the plasma drifts north and south along field lines to produce TEC enhancements at mid-latitudes.

Spatial Decorrelation of Delay

The aviation community and the ionospheric community have done studies to understand the ionosphere and assess its impact on GPS users. Early work in addressing the feasibility of GPS augmentation systems in the presence of the ionosphere was done by Klobuchar et al. [1993]. Prior to the maximum of Solar Cycle 23, the correlation of ionospheric delays was estimated to be high enough that correction estimates should be made within a few *hundred* kilometers of the user's line of sight [Klobuchar and Kunches, 2000]. This principle is the one that allows LAAS and WAAS to work in practice.

For LAAS, Christie et al. [1999] worked to quantify the decorrelation rate of the ionosphere for kilometer baselines, and estimated that the differential delay at L1 would be from a few to about 50 mm/km. The LAAS integrity bound calculation includes this term, and the need for a model to quantify anomalous behavior that might escape detection was not thought to be as high a priority for kilometer baselines.

Hansen et al. [2000] showed that the decorrelation of the ionosphere during typical conditions was 35 cm 1-sigma about a planar fit. The WAAS safety algorithms were designed to include what is effectively an ionosphere "Storm Detector" that would trigger during periods when reference station measurements indicated that spatial correlation of delays was low [Walter *et al.*, 2000]. In addition, the safety algorithms included offline quantification of the possible variations in delay between measurement locations, or "undersampling" [Sparks *et al.*, 2001]. A bound on undersampling is included in the WAAS Protection Level calculation during non-stormy conditions.

These algorithms were developed prior to the maximum of Solar Cycle 23. They performed with success during the major storms of the past few years ([Doherty *et al.*, 2004] and [Komjathy *et al.*, 2003]). However, the spatial variations observed from the storms showed localized regions of high decorrelation. These were included in the offline analysis to update the undersampled threat model, but the service availability was drastically degraded even during nominal days. The Storm Detector was extended into an "Extreme Storm Detector" (ESD) that would cut availability over an eight-hour period after the last

observed vestiges of a storm ([Sparks *et al.*, 2005] and [Pandya *et al.*, 2007]). In this way the local high decorrelation would not affect availability during nominal periods. The eight-hour hysteresis of the ESD was driven by the duration of a localized TEC enhancement that is studied in detail in this work.

The goal of the model presented here is twofold. It is an important step in understanding the ionospheric physical processes that created the anomalous region and whether they are consistent with current ionospheric theory. It is also a step in assessing the duration of the ESD hysteresis. Estimating electron altitude allows for an estimate of ion-electron recombination rate, which in turn can be used to validate the eight-hour hysteresis or revise it. Understanding why the anomaly was ground-fixed for a several-hour period can allow the argument to be made that reference stations would likely sample the region. In this way, the ESD hysteresis could be revised downward in the future.

1.5 Contributions

The contributions of this work can be summarized by the classic questions of the investigative reporter: "Who, What, Where, When, Why, and How?" This chapter addressed the question of WHO is concerned with anomalous ionospheric behavior. The issue of WHAT data are available to sense the ionosphere is the topic of Chapter 2. Chapter 3 discusses WHAT ionospheric behavior has been observed and WHY it poses a threat to Augmentation System user integrity. The contributions of this work to understanding the impact of the ionosphere for Augmentation Systems can be outlined as follows:

1. WHEN integrity threats can occur. As discussed in Chapter 4, 5–10 days of interest from 2000–07 and their place in a 50-year historical context were identified for their impact on WAAS and LAAS. The work presented here illustrates the connection between the geomagnetic index D_{st} and anomalous ionosphere over the US.

2. HOW MUCH ionosphere error can vary between user and LAAS reference station. Chapter 5 shows the first evidence that the TEC spatial rates of change across distances less than 100 km were two orders of magnitude higher during storms than was anticipated prior to the work.

3. HOW to find electron altitude. Ground-based sensors are sensitive to horizontal but not vertical gradients, so Chapter 6 integrates data from multiple sensors both from

satellites and ground stations to understand both horizontal and vertical electron density variation of localized enhancement. This work takes advantage of space-borne TEC data available to address the challenge with tomographic reconstruction of the ionosphere.

4. WHERE the electrons in a TEC enhancement that could go unsampled by WAAS reference stations are. Three-dimensional electron density modeling of an integrity threat contributes to validation of WAAS integrity-maintaining algorithms. The model indicates uplift of the electron density peak in the anomalous region of the ionosphere. This may have implications for the WAAS storm detection algorithms. The modeling is also discussed in Chapter 6.

The question of WHY such behavior in the ionosphere occurs is beyond the scope of this text, and is the topic of ongoing ionospheric research. This final question illustrates the symbiotic relationship that has emerged. Issues for the GPS aviation community can provide useful directions for ionospheric research, just as the ionospheric community can provide a greater understanding of the phenomena for which the GPS aviation world must be prepared.

Chapter 2

Sensing the Ionosphere

2.1 Overview

This chapter discusses a number of tools for sensing the ionosphere and the magnetosphere to which it is coupled. These are data that will be used throughout subsequent chapters. Other methods of measuring the ionosphere via Faraday rotation, Thomson scattering, Langmuir probes, incoherent scatter, or ionospheric heating are not discussed since they are not directly used. For more information on these techniques the reader may wish to consult Bittencourt [2004], Schunk and Nagy [2000], or Walt [1994].

Section 2.2 involves remote sensing of the ionosphere via ionosondes, which reflect radio waves off the bottom side of the ionosphere to measure electron density, N_e, at specific altitudes. In Section 2.3 the trans-ionospheric radio propagation of signals is discussed. Such measurements, including dual-frequency GPS, give the total electron content (TEC), i.e. the number density of electrons, N_e, integrated along the signal path.

The ground GPS network data that will be used and the processing involved are reviewed in Section 2.3.1 for: Wide Area Augmentation System (WAAS); Continuously Operating Reference Stations (CORS); International GNSS Service (IGS); and the Caribbean-North American Plate Experiment (CANAPE). Section 2.3.3 discusses remote sensing of the ionosphere with sensors aboard the orbiting satellites SAC-C and Jason. SAC-C measures TEC with a dual-frequency GPS receiver, in the same way that the ground-based receivers do. Jason also measures TEC, but does so with a dual-frequency altimeter.

Section 2.4 introduces a measure of geomagnetic activity, D_{st}, that indicates the worldwide level of magnetospheric activity due to currents flowing in the ionosphere and plasmasphere. This index is useful since it can serve as a proxy for ionospheric activity during periods that predate GPS sampling. Section 2.5 shows the periods of WAAS service coverage that were reported from 2003–2005 that will be compared to D_{st} in Chapter 4.

2.2 Electron Density

The ionosphere is the layer of the atmosphere from 50 km altitude upwards consisting of a weakly ionized plasma [Tascione, 1994]. The ionosphere has several layers - D, E, F1, and F2 - that are characterized by the ion and molecular chemistry dominant at those altitudes. The highest electron density occurs in the highest-altitude F2 layer. Figure 1.5 in the previous chapter shows typical electron densities, N_e, as a function of altitude (on the y-axis). The F2 layer occurs at the global density maximum on each curve, and is typically found at 300–450 km height. The region above 1000 km is generally referred to as the plasmasphere, in which H+ is the prevalent ion. This layer rotates with Earth, due to friction [Tascione, 1994].

Each point in a cold plasma such as the ionosphere has a characteristic frequency, the plasma frequency, f_{pe}, that depends on the local number density of electrons, N_e, in the medium:

$$f_{pe} = \frac{1}{2\pi}\sqrt{\frac{N_e e^2}{m_e \epsilon_0}} \tag{2.1}$$

The remaining terms in the plasma frequency are constants in SI units: electron charge, e, electron mass, m_e, and permittivity of free space, ϵ_0. Essentially the plasma as a whole acts as a spring-mass system. A small displacement of electrons from ions causes the electrons to oscillate at this characteristic frequency [Bittencourt, 2004].

A plasma subject to a magnetic field B has another characteristic frequency, called the gyro or cyclotron frequency. The gyro-frequency of electrons in a magnetic field is:

$$f_g = \frac{eB}{2\pi m_e} \tag{2.2}$$

Electromagnetic waves passing through the ionosphere are refracted. Neglecting collisions, their speed of propagation is governed by the Appleton-Hartree equation for the

phase index of refraction for a right-hand circularly polarized wave (e.g., GPS) [Klobuchar, 1996]:

$$n_\phi^2 = 1 - \frac{X}{1 - \frac{Y^2 sin^2\theta_B}{2(1-X)} - (\frac{Y^4 sin^4\theta_B}{4(1-X)^2} + Y^2 cos^2\theta_B)^{\frac{1}{2}}} \tag{2.3}$$

The angle between the magnetic field and the propagation direction is θ_B, and X and Y are given by:

$$X = (\frac{f_{pe}}{f})^2 \tag{2.4}$$

$$Y = \frac{f_g}{f} \tag{2.5}$$

In the expression for X in Equation (2.4), the electron plasma frequency f_{pe} is given by Equation (2.1). The gyro-frequency f_g in the expression for Y is given by Equation (2.2).

The appearance of the signal frequency f in Equation (2.3) means that the ionosphere is dispersive, so that different frequencies travel at different speeds. The Appleton-Hartree equation (2.3) is a beautiful closed-form expression of the dispersion relation in a cold, collisionless, magnetized plasma such as the ionosphere. As a model for ranging or remote sensing, though, it is unwieldy. For this reason simplifications are made through a variety of approximations as summarized in [Datta-Barua *et al.*, 2006] to arrive at:

$$n_\phi^2 = 1 - (\frac{f_{pe}}{f})^2 \tag{2.6}$$

This means that, to first order, signals of frequency f will be reflected at the point where $f = f_{pe}$. Signals with frequencies higher than f_{pe} will continue to propagate.

Measurements of the electron density are made with RF signals below and up to f_{pe}. Ionospheric sounders, or ionosondes, are ground-based active sensing devices that transmit signals at a range of frequencies f vertically to the ionosphere. The signal propagates upward through increasing plasma density until $f_{pe} = f$. At this point the signal is reflected back toward Earth. The ionosonde receives the reflected signal, and estimates the height at which the plasma density corresponding to $f_{pe} = f$ occurred based on the two-way signal transit time [Schunk and Nagy, 2000].

A number of ionosondes are located worldwide. Their data are available at the Space

Table 2.1: Locations of ionosonde data used.

Air Force Base (AFB)	Location Description	Geographic Lat (° N)	Geographic Lon (° E)
Ramey	50 km west of Arecibo, Puerto Rico	18.5	292.8
Eglin	panhandle of Florida	30.4	273.3

Physics Interactive Data Resource (SPIDR) online [National Geophysical Data Center, 2005]. Data from two ionosondes are used in this work. The geographic coordinates are shown in Table 2.1. Both are part of the Digital Ionospheric Sounding System run by the US Air Force's Air Weather Service to update the Parameterized Real-Time Ionospheric Specification Model [Buchau *et al.*, 1993]. Data are provided to the general scientific community through the SPIDR website run by the National Oceanic and Atmospheric Administration (NOAA). The digital ionosonde is based on the model developed at the University of Massachusetts Lowell and is identical to the Digisonde 256 (Reinisch [1986] and [1993]).

The ionosondes provide estimates of electron density maxima of each layer and the estimated altitude at which that density occurred, as a function of time. In this work, the F2 layer maximum electron density, N_{mF2}, and the altitude of the F2 peak, h_{mF2}, as a function of time are considered in Chapter 6.

2.3 Total Electron Content

Trans-ionospheric radio waves are those whose frequency exceeds the plasma frequency given in Equation (2.1) at the point of maximum density. The GPS signals at the L1 frequency (f_1 = 1575.42 MHz), L2 frequency (f_2 = 1227.60 MHz), and L5 frequency (f_5 = 1176.45 MHz), are trans-ionospheric signals. These waves do not pass through unaffected, but are refracted.

Taylor expansion reduces Equation (2.6), which itself was a simplification of the Appleton-Hartree equation (2.3), to the following even simpler expression:

$$n_\phi = 1 - \frac{1}{2}X \tag{2.7}$$

Phase velocity is given by (2.7), and group velocity by [Jackson, 1999]:

$$n_\rho = n_\phi + f\frac{dn_\phi}{df} \tag{2.8}$$

$$= 1 + \frac{1}{2}X \tag{2.9}$$

Bending also occurs but is much less significant, so it is neglected for the remainder of this discussion [Klobuchar, 1996]. From Equations (2.1) and (2.4) it can be seen that this index of refraction varies as the electron density N_e and the inverse of the square of the signal frequency f. Ranging with GPS by estimating transit time relies on the assumption that the signal propagates at the speed of light c. However, the cumulative effect of the index of refraction is to delay the signal, or increase the apparent path length:

$$I_s = \int_{rx}^{sv} (n_\rho - 1)\, dl \tag{2.10}$$

Substituting Equations (2.1), (2.4), and (2.9) into Equation (2.10) using MKS units, the delay in terms of additional meters for signal of frequency f Hz becomes:

$$I_s = \frac{40.3}{f^2}\int_{rx}^{sv} N_e\, dl \tag{2.11}$$

$$= \frac{40.3}{f^2} TEC \tag{2.12}$$

In this expression, the constants from Equation (2.1) yield 40.3 $\frac{m^3}{s^2}$. The integral of the electron density along the raypath is known as the total electron content (TEC), and is in units of m^{-2}. The signal delay, I_s, is proportional to the TEC and inversely proportional to the square of the signal frequency f. Often total electron content is measured in TEC units (TECU). One TECU is defined as follows:

$$1\, TECU = 10^{16}\, m^{-2} \tag{2.13}$$

From Equation (2.12) 1 m of range delay I_s at L1 can be shown to correspond to 6.13 TECU:

$$1\, m\, at\, L1 \times \frac{f_1^2}{40.3} = 6.13\, TECU \tag{2.14}$$

This proportionality between I_s and TEC is the key to making measurements of the ionosphere with trans-ionospheric signals. Throughout this text, "TEC" and "slant delay at L1" are used interchangeably since they are proportional. Unless otherwise specified, "slant delay" refers specifically to the slant delay at L1. The slant delays at L2 and L5 will be larger since the frequency f in Equation (2.12) is lower.

A GPS receiver produces two measurements at each frequency when it receives the signal from a satellite. One is the pseudorange, ρ, and the other is the phase of the carrier sinusoid, ϕ. The pseudorange is so named because it is not the user's true range to a single GPS satellite, but an estimate of the transit time of the signal based on the phase of the digital code riding on the carrier signal. A single frequency (civilian) receiver gives measurements ρ_1 and ϕ_1. A dual frequency receiver, which uses codeless or semi-codeless tracking of the L2 (currently military) signal, also supplies ρ_2 and ϕ_2 at frequency L2. These measurements and the error sources in them, including the ionosphere range delay I_s, can be modeled as:

$$\rho_1 = r + I_s + \epsilon_{\rho_1} \tag{2.15}$$

$$\rho_2 = r + \gamma(I_s + IFB + \tau_{gd}) + \epsilon_{\rho_2} \tag{2.16}$$

$$\phi_1 = r - I_s + N_1\lambda_1 + \epsilon_{\phi_1} \tag{2.17}$$

$$\phi_2 = r - \gamma(I_s - IFB - \tau_{gd}) + N_2\lambda_2 + \epsilon_{\phi_2} \tag{2.18}$$

$$\gamma = (f_1/f_2)^2 \tag{2.19}$$

In these equations, r represents the true range plus the non-dispersive bias errors due to the receiver clock, satellite clock, and troposphere. The ionosphere delay at L1 is I_s and is proportional to the delay at L2 by factor γ. The frequencies of the L1 and L2 signals are f_1 and f_2, respectively. The phase measurements, ϕ_1 and ϕ_2, contain an unknown integer number, N_1 and N_2, of wavelengths λ_1 and λ_2. The noise term on each observable is indicated by a subscripted ϵ.

With measurements at one frequency, for example L1, an estimate of the ionosphere, I_{ccd}, can be formed based on the divergence of the carrier from the code:

$$I_{ccd} = \frac{\rho_1 - \phi_1}{2} \tag{2.20}$$

$$= I_s - \frac{N_1\lambda_1 - \epsilon_{\rho 1} + \epsilon_{\rho 2}}{2} \tag{2.21}$$

In practice the code-carrier divergence is rarely used to measure the absolute delay introduced by the ionosphere because it contains the carrier integer ambiguity, N_1. It is also a noisy estimate due to the term $\epsilon_{\rho 1}$, which is much greater than $\epsilon_{\rho 2}$.

With measurements at two frequencies, I_s can be estimated directly. The dual frequency estimate of the ionosphere is formed from the GPS observables as:

$$\begin{aligned} I_\rho &= \frac{\rho_2 - \rho_1}{\gamma - 1} && (2.22)\\ &= I_s + \frac{\gamma}{\gamma - 1}(IFB + \tau_{gd}) + \frac{1}{\gamma - 1}(\epsilon_{\rho_2} - \epsilon_{\rho_1}) && (2.23)\\ I_\phi &= \frac{\phi_1 - \phi_2}{\gamma - 1} && (2.24)\\ &= I_s + \frac{\gamma}{\gamma - 1}(IFB + \tau_{gd}) - \frac{1}{\gamma - 1}(N_2\lambda_2 - N_1\lambda_1) && (2.25)\\ &\quad -\frac{1}{\gamma - 1}(\epsilon_{\phi_2} - \epsilon_{\phi_1}) && (2.26) \end{aligned}$$

The estimate of the ionosphere formed from the code phase does not contain the unknown integer number of cycles at L1, N_1, and at L2, N_2, but it is noisy because $\epsilon_{\rho_i} >> \epsilon_{\phi_i}$. Both estimates, I_ρ and I_ϕ, contain the receiver interfrequency bias, IFB. The hardware bias unique to each satellite, τ_{gd}, is also present in both estimates and must be removed [Wilson *et al.*, 1999].

Using dual-frequency data involves estimating and removing the nuisance biases and noise. Different data sets that are used throughout have different processing methods. They are reviewed here. In general, the final estimate of the slant delay at L1 is a function of both the code estimate and the carrier estimate:

$$\tilde{I}_s = f\left(I_\rho, I_\phi\right) \tag{2.27}$$

2.3.1 Ground-Based GPS Network Data

1. WAAS

   Ionospheric data, known as "supertruth," have been obtained for the past few years for the Conterminous United States (CONUS) region from the Wide Area Augmentation System (WAAS) network, which had twenty-five ground stations (WRS) at the time of the data analyzed in this work. Figure 2.1 shows the locations of the WRS at

the time of data collection. Each ground station has three dual-frequency receivers, allowing for a direct measurement of the ionospheric delay. The raw receiver data is first conditioned into "truth" by post-process leveling of carrier to the code to remove integer ambiguities N_1 and N_2, satellite bias τ_{gd}, and receiver biases IFB. In Chapter 5, the data from each receiver at two WRSs will be analyzed.

WAAS's redundancy allows for voting to remove possible artifacts due to problems on individual receivers. The voting technique is to choose the median measurement at each epoch and define a tight bound on that value. If the other two receivers' measurements do not fall within that bound, an estimate of the TEC for that epoch is not made available. Supertruth is the final result of the whole process. Supertruth data is provided at 5-second intervals, but is decimated as appropriate for computational ease. A list of the supertruth data sets that are used herein at 100-second intervals is shown in Table 2.2. Additionally, in Chapter 5 data at 10-second intervals are analyzed.

2. CORS

   The US National Geodetic Survey makes data publicly available from a network of Continuously Operating Reference Stations (CORS). The data collected from these stations during the 29–31 October 2003 storm have been assimilated and leveled by the use of the Global Ionospheric Mapping (GIM) software at NASA's Jet Propulsion Laboratory (JPL). With the additional use of the publicly available International GNSS Service (IGS) station data worldwide, GIM estimates and removes satellite and receiver interfrequency biases to provide high precision ionosphere measurements. The processing is described in detail by Komjathy et al. in [2002] and [2003]. The data are provided at 5-minute intervals.

3. IGS

   The International GNSS Service (IGS) is a project providing GPS data and products worldwide. It is a service of the International Association of Geodesy, developed in the 1990s to provide high precision and accuracy information on GPS orbits, clocks, and more [Dow *et al.*, 2005]. Dual frequency GPS measurements from hundreds of

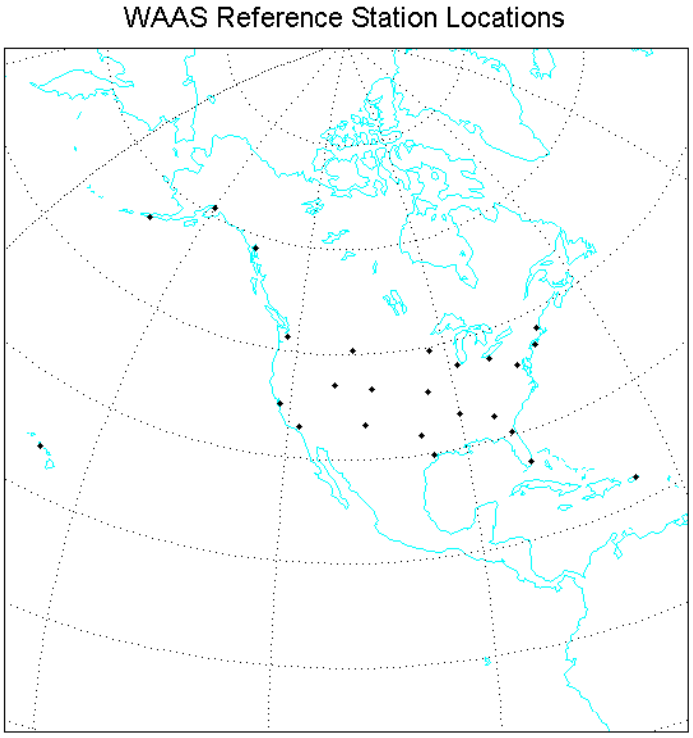

Figure 2.1: Map of North America indicating location of WAAS Reference Stations (WRSs) for data sets used.

Table 2.2: Summary of Supertruth Data Sets

Data Set	Year (yyyy)	Mon (mm)	Day(s) (dd)	Data Set	Year (yyyy)	Mon (mm)	Day(s) (dd)
1	2000	01	11	21	2002	04	18
2	2000	01	22	22	2002	04	20
3	2000	02	12	23	2002	05	23
4	2000	03	26–27	24	2002	08	23
5	2000	04	05–08	25	2002	09	04
6	2000	04	24	26	2002	09	07–08
7	2000	05	24–25	27	2002	09	11
8	2000	06	06–08	28	2002	10	01–02
9	2000	07	02	29	2002	10	04
10	2000	07	15–16	30	2002	11	21
11	2000	08	11–12	31	2003	05	29–31
12	2000	09	17–18	32	2003	06	01
13	2000	11	29	33	2003	06	18
14	2001	03	20	34	2003	07	12
15	2001	03,04	31, 01	35	2003	08	18
16	2001	04	11	36	2003	10	28–31
17	2001	10	03	37	2003	11	20–22
18	2001	10	21–22	38	2004	07	26–27
19	2001	11	05–06	39	2004	11	07–10
20	2001	11	24	40	2005	01	22

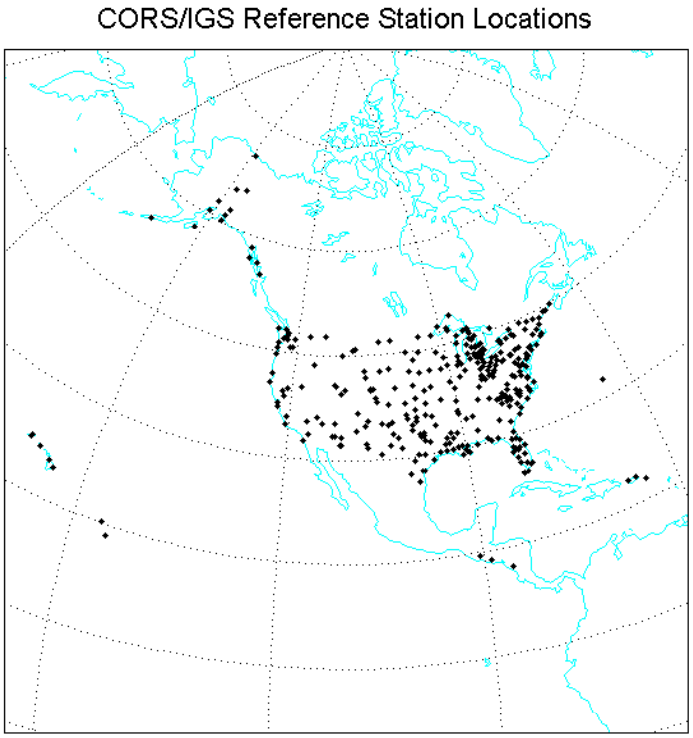

Figure 2.2: Map of North America indicating location of CORS and IGS Reference Stations for data sets used.

stations around the world are publicly available for download from the web. In this work, data from stations in Mexico and Central America are used. They are processed simultaneously with the CORS network data described above. The Kalman-filter-based GIM processing estimates and removes the satellite bias, τ_{gd}, and the receiver interfrequency biases, IFB. The combined CORS and IGS networks provide TEC data from almost 400 stations, shown in Figure 2.2. The IGS data are provided every 5 minutes along with the CORS data, with processing by Komjathy [2005].

4. CANAPE

   Additional GPS data from 12 stations in the Caribbean are provided by Dr. Glen Mattioli at the University of Arkansas, from the Caribbean-North American Plate

Boundary Experiment (CANAPE) effort. The code-leveled carrier phase measurement of the ionosphere is computed from the dual frequency data in the receiver-independent exchange (RINEX) format. The interfrequency and inter-data-set biases were initially removed by leveling each line of sight (LOS) to the nearest CORS/IGS station, also located in the Caribbean. LOSs with data at 19:00–07:00 EST (nighttime) are leveled to nighttime values first, and any LOSs without data at this time are leveled using their tracks from 07:00– 19:00 EST (daytime). This method disregards the fact that the receiver bias must be common among LOSs to a single receiver and that the satellite bias must be common among LOSs to a single satellite. An alternate method of leveling interfrequency biases, taking this coupling of biases into account, was attempted as described by Hansen [Hansen, 2002]. However, neither method ultimately showed sufficient consistency with the separately processed CORS/IGS and WAAS data to yield realistic contour maps. Since the main goal in leveling the biases is to be able to combine this data set with the data of CORS, IGS, and WAAS, ultimately this set was also processed at JPL with the GIM software.

2.3.2 Mapping TEC via the Thin Shell Model

Once the estimates of slant delay at L1, $\tilde{I}_s$, are obtained by removing the biases between receivers, a method for comparing measurements made at different viewing angles is needed. The raypath to a low elevation satellite passes through more ionosphere than the raypath to a satellite at zenith. Even if the electron density variation with altitude were identical at every latitude and longitude, the low elevation LOS would still have a significantly higher delay than the zenith raypath.

The most common way to account for apparent variations in TEC due to geometry is to model the ionosphere as a thin shell. Nearly all of the electrons are assumed to be concentrated within a single layer, or shell, of infinitesimal thickness at a chosen altitude, h_{iono}. Figure 1.5 of the electron density profile shows that the F2 layer contains the bulk of the electrons, so that typically the thin shell altitude is chosen to be at the height of the F2 density peak, usually 350–450 km. The concept of the thin shell is illustrated in Figure 2.3. The gray region of varying darkness represents the ionosphere, which has a thickness and a varying electron density. The thin shell is drawn as the white line through the region of greatest electron density, and is located at height h_{iono}.

With the thin shell assumption, each slant TEC measurement, $\tilde{I}_s$, has corresponding

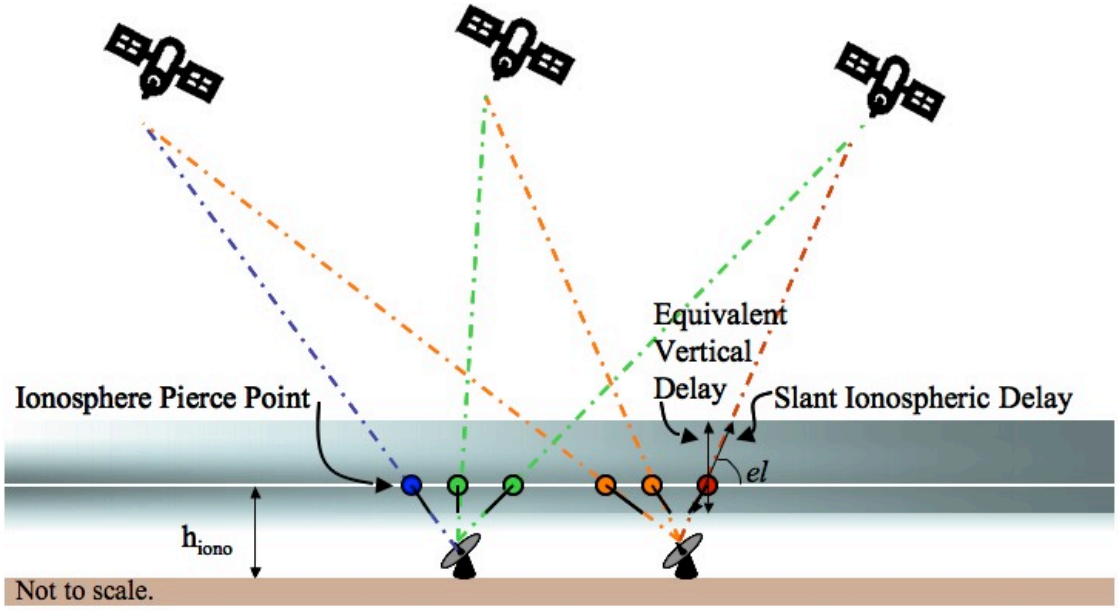

Figure 2.3: Illustration of how each equivalent vertical TEC $\tilde{I}_v$ measurement is mapped to a single point for comparison among different lines of sight.

equivalent vertical TEC, $\tilde{I}_v$. The equivalent vertical range delay is what the electron content would be for a vertical raypath passing through the thin shell at the same location as the actual LOS. The location at which the actual raypath reaches the altitude h_{iono} is known as the ionosphere pierce point (IPP).

The equivalent vertical delay, $\tilde{I}_v$, is computed from the GPS slant TEC measurements, $\tilde{I}_s$, by dividing by the mapping function in Equation (2.29) [Hansen, 2002]:

$$\tilde{I}_v = \frac{\tilde{I}_s}{M(el)} \tag{2.28}$$

$$M(el) = \frac{1}{\cos\left(\arcsin\left(\frac{R_E\cos(el)}{(R_E+h_{iono})}\right)\right)} \tag{2.29}$$

In Equation (2.29) R_E is the radius of Earth and el is the elevation of the satellite. The obliquity factor, M, varies from 1 for satellites at zenith to about 3 for those viewed from the ground at low elevation.

Once a measurement from each receiver-satellite pair is converted to equivalent vertical, it can be associated with the location of the IPP, for the purposes of visualizing the geographic variation of TEC. Given the latitude and longitude (λ_r, θ_r) of the receiver and the azimuth and elevation angles (az, el) of the satellite being tracked, the latitude and longitude of the IPP can be obtained from a sequence of rotation matrices. Following the notation of Misra and Enge [2006], let the angle between the line of sight vector and the local vertical at the IPP be ζ':

$$\zeta' = \arcsin\left(\frac{R_E cos(el)}{R_E + h_{iono}}\right) \tag{2.30}$$

In this expression, R_E is the equatorial radius of Earth. Then the Earth-centered angle, A, between the receiver and the IPP is given by:

$$A = \pi/2 - \zeta' - el \tag{2.31}$$

Define a coordinate frame whose z-axis is the local vertical at the IPP. Without loss of generality, the y-axis is defined such that the receiver lies in the y-z plane. The x-axis completes the right-handed axes. The rotation matrices T_1 and T_2 are applied to express a vector in an East-North-Up (ENU) frame local to the receiver. The matrix T_3 then expresses this vector in an ENU frame local to the point $(\lambda, \theta) = (0, \theta_r)$.

$$T_1 = \begin{pmatrix} 1 & 0 & 0 \\ 0 & cosA & sinA \\ 0 & -sinA & cosA \end{pmatrix} \tag{2.32}$$

$$T_2 = \begin{pmatrix} cos(az) & sin(az) & 0 \\ -sin(az) & cos(az) & 0 \\ 0 & 0 & 1 \end{pmatrix} \tag{2.33}$$

$$T_3 = \begin{pmatrix} 1 & 0 & 0 \\ 0 & cos(\lambda_r) & sin(\lambda_r) \\ 0 & -sin(\lambda_r) & cos(\lambda_r) \end{pmatrix} \tag{2.34}$$

$$\begin{pmatrix} e \\ n \\ u \end{pmatrix} = T_3 T_2 T_1 \begin{pmatrix} 0 \\ 0 \\ 1 \end{pmatrix} \tag{2.35}$$

$$\lambda_{IPP} = arcsin(n) \tag{2.36}$$

$$\phi_{IPP} = \phi_r + arctan\left(\frac{e}{u}\right) \tag{2.37}$$

On a geographic map, the IPP is then assigned a color according to its value of $\tilde{I}_v$, with blue being low delay (0 m) and red being high TEC (usually 10 or 20 m). Figure 2.3 illustrates this concept with a cross-section cartoon.

Some maps may include circles at the locations of the IPPs with line segments pointing back to the receiver making the measurement. Then by simply bi-linearly interpolating equivalent vertical delays between each set of nearest three IPPs and assigning these colors, a map can be used to illustrate the variation of total electron content over a large region combining many different receivers. If the nearest IPPs are more than 5° away, however, the region is left blank, as there is insufficient data to indicate what may be occurring in the ionosphere at that region. For this reason, as the satellites and their associated IPPs move, the shaded regions of the map change shape from figure to figure.

An example of nominal ionospheric behavior, as described in Section 1.3.1, is illustrated in Figure 2.4. A map of nominal ionospheric behavior on 2 July 2000 at 21:40 UT, over CONUS was obtained from WAAS supertruth data assuming a 350 km shell height. The axes indicate latitude and longitude in degrees, with positive north and east.

This map demonstrates that, on the whole, the nominal ionosphere varies smoothly

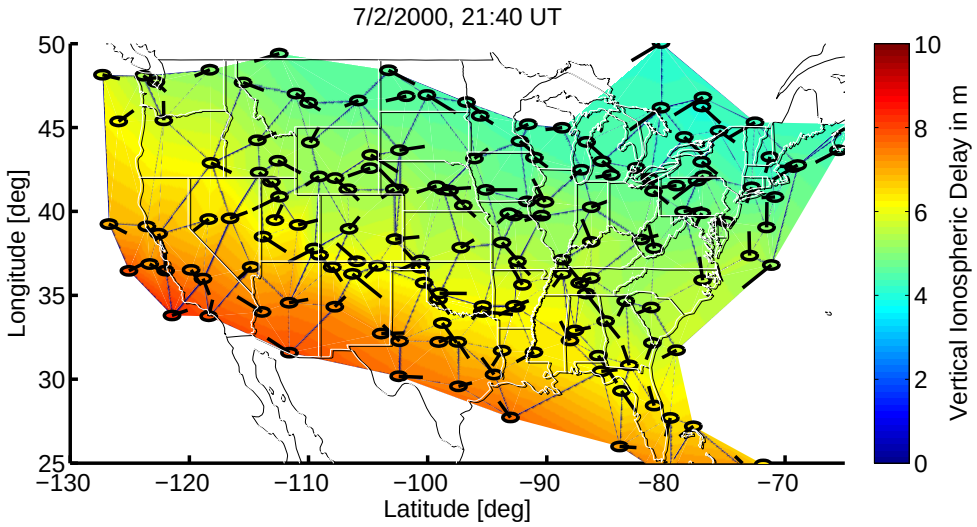

Figure 2.4: Contour map of nominal ionosphere over the United States. Colors range from 0 to 10 m of equivalent vertical range delay.

over a large region. This allows the SBAS and GBAS to model and estimate the nominal ionosphere with reasonable confidence on typical days.

2.3.3 Space-Based Remote Ionospheric Sensing

Dual-frequency measurements of TEC are not limited to ground stations. Orbiting satellites that perform ranging with two frequencies also yield information about the electron content on the signal raypaths. Two in particular are used in this work.

1. Jason

   Jason is a satellite designed to measure sea surface height using an onboard altimeter (at C- and Ku- bands). It orbits at an altitude of about 1330 km, repeating its ground track every 10 days. One of the sources of error corrected for in this sea surface measurement is the delay due to the ionosphere as the radar signal makes its way roundtrip from 1300 km to the ground. Data processed by Patricia Doherty and Bonnie Delay at the Boston College Institute for Scientific Research includes the latitude and longitude of the satellite and the ionospheric TEC, in TECU. These measurements are converted to delay at GPS L1 frequency with Equation (2.14). The Jason data are covered in greater depth in Section 6.4.1.

2. SAC-C

   The Satelite de Aplicaciones Cientificas-C (SAC-C) is a science mission satellite developed jointly by the US National Aeronautics and Space Administration (NASA) and Argentina's Commission on Space Activities (CONAE). SAC-C orbits at 700–730 km altitude in a sun-synchronous orbit [Alonso *et al.*, 2000]. Onboard is a Blackjack dual frequency GPS receiver developed for use on satellites with high bandwidth tracking loops for the dynamic Doppler rates between orbiting satellites at JPL.

   The SAC-C slant TEC measurements, $\tilde{I}_s$, are formed from the GPS dual frequency code and carrier estimates as shown in Equations (2.22) - (2.26), with the satellite bias, receiver interfrequency bias, and integer ambiguities estimated and removed such that the quiet nighttime delay at L1 is near 0 m. The SAC-C measurements featured in Chapter 6 are made at nighttime. To compare them with ground measurements made simultaneously, the broadcast satellite hardware biases, τ_{gd}, are removed. Then the receiver interfrequency bias, IFB, is estimated to be the value that ensures that all measurements are non-negative during a non-stormy nighttime. The measurements of interest will be discussed in greater detail in Section 6.4.2.

2.4 Disturbance Storm-Time, D_{st}

As mentioned in Chapter 1, the ionosphere is coupled to the magnetosphere, which is in turn driven by the solar wind. For this reason, measures of geomagnetic activity provide information by proxy about the ionosphere. Starting in 1957, one such measure of geomagnetic activity (whose use dated back to 1910 but had been limited to geomagnetic stormy conditions) was defined and continuously measured. This index, abbreviated D_{st} for, "Disturbance, Storm-Time," measured the average hourly difference in nanoTesla (nT) in the axial component of the geomagnetic field worldwide from the mean. The magnetic field measurements are made at four low-latitude stations worldwide, corrected for solar daily variations, averaged, and differenced from the mean as described by Sugiura and Kamei [1991]. These hourly D_{st} values are publicly available through the National Oceanic and Atmospheric Administration (NOAA) Space Physics Interactive Data Resource (SPIDR) [National Geophysical Data Center, 2005].

Figure 2.5 illustrates the behavior of D_{st} over a few days encompassing the geomagnetic storm of 20 November 2003. The geomagnetic storm signature shown in Figure 2.5 consists

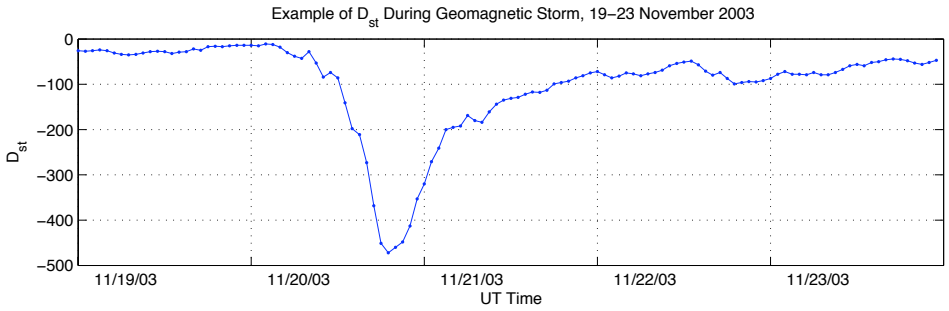

Figure 2.5: Example of D_{st} measurements during a geomagnetic storm. 19–23 November 2003.

of the "main phase," in which D_{st} drops rapidly, and a "recovery phase" of several days during which D_{st} gradually rises to pre-storm values.

D_{st} is designed to measure the equatorial ring current, a current loop encircling Earth at the equator in the radiation belts. Daglis [1999] provides a detailed review of the ring current. The asymmetric, or partial, ring current occurs over a limited range of longitudes primarily in the afternoon and dusk sectors. Liemohn et al. [2001] attribute a significant portion of the main phase drop in D_{st} to the asymmetric ring current. Takalo and Mursula [2001] suggest that the partial ring current leads to diurnal variations in mean D_{st}. The ring current is induced by interactions between the solar wind and the magnetosphere and tends to produce a magnetic field that opposes Earth's core magnetic field. Space weather disturbances produce a strong ring current that is detectable through an overall decrease in the geomagnetic field of as much as a few hundred nT. D_{st} values are used in Chapter 4 to compare the impact of various ionospheric storms on WAAS availability.

2.5 WAAS Approach Service Coverage

Availability is measured as the percentage of time that a particular type of navigation service is offered to users. The percent area for which LPV is available a certain percentage of the time is known as "coverage." Typically the FAA reports LPV coverage at the 95% or 99% availability levels. Coverage percentages were obtained from the FAA for the periods shown in Table 2.3. For some periods LPV coverage was not reported by the FAA, but coverage for another level of precision approach service known as Lateral Navigation with Vertical Navigation (LNAV/VNAV) with less strict integrity requirements was reported. In these cases, the LNAV/VNAV coverage value provides an upper bound on, and is typically within

1–2 percentage points of, what LPV coverage would have been. WAAS approach service availability and, thus, coverage, will be shown to be affected by the degree of irregularity in the TEC variation in the ionosphere in Chapter 4.

Table 2.3: Periods of Coverage Percentage Data

Start (yyyy)	Start (mm)	Start (dd)	End (yyyy)	End (mm)	End (dd)	Availability Measure
2001	07	01	2001	12	31	LPV 95%
2002	01	01	2002	06	30	LNAV/VNAV 95%
2002	07	19	2002	09	16	LPV 95%
2003	04	01	2003	06	30	LPV 95%
2003	07	01	2005	03	01	LPV 95%

2.6 Summary

This chapter introduced several different types of measurements of Earth's space environment that will be used herein. These include ionosonde measurements of maximum electron density and altitude, total electron content from dual-frequency ranging, and a measure of worldwide geomagnetic activity. These measurements are made from a suite of both ground- and space-based sensors. The processing required to use each of these measurements was described. In Chapter 3, the ground-based dual-frequency GPS measurements from CORS, IGS, and WAAS will be used to illustrate the threats to an airborne GPS user's integrity that can arise during periods of ionospheric activity.

Chapter 3

Examples of Integrity Threats

3.1 Overview

This chapter illustrates the specific problems that irregularities in the ionosphere pose to augmentation systems, using data from the solar maximum period of the current solar cycle. The next section shows observations of the overall differences between nominal conditions and stormy conditions. Section 3.3 shows observations of spatial gradients, which will be discussed in greater detail in Chapter 5 for their integrity impact on LAAS. In practice, spatial and temporal variations are blended together because the ionosphere irregularity, the lines of sight of the reference stations and user, and the user himself are all moving simultaneously. This has posed a great part of the challenge in modeling ionosphere threats to LAAS; some threats under worst-case scenarios could be nearly unobservable. For LAAS, the challenge is structures in the ionosphere, possibly large-scale, that fall beyond the view of the LGF.

Section 3.4 discusses the specific limitation of WAAS ionosphere modeling: failing to distinguish between viewing angles before performing a planar fit to the data. Often this triggers the WAAS Irregularity Detector. Section 3.5 is concerned with the problem of WAAS undersampling, in which irregularities in the ionosphere may be localized enough to fall between WAAS network measurements. A model of the electron variation in these conditions developed in Chapter 6 is an important step in understanding how long-lasting such an enhancement can be.

3.2 Nominal vs. Active Mid-Latitude Ionosphere

The process for plotting dual-frequency GPS ground measurements of the ionospheric total electron content (TEC) was discussed in Section 2.3.2. A map of nominal mid-latitude daytime ionosphere delay over CONUS is usually similar to Figure 3.1(a). The challenge is to determine in real-time whether the ionosphere is instead behaving as shown in Figure 3.1(b), and protect users from delays of the magnitudes and variations shown there. Figure 3.1(b) is a snapshot of the ionosphere based on WAAS supertruth data taken on 29 October 2003, at 21:40 UT, during an ionospheric storm. In both figures the color ranges from 0 to 10 m of delay at L1.

In Figure 3.1(b) the absolute values of ionospheric delay are among the highest observed. The IPPs with equivalent vertical delays of 35 m to the south on the map are associated with fairly low elevation satellites, so the slant path delay experienced by the receiver may actually be a factor of two or three more, when using the mapping function in Equation (2.29) to convert the equivalent vertical delays shown here back to the receiver's slant raypath delay. Later during the same storm, vertical delays approaching nearly 45 m were observed. Such large delays are rare but not unique; comparable magnitudes were observed during the 15 July 2000 storm. With high TEC near regions of relatively low TEC (shown in blue on Figure 3.1(b)) the ionosphere does not vary in a smooth planar manner over hundreds of kilometers.

For an augmentation system to provide integrity to its users, the system must do one of two things. In the first option it must model behavior such as that shown in Figure 3.1(b) accurately and be able to broadcast that information to its users in real-time with bounds that will cover the spatial variability observed. The LAAS ionosphere threat model applies to all users all the time to cover the spatial variability shown in the next section and in Chapter 5.

If the ionospheric model fails to accurately represent disturbed behavior, then the AS must instead have a detection system of some kind in place to warn that the errors cannot be tightly bounded. This is the motivation behind the WAAS Irregularity Detector. The detector provides a robust warning system when the ionospheric model cannot safely be used with the observations made, during which time the broadcast message from WAAS is set to the maximum bound value, effectively prohibiting LPV precision approach service to its users [Walter *et al.*, 2000].

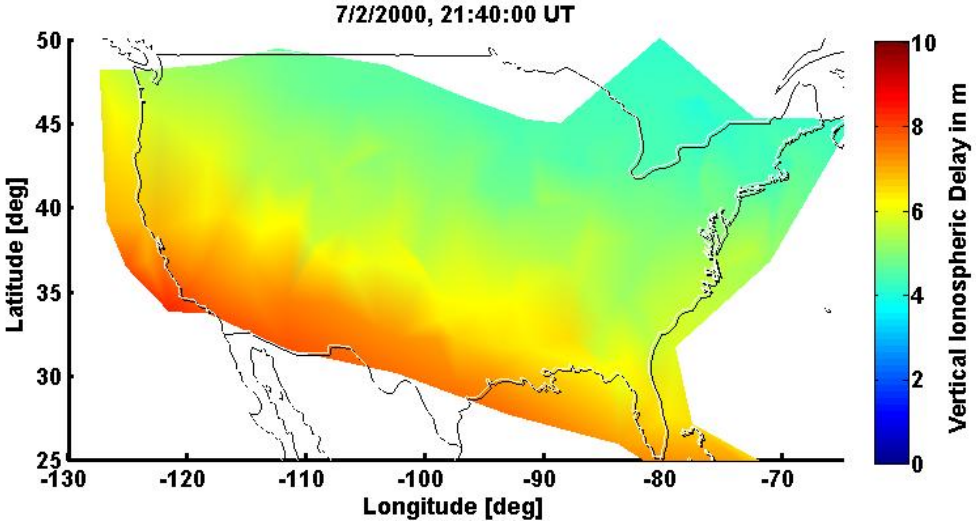

(a) Nominal

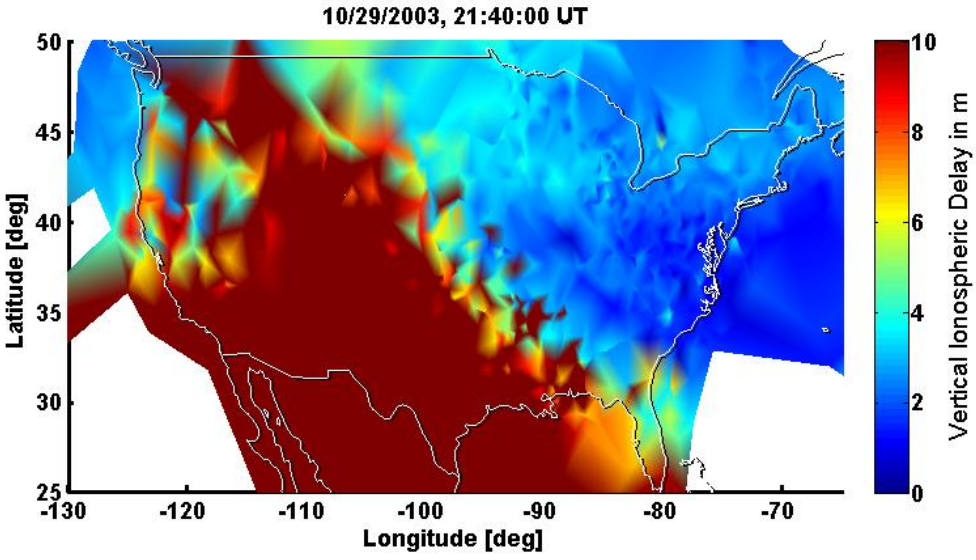

(b) Active

Figure 3.1: Contour map of ionosphere observed over the United States. Colors range from 0 to 10 m of equivalent vertical range delay.

3.3 Spatial Gradients

An augmentation system offers service over a large geographic region, whether tens of kilometers (GBAS) or hundreds of kilometers (SBAS). Users may be distant from the nearest augmentation system reference station. The difference between the ionospheric delay suffered by the user and the reference station could be significant, depending on their proximity. To provide confidence levels on ionospheric corrections, a measure of how different a nearby user's delay could be, i.e., a spatial decorrelation rate, must be known.

During disturbed periods, the user near the reference station may experience a very different delay. Without a way to distinguish that a region is under a disturbed ionosphere (i.e., an irregularity detector), the augmentation system must bound the highest possible spatial decorrelation rates for all users at all times if it is to ensure integrity.

Figure 3.2 shows a contour map that delineates the location at which a high spatial decorrelation rate was observed. The CORS dual-frequency GPS data plotted are over the midwestern US during an ionospheric storm period on 20 November 2003. Latitude and longitude are marked on the axes, with degrees north and east positive. The only IPPs plotted explicitly are the two from CORS stations MTVR and COLB to GPS satellite (SVN) 44. The distance between these two stations is about 65 km and the difference in their equivalent vertical delays is about 15 m.

WAAS successfully contended with these features through the use of its irregularity, or "storm," detector, which notified users in this region that vertical guidance was unavailable until the storm conditions had subsided. Without the irregularity detector, WAAS would need to broadcast overbounds on the few hundred mm/km spatial decorrelation rate for all its users all the time. This would hurt overall availability. Without a storm detector that robustly declares periods of disturbed activity, the general AS would need to assume these conditions could happen to any user at any time anywhere within the region of coverage. This is the approach of LAAS, and quantifying the magnitude of such spatial variations is the topic of Chapter 5.

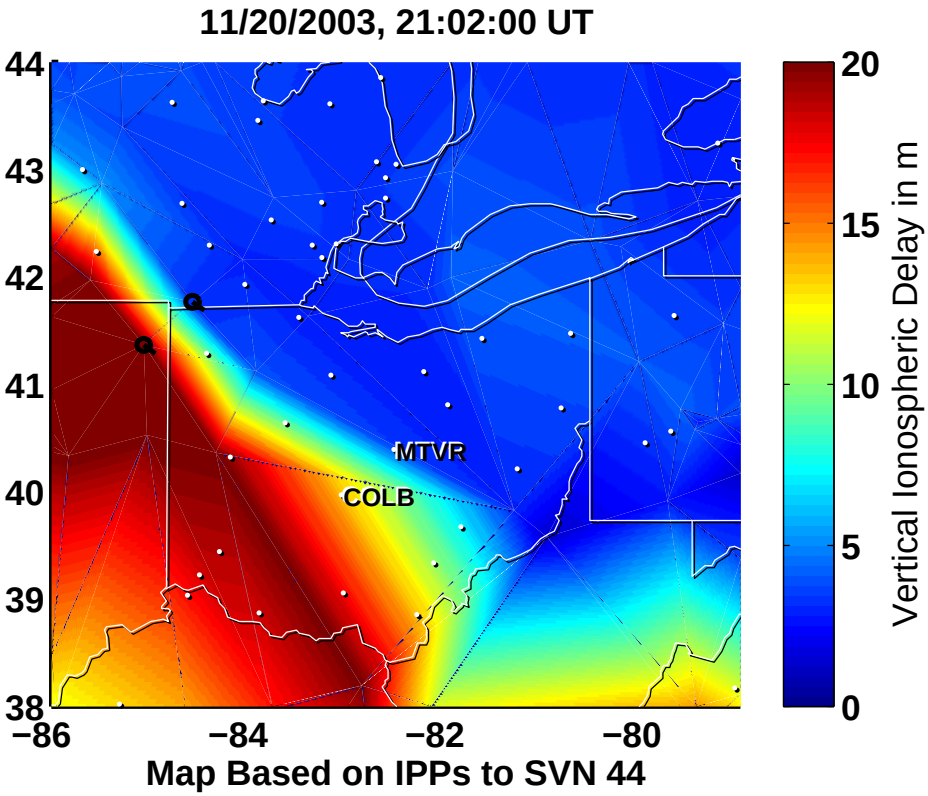

Figure 3.2: TEC map from CORS stations in Ohio to GPS SVN 44.

3.4 Thin Shell Limitations

The International Civil Aviation Organization's (ICAO's) Standards And Recommended Practices (SARPs) specify that a grid of ionospheric error corrections and bounds be broadcast by an SBAS such as WAAS. In order to represent the ionosphere as a grid, the SARPs specify that the thin-shell model described in Section 2.3.2 must be used with the shell height $h_{iono} = 350$ km. This representation of the ionosphere has limitations that remain even during the quietest, most nominal ionospheric behavior. Specifically, by collapsing the three-dimensional ionosphere of several hundred kilometers thickness into a two-dimensional shell, vertical information is lost.

This issue is illustrated in Figure 3.3. Even though the ionosphere is a layer of the upper atmosphere with a finite thickness (gray region), the WAAS algorithm assumes that the bulk of the error happens within a layer of infinitesimal thickness (white line). The line of sight from Receiver A to Satellite 2 passes through nearly the same latitude and longitude as the line of sight from Receiver B to Satellite 1 at 350 km altitude. They have the same IPP location regardless of the orientation of the satellite-to-receiver raypaths. The signals travel through very different regions of the ionosphere. So, even though the IPPs would appear at the same point on a map, they may have very different range delay values. As a result, the differential delay between two IPPs on the shell may not vanish in the limit when they are colocated because their "look angles" may be completely different. This is a limitation inherent to the thin shell model.

Figure 3.4 serves to illustrate this point for a nominal day, as obtained from the WAAS supertruth data. The analysis and production of this plot was performed by Rajagopal, and is described in detail in his earlier work on the subject [Rajagopal *et al.*, 2004]. Briefly, at each epoch every possible pair of IPPs is placed into a bin in a two-dimensional histogram based on 1) the difference in vertical delay, and 2) the separation distance between them. At each distance column (spanning 100 km each), the 95^{th} percentile (2-sigma) bound on the difference in vertical delay between IPPs is found and normalized to a 1-sigma value by dividing by two. These bounds are plotted in magenta as a function of IPP separation distance. The green curve places additional requirements on the IPP pair: the elevation angles must lie within 15° of each other, as must the azimuthal angles. This enforces that they have similar look angles before they are counted in the histogram. The 95^{th} percentile of these points are obtained and plotted in green.

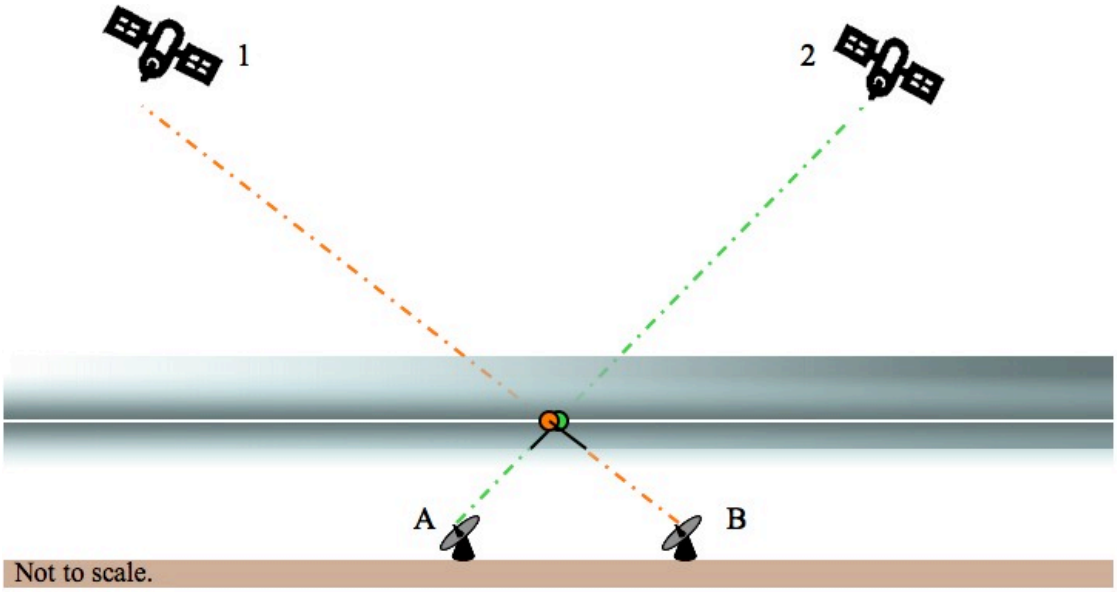

Figure 3.3: Illustration of two raypaths from different receivers to different satellites, but with the same ionosphere pierce point location. The raypaths travel through different parts of the ionosphere.

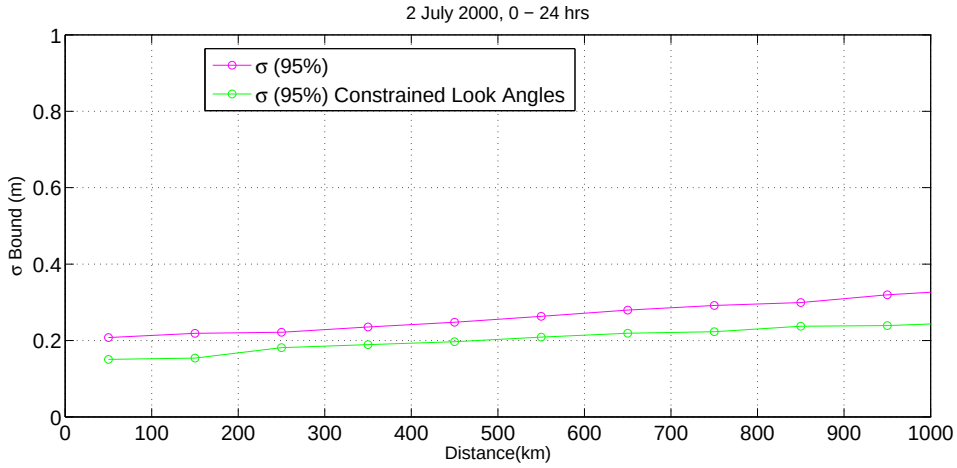

Figure 3.4: Normalized 95^{th} percentile standard deviation of equivalent vertical range delay differences (m) vs. IPP separation distance (km) on a nominal day. Magenta: all possible pairs of IPPs. Green: IPPs with $\triangle el \leq 15°$ and $\triangle az \leq 15°$.

Figure 3.4 shows that the sigma bound, when counting all possible pairs (magenta), does not approach the origin. Instead, on this quiet ionosphere day, as the IPPs become closer together, the difference between them may vary by a fraction of a meter. If the only IPP pairs counted are the ones whose elevation angles and the azimuth angles lie within 15° of each other, then the sigma bound is somewhat reduced, but still does not approach a delay difference of zero as IPP separation approaches zero. Logically this delay difference must approach zero as raypaths are more nearly coincident. Limiting the difference in azimuth and elevation between any two lines of sight is one way to enforce coincidence, but may still allow for comparison from two different stations to two different satellites, as shown in Figure 3.3. Also, dividing IPP separation distance into bins smaller than 100 km could improve the estimate approaching 0 km. With this data set, however, constraining allowable pairs to align within an angle smaller than 15 degrees or binning the distances by less than 100 km yields too few samples near 0 km to form an estimate of the variance. This is one reason that understanding the vertical variation of the electrons in the ionosphere is helpful for augmentation systems.

3.5 Undersampling

Since the SBAS uses a real-time data-driven model of the ionosphere, it must contend with the threat of undersampling. The SBAS developers must factor in the probability that there is some feature in the ionosphere that is not detected by the reference receivers. This feature may lie just beyond the view of the receiver network, or it may be an even more insidious threat, one that just happens to fit right in between the measurements of the reference stations. In the latter case, the ionosphere may seem to be well-sampled when in fact it is not. A comparison of the next two figures illustrates this point dramatically.

Figure 3.5(a) shows an IPP contour map, generated in the same way as Figure 3.1, of the IPPs from WAAS measurements on 30 October 2003 at 05:50 UT. The contour colors are interpolated with the mapping routine described in Section 2.3.2. These contour colors serve merely to give an idea of what information WAAS had available to it in real-time. The IPPs are denoted with black circles, and their associated receivers lie in the direction of the line segments. Longer line segments indicate that the satellite is at a low elevation. The color scale varies from 0 to 20 m.

On the whole the map is relatively quiet, since it is a snapshot of local night-time,

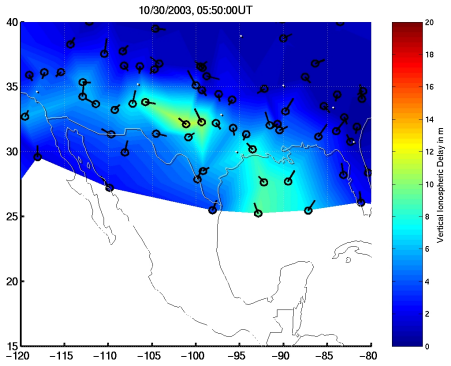

(a) WAAS-based TEC map and IPPs.

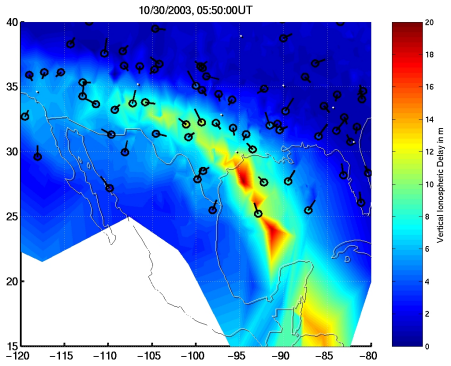

(b) CORS-based TEC map. WAAS IPPs (same as (a)).

Figure 3.5: Comparison of ionosphere sampled at lower density by WAAS to "actual" activity, as observed in higher density CORS data, over the southern US on 30 October 2003.

although even an equivalent vertical delay value of 5 m (medium blue) is higher than usual at mid-latitude local nighttime. There are indications of irregular behavior over Texas and at the edge of the sampled region, over the Gulf of Mexico.

Now for comparison, a contour map based on the high-density CORS network data is shown at the same epoch in Figure 3.5(b). Overplotted on this CORS contour map are the very same WAAS IPPs shown in Figure 3.5(a). The CORS measurements indicate that there is a localized region of the ionosphere where equivalent vertical delays of 20 m were measured. This map shows that the WAAS IPPs at this epoch hovered just on the edges of this irregularity. In one case, the IPP at (25° N, 93° W), sampled in nearly the same thin shell location as this irregularity. However, the delay measured at that point was less than in surrounding areas. For this IPP, the WAAS reference station ZFW at Fort Worth, Texas, viewed satellite SVN 26. CORS stations in the Dallas/Fort Worth area made observations around 15–19 m equivalent vertical. The WRS measurements peaked at 16 m a few minutes later, but at this particular epoch, the measurement was only about 10 m.

Also, what may have appeared to be two different features colored green in Figure 3.5(a) was more likely a continuation of one larger structure. The apparent distinctness of the two green areas in Figure 3.5(a) is an artifact of the contour plotting method.

This contour plot says nothing about the confidence with which colors are assigned. That is the fundamental advantage to the SBAS estimates. An SBAS offers more than just

a best guess of the ionospheric error based on whatever measurements are available. It offers a guarantee on the worst value of true ionosphere for a user, based on the measurements. In the case shown in Figure 3.5, the bounds would need to cover the unobserved 20 m vertical delay.

An additional challenge of contending with undersampling threats is that, in order for the SBAS to meet FAA certification requirements, its overall broadcast integrity bound must be sufficient for any combination of user IPPs. Since the SBAS has users over a wide geographic region and has no knowledge of where the users' IPPs are, it must protect them from possible ionospheric features, no matter what distribution of ionospheric pierce points it measures.

SBAS developers can study this issue of protecting users given any possible sampling of the ionosphere through the use of data deprivation. The goal of data deprivation is to simulate scenarios in which the SBAS would have sampled the ionosphere insufficiently in a threatening area (as it did in Figure 3.5) and assess the resulting severity of the threat to the user. SBAS designers must then develop an undersampling bound that protects against the most severe of these threats.

Figure 3.6 illustrates a scenario artificially created by deprivation. The scenario mimics the physical situation that was observed in Figure 3.5. In Figure 3.6(a) a contour map of equivalent vertical delay (0–10 m) is plotted using all CORS data available at 05:00 UT on 31 October 2003. The feature over Florida was sampled by WAAS as well, but for plotting purposes CORS data is more complete. One particular choice of data deprivation schemes (many are possible) is applied to the WAAS supertruth data at this epoch. The IPPs that are *not* excluded by this process are plotted with circles and lines directed toward the receiver making the measurement. The excluded supertruth IPP data, not shown, are all located in the red-yellow region over Florida in the contour map.

In contrast, Figure 3.6(b) shows what the contour map would look like based on the WAAS measurements without these excluded IPPs. As a result of this combination of IPPs, not only does activity appear to be generally calm over Florida, but the region appears to be relatively well-sampled. The unsampled region artificially created over Florida is not much larger than the actual gap in measurements over the Gulf of Mexico. There are measurements of about 2.5–3.5 m on all sides, which would all seem to confirm that nothing unusual is occurring over Florida. For this distribution of IPPs, the ionosphere varies quite a bit even though the region seems well-sampled. The SBAS would need to protect users

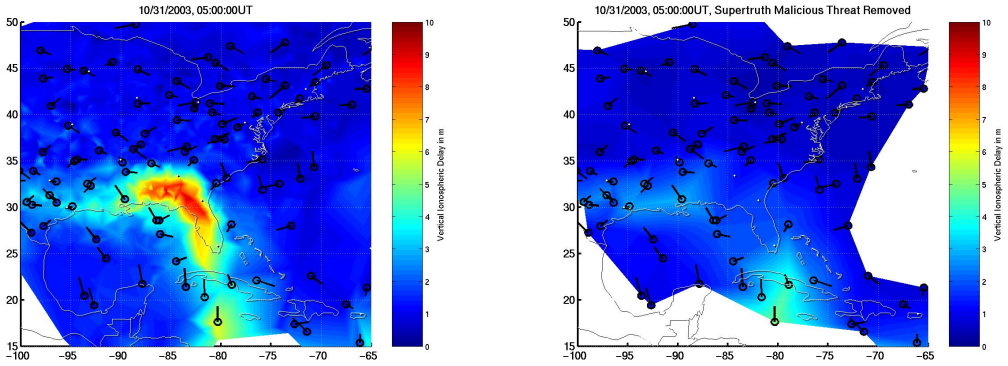

(a) CORS-based TEC map. WAAS IPPs not excluded by data deprivation.

(b) WAAS TEC map and IPPs based data not excluded by deprivation.

Figure 3.6: Illustration of data deprivation as a method for characterizing undersampling.

from this possibility.

Ideally, the SBAS developers would do an exhaustive search over all possible combinations of IPPs, but this is prohibitively time-consuming, computationally expensive, and extremely pessimistic. One possible and extremely conservative deprivation technique is to search for precisely those combinations of IPPs that would give the most trouble to the SBAS model: create a scenario that fools the system in the worst possible way and make sure that that scenario is protected by the undersampling bound. The current WAAS implementation is to eliminate measurements from a single WRS at a time or to remove multiple stations in each of the eight cardinal directions. The first method models threats due to a missing station or satellite thread and the second mimics storms that might occur beyond the geographic edge of sampling [Pandya *et al.*, 2007]. These methods are more efficient and realistic, but still allow for undersampled regions of small area.

Chapter 6 will discuss in great detail the event shown in Figure 3.6 on 31 October 2003. This night and the previous night, mapped in Figure 3.5, were part of a larger series of events collectively called the Halloween Storm of 2003, which will be discussed in Chapter 4. However, localized TEC enhancements are not limited to the Halloween Storm alone. Figure 3.7(a) is a plot of the equivalent vertical delay at L1 on the night of 6–7 April 2000, during which another of the most severe storms of the same solar cycle occurred. At 08:00 UT (03:00 EST) on 7 April 2000, a localized region of enhanced TEC of about 8–9 m is visible above, south, and west of Florida. The background ionization of this feature is different from that of the Halloween Storm, however. While the northern CONUS ionization

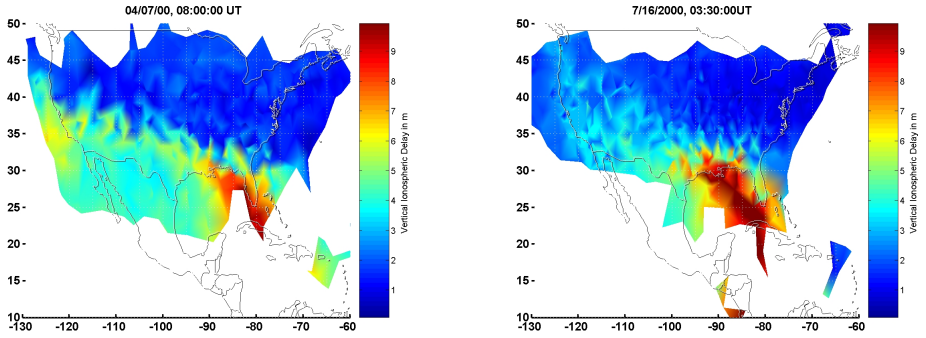

(a) 7 April 2000, 08:00 UT (04:00 EDT).

(b) 16 July 2000, 03:30 UT (15 July 2000, 23:30 EDT).

Figure 3.7: CORS data IPP maps for storms exhibiting a localized enhancement over southeastern US.

level is around 1 m of delay, the southern region of CONUS is in the 4–6 m range. This feature is not so prominent against the background because the background level is higher. In addition, the evolution prior to this configuration of the ionosphere may be different, based on maps generated at two-hour intervals throughout the night, shown in Appendix B.

As another illustration, a map of equivalent vertical TEC at 03:30 UT on 16 July 2000 is shown in Figure 3.7(b). In a similar location and orientation — west of Florida, aligned northwest-southeast — another TEC enhancement of about 10 m is visible. Finally, Dehel [2005] shows a TEC map generated by Jonathan Makela for 03:00 UT on 17 July 2004. On this map, there was a 7 m enhancement extending northwest-southeast from Georgia that was separated from the main daytime TEC enhancement by a small region of 1–2 m delay to the west. The map for this event looks generally similar to that of the Halloween storm at 23:00 UT on 30 October 2003. However, the magnitude of the spatial variation is smaller for the July 2004 event. During 17 July 2004 a minor geomagnetic storm occurred that had minimal effect on WAAS performance, unlike the 2000 and 2003 storms, for which LPV service availability was impacted.

3.6 Summary

At all times while an augmentation system provides service, confidence bounds must be broadcast on spatial gradients since users are not colocated with reference stations. During disturbed conditions the ionosphere can be highly nonplanar, and spatial gradients as high as a few hundreds of mm differential delay per km of separation have been observed. The first evidence of such high spatial gradients and the challenge in estimating them over short distances is the topic of Chapter 5 with a case study from the 6–7 April 2000 storm. One of these challenges is that the gradients are coupled to user geometry and relative velocity of the ionosphere.

A successful augmentation system bounds the threats illustrated in this chapter to maintain user integrity while keeping navigation service availability high. The threats to integrity with which the augmentation system must contend include localized irregular behavior, as is seen during the 29–31 October 2003 storms. The daytime storm-enhanced densities of these periods introduced equivalent vertical delays of as much as 45 m in some areas of CONUS. User slant delays would have been as much as a factor of two to three higher. Behavior which indicates a breakdown of the ionospheric model (in the WAAS case, the planar fit) should be mitigated by the use of some form of irregularity, or "storm," detector. Localized enhancements have been observed to occur during the worst storms. These localized irregularities that could slip in between augmentation system measurements must either be bounded at all times (reducing availability to an unacceptably low level), or mitigated with a storm detector, as WAAS does.

One outcome of using the thin-shell model for providing SBAS correctsions is that even colocated IPPs may have entirely different equivalent vertical delays. More than a spatial gradient, this can be interpreted as a look-angle decorrelation. The SBAS must protect a user from using an estimate of the ionosphere based on reference station measurements taken from very different elevation and azimuth angles than the user's own.

Finally, the threat of undersampling the ionosphere was illustrated for any data-driven model. A specific instance of an SBAS barely detecting a significant feature was pointed out. It is precisely for such cases that the WAAS ionospheric threat algorithm includes a sigma bound on undersampling. Data deprivation simulates undersampling scenarios to allow for threat assessment and development of bounds. Each of the threats mentioned in this paper have been bounded or mitigated by WAAS, and any future augmentation system

offering integrity will need to address all of these issues as well. The algorithm to mitigate these threats with an acceptable level of service availability is nearing completion for LAAS as well. For an operational system, once the crucial service of integrity has been provided to users, the next step will be to continue to maintain it while increasing availability.

This chapter has shown examples of integrity challenges from observations of several different storms. Chapter 4 discusses how to place the severity of these storms in the context of activity from previous decades.

Chapter 4

Ranking Storms with D_{st}

4.1 Overview

The previous chapter illustrated the specific integrity challenges that an irregular ionosphere poses to an SBAS such as WAAS and to a GBAS such as LAAS. This chapter covers ways of identifying when and how often these challenges may occur using historical records of geomagnetic activity. Section 4.2 describes the WAAS algorithm that indicates a disturbed ionosphere and reduces LPV availability to keep users safe. Then Section 4.3 shows that this algorithm shows moderate correlation with the geomagnetic index D_{st}. It will be shown from one half of Solar Cycle 23 that D_{st} can be used as an indicator of the magnitude of irregularity in the ionosphere, and is very successful as a predictor of those irregularities associated with near-worst-case integrity threats. Then with almost 50 years of D_{st} values, Section 4.4 uses D_{st} data dating back to 1957 to show that the major storms of Solar Cycle 23 have been representative of what may have occurred prior to the existence of dense TEC measurements. Of these, two storms will serve as case studies for WAAS integrity and LAAS integrity, respectively, in the subsequent chapters.

4.2 Irregularity Detector and Availability

Chapter 1 described the augmentation system performance criteria of integrity and availability. In the presence of disturbed ionosphere, the augmentation system may need to maintain user integrity by making a particular type of service unavailable. The Wide Area Augmentation System achieves this through the Irregularity, or "Storm," Detector. The

Irregularity Detector provides a way of quantifying the impact of ionosphere storms over CONUS. The algorithm, described in detail by Walter et al. [Walter *et al.*, 2000], is reviewed here and will be implemented in Section 4.3.

WAAS provides ionosphere corrections and bounds for points defined at regular $5^\circ \times 5^\circ$ latitude and longitude intervals over CONUS, known as Ionosphere Grid Points (IGPs). At each IGP, the IPP measurements from the WAAS network that fall within at least an 800 km radius but no more than a 2100 km radius are used, provided there are at least 30 of them. If, after the search radius has been expanded to 2100 km, there are fewer than 10 IPPs, the estimate is not formed and the WAAS broadcast for that grid point is "Not Monitored." For an IGP with a sufficient number, N, of nearby IPPs, the measurements form vector $\mathbf{I_{v,IPP}}$:

$$\mathbf{I_{v,IPP}} = \begin{pmatrix} I_{v,IPP_1} \\ I_{v,IPP_2} \\ \vdots \\ I_{v,IPP_N} \end{pmatrix} \tag{4.1}$$

In the real-time system a least-squares planar fit is performed on these measurements and the resulting coefficients are used to estimate the ionosphere grid delay (IGD) vertical ionosphere at the IGP. The χ^2 statistical measure of goodness-of-fit is computed at each IGP as well. The χ^2 value effectively tests that the data are consistent with the assumption of a planar model ionosphere. It is used as the parameter to be tested in the Irregularity Detector.

The observation matrix, $\mathbf{G}$, weighting matrix, $\mathbf{W}$, and IPP measurements, $\mathbf{I_{v,IPP}}$, used to compute the IGD are also used to compute χ^2. The definition of the matrices $\mathbf{G}$ and $\mathbf{W^{-1}}$ for this computation from [Walter *et al.*, 2000] are reproduced as Equations (4.2) and (4.3) below:

$$\mathbf{G} = \begin{pmatrix} 1 & d_{IPP_1,IGP} \cdot \hat{E} & d_{IPP_1,IGP} \cdot \hat{N} \\ 1 & d_{IPP_2,IGP} \cdot \hat{E} & d_{IPP_2,IGP} \cdot \hat{N} \\ \vdots & \vdots & \vdots \\ 1 & d_{IPP_N,IGP} \cdot \hat{E} & d_{IPP_N,IGP} \cdot \hat{N} \end{pmatrix} \tag{4.2}$$

$$\mathbf{W^{-1}} = \begin{pmatrix} \sigma^2_{I_v,IPP_1} + \sigma^2_{decorr} & \sigma_{bias,1,2} & \cdots & \sigma_{bias,1,N} \\ \sigma_{bias,1,2} & \sigma^2_{I_v,IPP_2} + \sigma^2_{decorr} & \cdots & \sigma_{bias,2,N} \\ \vdots & \vdots & \ddots & \\ \sigma_{bias,1,N} & \sigma_{bias,2,N} & \cdots & \sigma^2_{I_v,IPP_N} + \sigma^2_{decorr} \end{pmatrix} \tag{4.3}$$

In the weighting matrix, $\sigma^2_{I_v,IPP_i}$ is the variance that bounds receiver noise, multipath, and bias uncertainty for the i^{th} IPP. The off-diagonal elements, $\sigma_{bias,i,j}$, are the cross-correlation biases, nonzero if lines of sight i and j share a common satellite or a common receiver. The nominal decorrelation of the ionosphere over CONUS is $\sigma_{decorr} = 35$ cm about a plane, independent of distance [Walter *et al.*, 2000]. The χ^2 statistic is then:

$$\chi^2 = \mathbf{I^T_{v,IPP}} \cdot \mathbf{W} \cdot \left(\mathbf{I} - \mathbf{G^T} \cdot \left(\mathbf{G} \cdot \mathbf{W} \cdot \mathbf{G^T} \right)^{-1} \cdot \mathbf{G} \cdot \mathbf{W} \right) \cdot \mathbf{I_{v,IPP}} \tag{4.4}$$

The number of degrees of freedom, N_{dof}, of the χ^2 statistic is the number of measurements minus the number of degrees of freedom of the model (3 for a planar fit) as given in Equation (4.5). The χ^2 threshold value (Equation (4.6)) can then be looked up in the table given by Walter et al. [2000]; it is a function of N_{dof}. If the ratio of χ^2 to the threshold value (Equation (4.7)) exceeds 1, then the IGP is considered to be in a storm state. The bound on the ionosphere error, known as the Grid Ionosphere Vertical Error (GIVE), that is used to compute the user's VPL is set to its maximum value of 45 m, which is safe for any ionospheric state.

$$N_{dof} = N - 3 \tag{4.5}$$

$$\chi^2_{thresh} = f(N_{dof}) \tag{4.6}$$

$$\chi^2_r = \frac{\chi^2}{\chi^2_{thresh}} \tag{4.7}$$

The result of setting the GIVE for an IGP to 45 m is that the type of vertical guidance service known as LPV, with the tightest Vertical Alert Limit, is unavailable for a user estimating his or her ionosphere delay based on that IGP. Horizontal guidance remains available throughout this period.

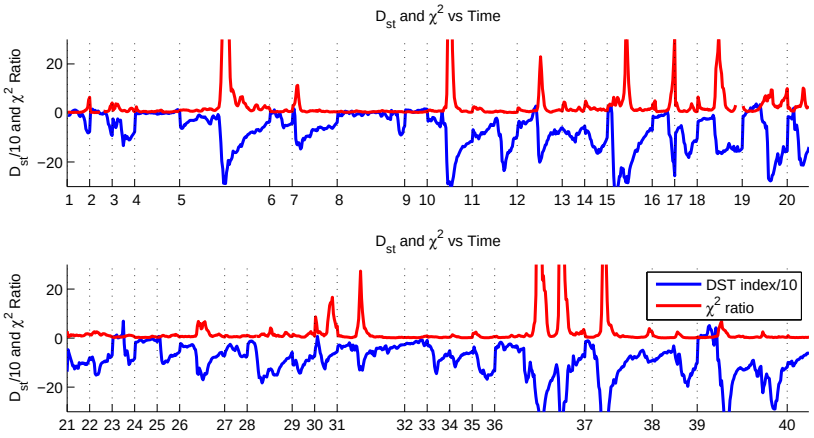

Figure 4.1: $D_{st}/10$ (blue) and χ^2_r (red) vs. time for each storm, numbered according to data sets in Table 2.2.

4.3 CONUS Irregularities 1 January 2000–1 March 2005

The previous section discussed the algorithm for detecting irregularities in the ionosphere. Tripping the WAAS Storm Detector can lead to reduction in navigation service availability and, thus, coverage. To look at the relationship between D_{st} and ionosphere irregularity over CONUS, χ^2 is compared to D_{st} as far back as the maximum of Solar Cycle 23 in this section.

4.3.1 χ^2_r vs D_{st}

Supertruth data has been generated with post-processing by WAAS prime contractor Raytheon for the dates listed in Table 2.2 by the processing described in Chapter 2. Many of the dates were chosen specifically because low LPV service availability was observed (or expected, based on external space weather and ionosphere activity reports). In the absence of coverage data, WAAS supertruth data sets are used to compute χ^2_r as the Irregularity Detector would have done in real-time, and use it as a surrogate for availability. For each of the days listed in Table 2.2, the real-time WAAS calculation of Ionospheric Grid Point (IGP) corrections and function of the Irregularity Detector described in Section 4.2, are simulated. There are 66 days total in the data set, a number of which occur during the solar maximum year 2000.

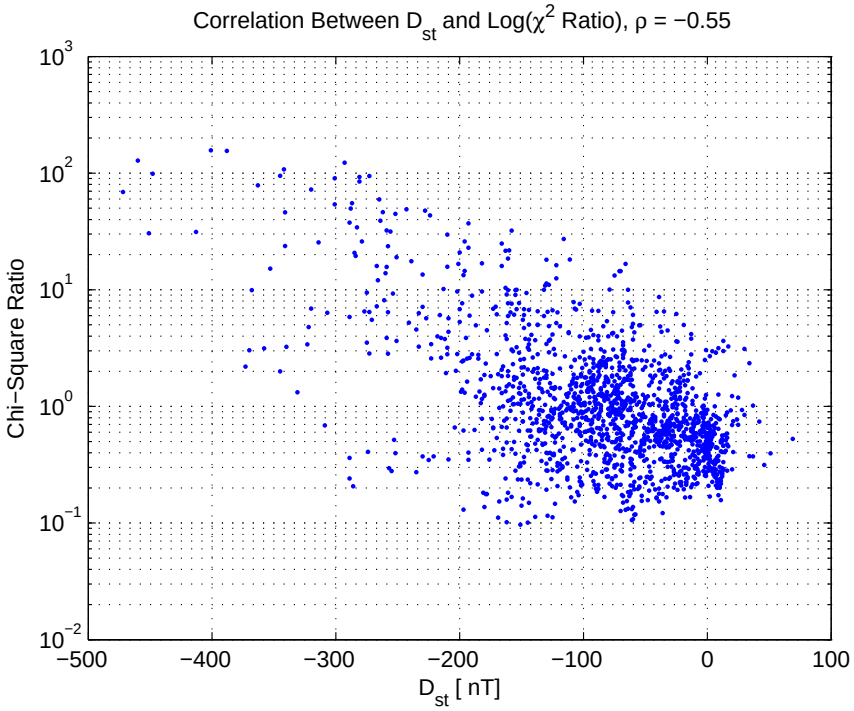

Figure 4.2: Log scatter plot of χ_r^2 vs D_{st}.

The plot of hourly D_{st} and χ_r^2 versus time for each storm is given in Figure 4.1. D_{st} is shown as a blue line and has been scaled down by a factor of 10 for easier viewing. The χ_r^2 is plotted in red. D_{st} and χ_r^2 seem to spike at about the same time, and indeed, the computation of correlation coefficient for 0, 1, and 2 hour lag in χ_r^2 confirms this; the correlation values are -0.50, -0.48, and -0.42, respectively. A conversion to $log(\chi_r^2)$ produces an even stronger correlation. With no lag, the correlation between D_{st} and $log(\chi_r^2)$ is -0.55.

The log scatter plot of D_{st} vs. χ_r^2 is shown in Figure 4.2. False alarms occur when the D_{st} is more negative than a chosen threshold, but χ_r^2 is less than one. A missed detection occurs any time that D_{st} is greater than a specified threshold while χ_r^2 exceeds one. The false alarm region on Figure 4.2 falls in the lower left region of the plot. The missed detection area is the upper right region on Figure 4.2. For a threshold of D_{st} = -310 nT, there would have been no false alarms, although there would be some missed detections. This is based on a limited number of days: those for which supertruth data has been produced.

4.3.2 D_{st} as Detector for Half Solar Cycle

The 66-day data set is extended back to 1 January 2000 by using coverage where available. The advantage of coverage percentages is that, unlike the real-time χ^2 values and IPP measurements used, historical records of the percent of CONUS that had LPV service available at least 95% of each day have been kept. In effect, coverage is a daily composite availability value, and availability is impacted by ionosphere irregularity, so coverage numbers track ionosphere activity.

For many time periods shown in Table 2.3, LPV 95% coverage values are available. In the absence of LPV 95% values, LNAV-VNAV 95% are used (see Table 2.3). For the purposes of this study, a stormy day is defined as one for which LPV 95% coverage is less than 75%. In the absence of either coverage value, a storm designation is based on χ^2_r values computed from supertruth (see Figure 4.1). Any day without a coverage value or supertruth is assumed to be a non-stormy day. The reason for this assumption is to let D_{st} be tested as a detector over a half solar cycle. The P_{MD} and P_{FA} rates are computed for half the solar cycle including solar maximum. The value of χ^2_r is a proxy for availability when coverage values are unavailable.

In the period between 1 January 2000 and 1 March 2005, D_{st} data are available for 1856 days. During this period, 59 days are stormy, either based on the coverage percentage or on χ^2_r availability (see Table 4.1). There are 9 days, corresponding to 5 continuous storms, that are printed in red. These days are referred to in the literature as "extreme storms" or "super storms." These are days that would trigger the Extreme Storm Detector (ESD). The ESD is an extension of the WAAS Storm Detector discussed in Section 4.2, with the ESD triggering for χ^2_r greater than 50 [Sparks *et al.*, 2005].

With this larger data set, the probabilities of missed detection and false alarm as a function of D_{st} threshold are summarized in Figure 4.3(a). The plot shows P_{MD} (red stars) and P_{FA} (green circles) versus D_{st} threshold. For the 5-year data set, a $P_{MD} = 0$ can be achieved at -27 nT threshold, but it yields a false alarm rate of about 50%.

The geomagnetic index, D_{st}, can be used with much greater success as an indicator of extreme storms in the 5-year period. A threshold of -287 nT achieves $P_{MD} = 0$. This threshold is driven by the extreme storm day 6 April 2000. The resulting false alarm rate is just under $P_{FA} = 0.3\%$. Based on this limited data set, very extreme D_{st} values may be very good at indicating ionosphere irregularities over CONUS.

Table 4.1: Summary of Storm Days, 1 Jan 2000 – 1 Mar 2005

Data Set	Year yyyy	Mon mm	Day dd	Cvg. %	Dst nT	Data Set	Year yyyy	Mon mm	Day dd	Cvg. %	Dst nT
1	2000	01	11	low	-81	-	2002	04	19	0	-122
2	2000	01	22	low	-92	22	2002	04	20	18	-151
3	2000	02	12	low	-133	26	2002	09	07	0	-163
5	2000	04	06	low	-287	26	2002	09	08	0	-170
5	2000	04	07	low	-288	28	2002	10	01	low	-183
5	2000	04	08	low	-87	28	2002	10	02	low	-151
7	2000	05	24	low	-147	29	2002	10	04	low	-143
10	2000	07	15	low	-289	30	2002	11	21	55	-126
10	2000	07	16	low	-301	-	2003	04	30	51	-57
11	2000	08	11	low	-106	-	2003	05	22	62	-67
12	2000	09	17	low	-201	31	2003	05	29	0	-130
12	2000	09	18	low	-193	31	2003	05	30	0	-131
13	2000	11	29	low	-119	32	2003	06	01	71	-31
14	2001	03	20	low	-165	-	2003	06	16	41	-55
15	2001	03	31	low	-358	36	2003	10	29	0	-345
15	2001	04	01	low	-215	36	2003	10	30	0	-401
16	2001	04	11	low	-256	36	2003	10	31	0	-320
18	2001	10	21	50	-166	37	2003	11	20	0	-472
18	2001	10	22	59	-166	37	2003	11	21	55	-320
-	2001	12	21	64	-51	37	2003	11	22	72	-99
-	2001	12	31	55	-27	-	2004	04	03	62	-97
-	2002	01	01	58	-41	-	2004	04	04	48	-112
-	2002	01	10	41	-51	-	2004	07	17	69	-80
-	2002	02	02	50	-83	-	2004	07	23	67	-101
-	2002	02	05	54	-81	-	2004	07	25	74	-148
-	2002	02	06	75	-70	-	2004	07	29	24	-76
-	2002	02	28	69	-49	39	2004	11	07	41	-128
-	2002	03	01	43	-64	39	2004	11	08	0	-373
-	2002	03	24	46	-101	-	2005	01	21	73	-103
-	2002	04	17	20	-106						

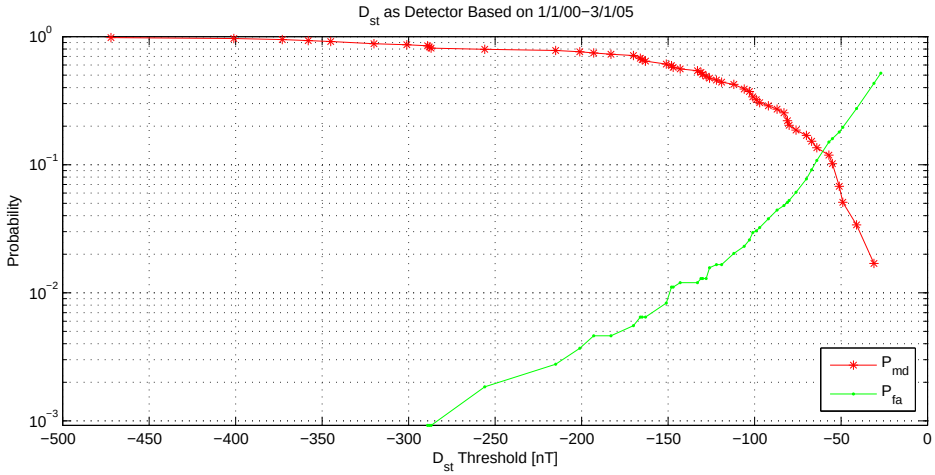

(a) Storms

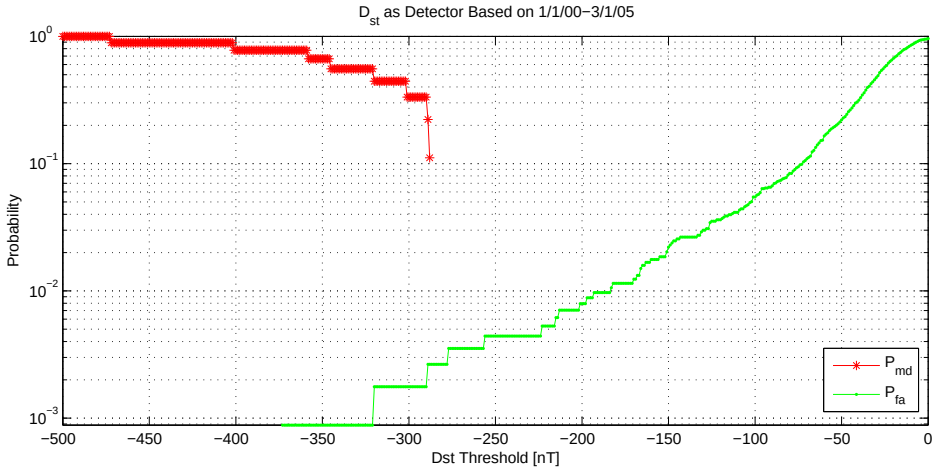

(b) Extreme Storms

Figure 4.3: Probability of missed detection (red star) and of false alarm (green circle) as a function of D_{st} threshold. Based on data from 1 January 2000–1 March 2005.

4.4 D_{st} During WAAS Operation vs. D_{st} Since 1957

This section focuses on using D_{st} to place the storms of Solar Cycle 23, which peaked around 2001, against the previous several solar cycles. Previous sections showed that D_{st} is a reasonable indicator of disturbed ionosphere over CONUS. However, coverage and χ^2_r numbers only date back as far as 2000, whereas D_{st} has been recorded since 1957. To compare the ionospherically disturbed days of this solar cycle with those of the past four solar cycles, D_{st} alone is considered. The publicly available D_{st} data were downloaded and provided by Eric Altshuler.

To compare the outliers more directly, the top 50 geomagnetic storms, according to D_{st}, are listed in Table 4.2. Those storms occurring within 2000–2005 are printed in red. The table shows that the current solar cycle contains 14 of the 50 most extreme geomagnetic storms, as measured by D_{st}. One of these storms has the 2^{nd} lowest D_{st} value on record. Maps of the ionosphere delays over CONUS on these 14 days are available in Appendix B.

Twelve of the fourteen most extreme D_{st} days contribute to the WAAS undersampled threat model. The exceptions are 10 November 2004 and 11 April 2001. These have been analyzed and pose no threats worse than the days that are already included in the threat model. In addition to these 12 days, the threat model includes 7 others for a total of 19 days: 11 January 2000, 21 October 2001, 5 November 2001, 24 November 2001, 26 July 2004, 27 July 2004, and 22 January 2005 [Eldridge, 2005].

D_{st} has been measured for 5 solar cycles. WAAS has been operating during and after solar maximum for one of these solar cycles. The expected frequency is then roughly that one of every five storms, or 20%, will have occurred during 2000–05. Instead, we find from Table 4.2 that four of the top 10, seven of the top 20, nine of the top 30, 13 of the top 40, and 14 of the top 50 stormy days happened during the years 2000–05. This corresponds to 40%, 35%, 30%, 33%, and 28%, respectively.

To compare the 2000–05 half-solar cycle with each solar cycle dating back to 1957, a histogram is plotted for the first half of each solar cycle in Figure 4.4. The horizontal axis bins D_{st} values; the vertical axis has a logarithmic scale. Since WAAS has only operated for half of a solar cycle from solar maximum year 2000 to the present (shown in purple), its distribution of D_{st} is compared to the first half of the previous solar cycles: 1989–94 (cyan), 1978–83 (red), 1967–72 (green), 1957–61 (blue). The period 1957–61 has fewer points overall because D_{st} only goes as far back as 1957, despite the fact that the solar

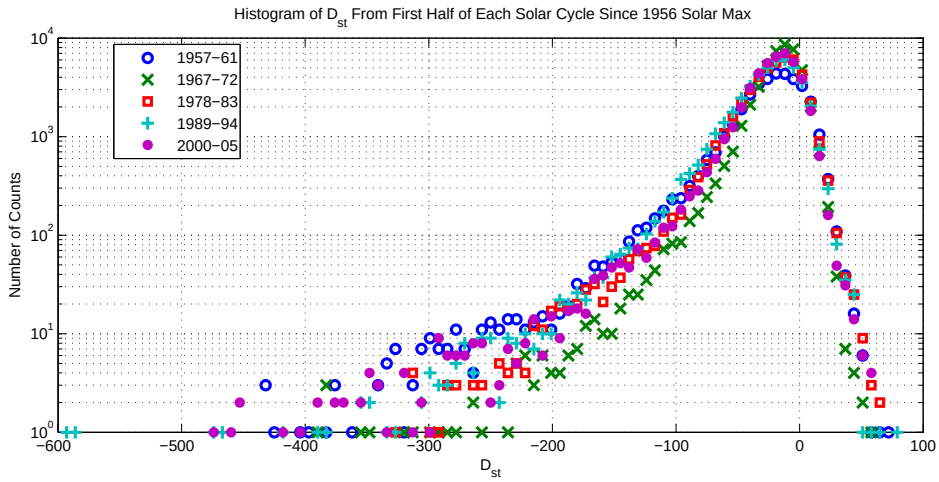

Figure 4.4: Histogram of 5 years post-solar-max for each solar cycle since 1957. The cycle whose max was in 1956 (blue) is underrepresented as there is no D_{st} data for 1956. The 2000–05 half-solar-cycle is plotted in magenta.

maximum year was 1956.

In Figure 4.4 the peak is virtually identical for each solar half-cycle. The tails extending to negative D_{st} values are the most extreme storms. We see here that in the $D_{st} \leq$ -300 nT range there are a number of purple points, indicating that the 2000–05 solar cycle has sampled the far range of a typical solar cycle.

4.5 Summary

WAAS has been in operation during solar maximum and the waning phase of a solar cycle. This work has attempted to show that WAAS has now sampled a typical to higher than average range of ionospheric storms, as measured by D_{st}. Of these days, the ones with extremely low daily D_{st}, e.g. $D_{st} \leq$ -100, and/or WAAS precision service (LPV) availability, are the ones for which supertruth data has been post-processed to check for irregularities. This work indicates that the storms that are used as case studies in Chapters 5 and 6 are representative of near-worst-case storms. Although individual storms may contain many differences, the storm set evaluated by WAAS is in line with historical storms and is expected to represent future storms that will affect WAAS, LAAS, and their users. Storms that are *significantly* worse than those already observed are not expected during future solar cycles.

Table 4.2: Top 50 Geomagnetic Storms by D_{st} ranking.

Rank	Year	Mon (mm)	Day (dd)	D_{st} (nT)	Rank	Year	Mon (mm)	Day (dd)	D_{st} (nT)
1	1989	03	14	-589	26	2000	07	16	-301
2	1989	03	13	-472	27	1991	03	25	-298
2	2003	11	20	-472	28	1958	09	05	-296
4	1959	07	15	-429	29	1958	07	09	-293
5	1957	09	13	-427	30	2001	11	06	-292
6	1958	02	11	-426	31	1982	09	06	-289
7	2003	10	30	-401	31	2000	07	15	-289
8	1967	05	26	-387	31	2004	11	10	-289
8	2001	03	31	-387	34	1992	05	10	-288
10	2004	11	08	-373	34	2000	04	07	-288
11	1991	11	09	-354	36	1960	10	07	-287
12	2003	10	29	-345	36	2000	04	06	-287
13	1960	11	13	-339	38	1970	03	08	-284
14	1958	07	08	-330	39	1959	07	16	-283
15	1960	04	01	-327	40	1990	04	10	-281
16	1960	04	30	-325	40	1991	03	24	-281
16	1982	07	14	-325	42	1957	09	04	-280
18	1957	09	05	-324	42	1991	11	08	-280
19	2003	10	31	-320	44	1960	04	02	-272
19	2003	11	21	-320	44	1961	10	28	-272
21	1967	05	25	-312	46	2001	04	11	-271
22	1981	04	13	-311	47	1989	10	21	-268
23	1986	02	09	-307	48	1989	11	17	-266
24	1957	09	23	-303	49	1986	02	08	-259
25	1958	09	04	-302	50	1970	03	09	-258

Chapter 5

Challenge to LAAS: Spatial Gradients

5.1 Overview

Chapter 3 pointed out that the integrity challenge for LAAS is bounding the impact of large spatial gradients in TEC. The previous chapter pointed out that the most severe irregularities in the ionosphere occurred during extreme storms. In this chapter, data from the 6 April 2000 storm is used as a case study for estimating spatial gradients over LAAS-scale baselines.

The LGF and aircraft separated by some distance on the order of kilometers and viewing the same satellite each suffer an ionospheric delay. These simultaneous delay values will generally differ because the line-of-sight (LOS) of the LGF and the LOS of the aircraft each penetrate different parts of the ionosphere. Theoretically, in the limit as two receivers separation approaches zero, the difference in ionospheric delay for the LOSs should vanish. In practice, when an aircraft approaches the runway and LGF, carrier smoothing of the code introduces a lag between the delays such that they may not be instantaneously identical [Ko, 2000].

The goal of this study is to estimate the maximum spatial decorrelation at kilometer distances and to develop an idea of the LAAS worst-case scenario that must be protected. Dual-frequency GPS data taken by the WAAS network of ground stations are used. In order to analyze the LAAS configuration, the difference in delay along two LOSs and a characteristic separation distance between them must be measured.

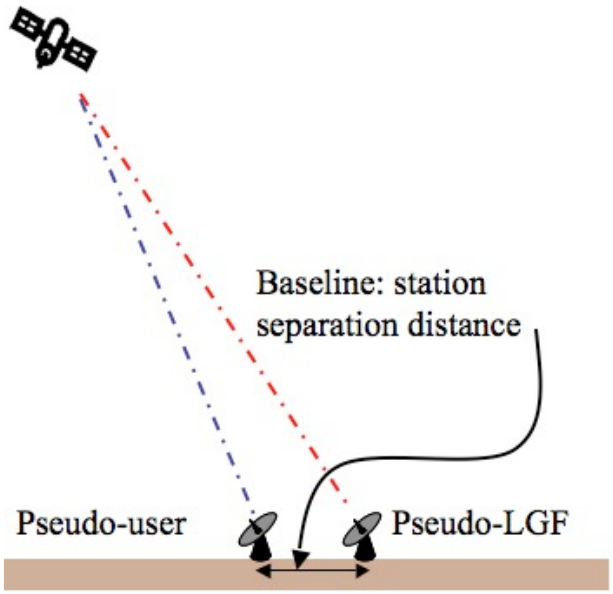

Figure 5.1: Illustration of the station pair configuration.

5.2 Station Pair Configuration

One approach involves considering each pair of WAAS stations as the LGF-aircraft receiver pair. For each epoch, the delays at each of two stations i and j viewing the same satellite k are differenced:

$$\triangle I_{s,stn} = |\tilde{I}^k_{s,i}(t) - \tilde{I}^k_{s,j}(t)| \tag{5.1}$$

This method is illustrated in Figure 5.1. It is fairly intuitive, in that there is an exact analogue to each part of the LAAS configuration in this approach. In the same way that the LGF and the aircraft are separated by some distance, each pair of stations chosen is spatially separated. Just as the LAAS concern is the simultaneous difference in the delays experienced by the LGF and the aircraft, with this method the delays for a single epoch are differenced.

Figure 5.2(a) shows a two-dimensional histogram of the number of observations as a function of both the WAAS station separation distance and the difference in the slant ionospheric delay, $\triangle I_{s,stn}$, for 2 July 2000, which exhibited nominal ionospheric behavior. This histogram was developed by counting the number of instances for which a particular

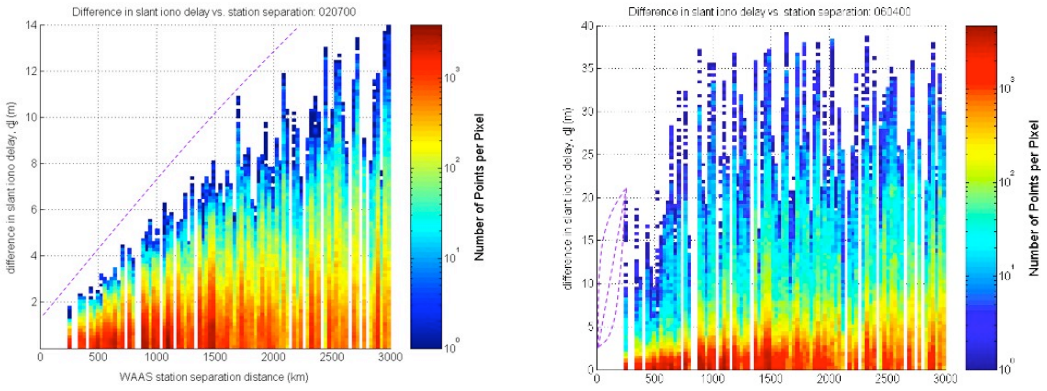

(a) Nominal (b) Stormy

Figure 5.2: Difference in slant ionospheric delay as a function of station separation distance.

separation distance yielded a particular difference in slant delay as the two stations tracked the same satellite. The horizontal axis divides station separation distances into bins, and the vertical axis divides measurements of the difference in slant delay into bins. The color of each pixel indicates the number of instances counted, on a logarithmic scale that spans more than 10^3 observations.

To protect a user in all cases, the greatest difference in delay observed for each separation distance must be bounded. Although the station pair method has been used before [Klobuchar *et al.*, 1993], it has certain limitations when applied to the LAAS scenario. First of all, the sampling over distance is discretized because the reference station locations are fixed. This results in segments of the x-axis (e.g., the 800 km region) for which there are no data. Also, there are no data for distances less than the smallest station separation (in this case, 255 km). Despite these sampling issues, the fairly smooth behavior approaching the origin on the plot of nominal ionospheric data implies that an upper envelope on the data may provide a bound, in units of millimeters of differential delay per kilometer of separation, on the spatial gradients at distances less than 255 km. Based on the maximum differential delay of 1.8 m observed at the shortest distance, 255 km, the spatial rate of change is bounded by 7.1 mm/km on a nominal day.

However, the two-dimensional histogram for 6 April 2000, on which there was an ionospheric disturbance, indicates otherwise (Figure 5.2(b)). Spatial decorrelation does not occur smoothly enough for a clean envelope of the plot to emerge. Any of the dotted lines drawn at less than 255 km is a possible extrapolation of the spatial decorrelation based on

the data at greater than 255 km.

Between the WRSs separated by 255 km (New York and Boston), the differential slant delay is nearly 20 m. With the supertruth data available, the event of New York and Boston measuring a slant ionospheric delay difference of 20 m appeared to be due to the LOSs straddling a region of high TEC spatial gradient.

Figure 5.2(b) of spatial gradient observations on a known storm day, emphasizes the severity of the sampling limitations of the station pair method. Information is available over receiver separation distances only as short as 255 km, and even the highest observed difference of 20 m at this distance could not be sufficiently confirmed by other measurements such that a decorrelation rate of 78 mm/km could be established as the minimum upper bound. Also the envelope bounding the observations, when extrapolated down to zero separation, does not converge to zero difference. Physically the difference in delay must approach zero as the separation decreases, but it is difficult to determine an accurate model for distances less than 20 km based on this data. Ultimately this method of analysis is insufficient to provide a reliable decorrelation rate envelope at the 10 km distance separation, given the density of the WAAS station network.

5.3 Time Step Configuration

An alternate approach to bounding ionospheric decorrelation for LAAS is chosen to gain sufficient sampling at distances less than 255 km. With this configuration, ionospheric delay from a single satellite to a single station at one epoch is compared to the delay for the same LOS 100n seconds later (n = 1,2,3...) up to an hour later.

$$\triangle I_{v,time} = |\tilde{I}^k_{v,i}(t) - \tilde{I}^k_{v,i}(t + 100n)|,\ n = 1, 2, 3, ...36 \tag{5.2}$$

The difference in the vertical ionospheric delay of a single LOS between time t = 0 and t = 100 s, then between t = 0 and t = 200 s, and so on, is computed. Working with data from a single LOS eliminates receiver and satellite biases, but ionospheric dynamics can corrupt the results. A quasi-static ionosphere is assumed over this time scale so that temporal decorrelation approximates spatial decorrelation.

This method has a slightly different configuration from the actual LAAS LGF-aircraft scenario, so the connection it bears to the LAAS scenario may be less intuitive than the station pair method described above. In this situation, only a single station's measurements

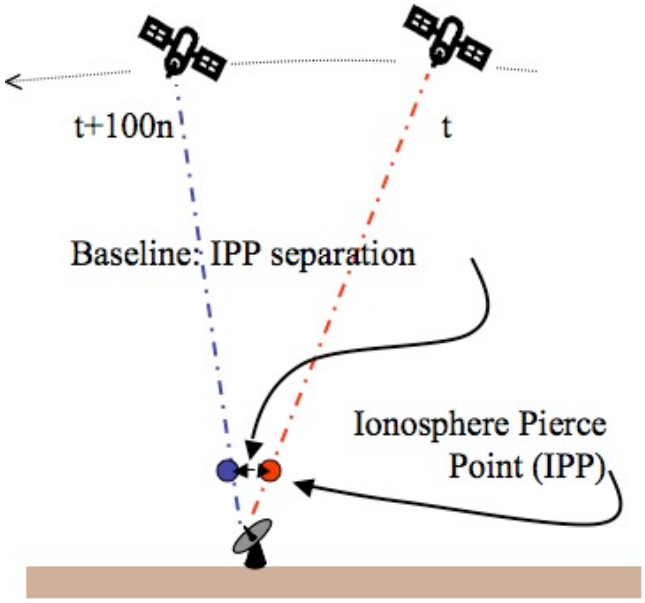

Figure 5.3: Illustration of the time step configuration.

are under consideration, so the ability to equate one WAAS station to the LGF and a different WAAS station to the aircraft does not hold. It is not exactly possible to equate a station at time t = 0 to the LGF, and the same station at t = 100 s to the aircraft because that single reference station is fixed and effectively the separation distance is 0.

Although this approach bears less architectural resemblance to the LAAS scenario of interest, the reason that it achieves the same purpose as the station pair method is that over a time interval of seconds or even minutes, the elevation and azimuth angle of a single orbiting GPS satellite at both times are similar. As a result, the LOSs slice through neighboring regions of the ionosphere. This achieves the same effect as an LGF receiver and an aircraft receiver whose LOSs to a given satellite penetrate neighboring areas of the ionosphere. In the LAAS configuration under study, the LGF and aircraft view a given satellite at similar elevation and azimuth angles.

This method, therefore, allows for the comparison of similar regions of the ionosphere in measurements of difference in ionospheric delay. Since the reference station is fixed, though, the characteristic spatial separation distance between the two measurements must be redefined. The ionosphere, assumed in the thin shell model to be at an altitude of 350 km, is much closer to the LGF and aircraft than it is to the GPS satellite, which orbits at

a height of about 20,000 km. For this reason, the IPPs associated with the LGF and the aircraft have a separation distance similar to the LGF-aircraft separation. In characterizing spatial decorrelation, then, IPP separation is treated as the characteristic length. In the "time step" method, there is only one receiver under consideration, but the IPP moves over time because the satellite is orbiting. In the time step approach, the IPP separation is the characteristic distance taken as most analogous to that between the LGF and the aircraft.

In order to determine that the time step method overcomes the limitations that the station pair method has, the two-dimensional histograms for 6 April 2000, as generated by each method of analysis, are compared. In order to compare the two methods, the station pair histogram is modified from its form in Figure 5.2(b) to count observations as a function of zenith (rather than slant) delay and as a function not of station separation distance, but of IPP separation. The vertical delay, $\tilde{I}_v$, is computed from the slant using Equation (2.29) with a 350 km shell height.

$$\triangle I_{v,stn} = |\tilde{I}^k_{v,i}(t) - \tilde{I}^k_{v,j}(t)| \tag{5.3}$$

$$\tag{5.4}$$

Figure 5.4 compares the two dimensional histograms as a function of IPP separation and vertical ionospheric delay via: (a) the station pair method, and (b) the time step method. The horizontal axis subdivides IPP separation distances into bins of width 40 km. The vertical axis separates the vertical ionospheric delay into 0.3 m bins. On both plots, the color indicates number of observations, but the scale is different for each plot. On Figure 5.4(a), dark red indicates 5000 observations, whereas for Figure 5.4(b) dark red indicates over 13,000 observations.

Overall the time step method achieves greater sampling. For IPP separation less than 100 km, in particular, the time step method yields extremely high sampling, compared with the complete lack of data in that range on Figure 5.4(a). Figure 5.4(b), a two dimensional histogram via the time step method, has high sampling at the kilometer range.

With the time step method, the bounding envelope peaks at under 200 km with a highest observed vertical delay of nearly 17 meters. Even for separation distances between 0 and 40 km, there are differences in vertical delay as great as 9 m. These high gradients observed by the time step method conservatively bound the highest gradients (i.e., 10 m vertical delay

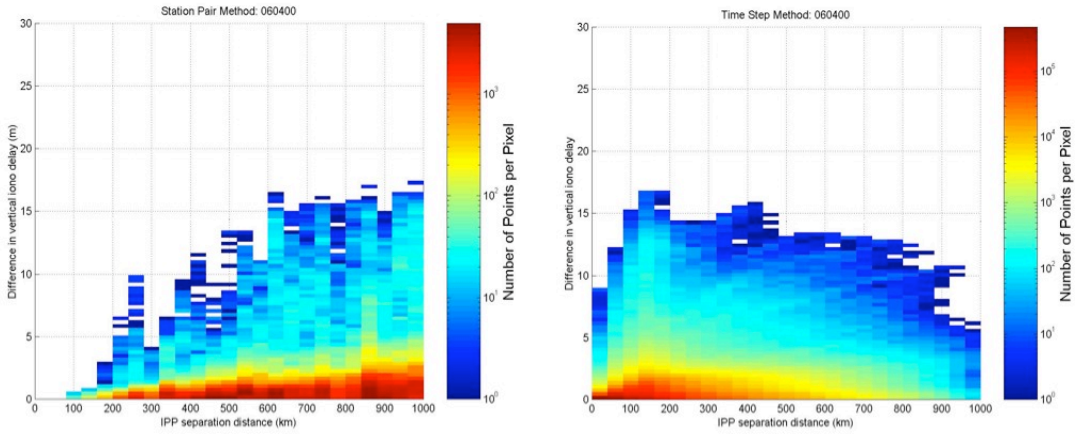

(a) Station Pair (b) Time Step

Figure 5.4: Comparison of difference in zenith ionospheric delay (m) as a function of IPP separation distance (km) for two methods of analysis.

at 250 km separation) estimated by the station pair method. Calculating the decorrelation rate based on the Time Step approach should overbound the actual scenario. This method permits a more conservative estimate of the decorrelation rate than the station pair method.

The fact that the envelope curve for Figure 5.4(b) decreases as the IPP separation increases beyond 200 km is most likely an effect of differencing measurements over time spans of up to only an hour. For a low elevation satellite, an IPP to a station may cover a great distance in under an hour. In general, though, greater IPP separations may result from longer time intervals (i.e., greater than one hour) during which the satellite orbits. As a result, at greater IPP separation distances, sampling becomes less complete. In any case, at the sub-100-km distance scale of interest for LAAS applications, the time step method defines an envelope.

Having checked the viability of the time step configuration as a method of analysis for the LAAS scenario, we produce a higher resolution two-dimensional histogram to see the finer structure to the bounding envelope at distances less than 100 km. For this analysis, time intervals of 10n (n = 1,2,3...) seconds, up to an hour later are considered.

$$\triangle I_{v,time} = |\tilde{I}^k_{v,i}(t) - \tilde{I}^k_{v,i}(t + 10n)|,\ n = 1, 2, 3, ...360 \tag{5.5}$$

Figure 5.5 is a two-dimensional histogram counting the number of events as a function of the IPP separation and the difference in the zenith ionospheric delay, $\triangle I_{v,time}$, on

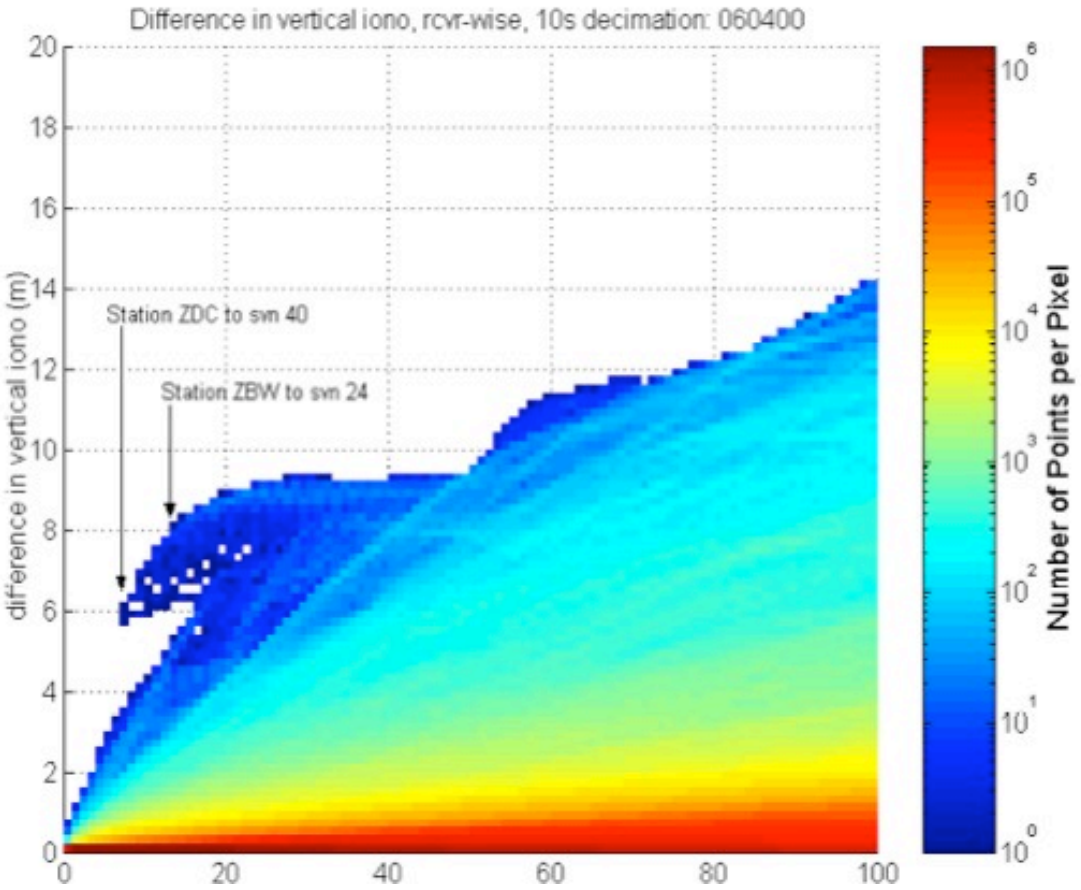

Figure 5.5: Difference in zenith ionospheric delay as a function of IPP separation during an ionospheric storm.

6 April 2000. The x-axis divides the IPP separation distance into kilometer-wide bins. The y-axis divides the measured $\triangle I_{v,time}$ into bins of width 0.2 m. The color represents the number of observations on a logarithmic scale, with dark red indicating nearly two million observations. The data can be enveloped by a curve that converges to nearly zero at the origin, and whose steepest slope is the upper bound on the decorrelation rate.

The point on Figure 5.5 that defines the highest decorrelation rate observed occurs at 7 km, with an observed difference in vertical delay, $\triangle I_{v,time} = 6$ m. This is unexpectedly large and is investigated further. The highest gradient observed via the time step method occurred from the WAAS station at Washington, D.C., as it tracked SVN 40 in the local mid-afternoon. As the next section will show with the raw data, over a time span of two

minutes the vertical ionospheric delay apparently dropped 6 m.

5.4 Verification with Raw Data

To verify that at an IPP separation of 7 km the WRS at Washington, D.C., (designated ZDC) measured a change in vertical delay to SVN 40 of $\triangle I_{v,time} = 6$ m, the raw data from ZDC is considered. In this way, cycle slips or any smoothing and bias removal processes that might have yielded misleading results would be visible. Figure 5.6 shows the slant ionospheric delay in meters at each of the three receivers at station ZDC as they track GPS satellite number 40 over time, measured in three ways at each receiver.

The red line shows the ionospheric delay, I_ρ, at the L1 frequency as measured by the L1-L2 code difference. The equation with which pseudorange measurements, ρ_1 and ρ_2, at the L1 and L2 frequencies, respectively, can be used to measure the ionospheric delay, I_ρ, is given by Equation (2.22) in Chapter 2. This measurement of the slant ionospheric delay is the noisiest but is unambiguous. The blue line plots the delay, I_ϕ, at L1 as obtained from the L1 and L2 carrier phase measurements, ϕ_1 and ϕ_2, using Equation (2.24). The carrier measurement of the ionospheric delay is significantly less noisy than the code measurement. Due to the integer ambiguity of each carrier phase measurement, this measurement, I_ϕ, of the delay is offset from the correct absolute value and was re-centered using the time-averaged code measurement, I_ρ. The green line is one-half the code-carrier divergence at L1, given by Equation (2.20). The measurement of the ionospheric delay using only the L1 band, I_{ccd}, also contains an ambiguity and is re-centered with the time-averaged code measurement of the delay, I_ρ. The epochs that produced 6 m vertical delay difference at 7 km IPP separation are marked with vertical lines. The horizontal axis below each plot marks the elapsed time in seconds.

Several features are apparent in Figure 5.6. First, it is clear there were no cycle slips for any of the receivers during the time interval in question. Second, all three receivers behave qualitatively identically. The curves for Receiver 1 are offset by about 2 m with respect to the curves for Receivers 2 and 3. This may have affected the voting process and contributed to the several second outage in the supertruth data. However, the identical time-evolution shown by all three receivers indicates that the observed anomaly was not due to receiver bias. At each receiver, the three forms of slant delay measurement — code (I_ρ), carrier (I_ϕ), and code-carrier divergence (I_{ccd}) — drop by the same amount. At each receiver, both the

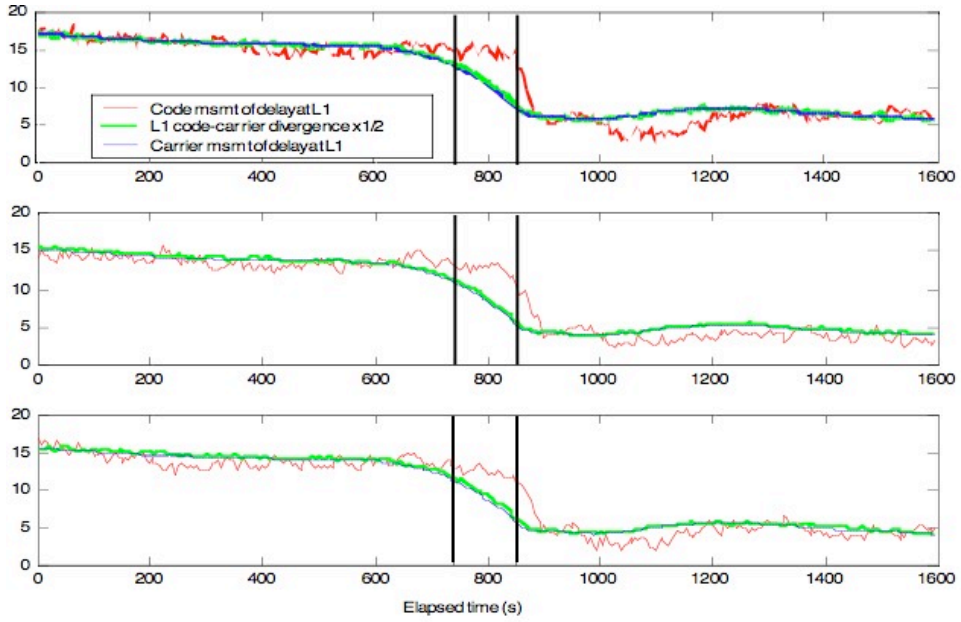

Figure 5.6: Slant ionospheric delay in meters to SVN 40 from each receiver at Washington, D.C., WAAS station.

code measurement of the ionospheric slant delay (red) and code-carrier divergence (green) lag the carrier phase measurement (blue), the former to a significant extent. This behavior is an artifact of carrier smoothing of the code measurement, with a 5 s filter time constant for the L1 frequency and a 15 s time constant for the L2 frequency [Walter *et al.*, 2004]. These time constants correspond to the carrier smoothing, or "C-smooth," values [Novatel, 1997] that were in effect for WAAS on 6 April 2000. Over a time interval of 110 s, the beginning and end of which are marked with vertical lines on Figure 5.6, the IPP tracked through a drop in the slant ionospheric delay of about 8 m, which corresponds to a zenith delay of 6 m, as was observed on Figure 5.5. The data indicate that, on 6 April 2000, while station ZDC tracked SVN 40 during a time span of 110 s, corresponding to an IPP traversal of 7 km, the IPP crossed an ionospheric front that caused a drop in zenith delay of 6 m.

From Figure 5.5, an independent LOS can be found to further confirm the ZDC-SVN40 anomaly. In this case, the LOS that produced $\triangle I_v = 8$ m at an IPP separation of 15 km occurred between the Boston WRS (ZBW) and SVN 24. The raw data measurements of the ionosphere for this LOS over the time interval it exhibited its highest gradient in the supertruth data are shown in Figure 5.7. The raw data for Receiver 2 at ZBW were not

available. The horizontal axis denotes elapsed time in seconds, and the vertical axis marks magnitude of the slant ionospheric delay in meters. The epochs whose difference produced the point identified on the histogram in Figure 5.5 for the LOS between ZBW and SVN 24 are marked with vertical lines. The red line is the dual frequency code measurement of the ionospheric delay, I_ρ, at frequency L1, as given by Equation (2.22). The blue curve shows the dual frequency carrier phase measurement of the ionospheric delay, I_ϕ (Equation (2.24)), and has been recentered to the mean of the code measurement, I_ρ, to remove the integer ambiguity. The green curve illustrates the single-frequency code-carrier divergence measurement of the ionospheric error, I_{ccd}, as given by Equation (2.20) in Chapter 2.

Receivers 1 and 3 at station ZBW both exhibit similar drops in the measured slant delay. At each receiver the drop in delay appears in all three forms of measurement: code (red), carrier (blue), and code-carrier divergence (green). The code measurement lags the carrier and code-carrier divergence delay measurements. This is, again, a byproduct of the carrier-aided smoothing process that takes place on each frequency's pseudorange measurement, ρ_1 and ρ_2. From Figure 5.7 it appears that, while station ZBW tracked SVN 24, during a span of 150 s, the slant ionospheric delay measured dropped 10 m. These values are consistent with the ones implied by the supertruth data analysis in Figure 5.5. An IPP traversal of 15 km corresponds to 150 s, and a 10 m slant delay corresponds to about 8 m zenith delay, given SVN 24's position in the sky during the time interval.

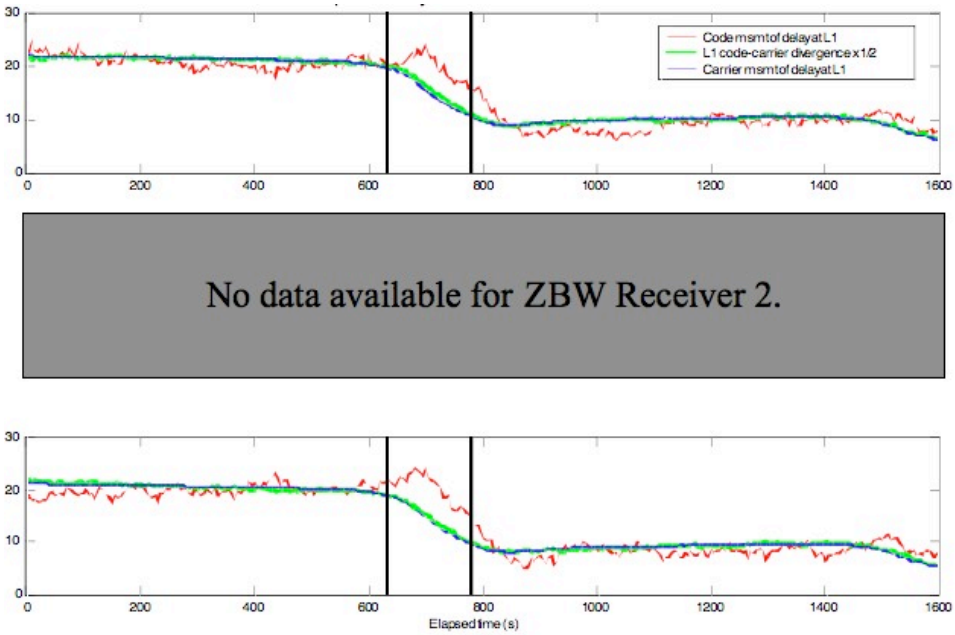

Figure 5.7: Slant ionospheric delay in meters to SVN 24 from each receiver at Boston WAAS station. Data for Receiver 2 not available.

5.5 Analysis of Anomalies Observed

In Section 5.3 supertruth data was used to identify two instances of particularly high gradients over IPP separation distances of several kilometers. In one case the anomaly in question was associated with the Washington, D.C., WRS and SVN 40. In the other case an anomaly was associated with the Boston WRS and SVN 24 an hour and a half earlier in the day. The fact that two independent lines-of-sight exhibited high gradients seems to indicate that neither biases at an individual receiver or satellite nor cycle slips contributed to the high apparent decorrelation. In each instance of anomalous behavior, the redundant receivers' raw data measurements each corroborate the others'. In each case the anomaly affected both the L1 and L2 frequencies, as evidenced by the code, carrier, and code-carrier divergence measurements of the ionospheric delay from the raw data. Alternate sources of error have been ruled out by this cross-verification. The anomalous events that affected LOS ZDC-SVN 40 and LOS ZBW-SVN 24 were both records of actual ionospheric events. However, the gradients they imply (8 m over 7 km separation and 10 m per 15 km) may be artificially inflated for the following reason. The anomaly at station ZBW as it tracked SVN

24 preceded the anomaly along LOS ZDC-SVN 40 by 1.5 hours. The IPP maps for this storm period shown in Figures B.1 and B.2 of Appendix B roughly indicate that the storm front whose boundary runs roughly east-west recedes southward for the duration. Having first been traversed by an IPP from station ZBW, it progresses south to be traversed by an IPP from ZDC an hour and a half later.

This implies that the storm front is moving at a rate comparable to the IPP velocities. With the time step method a quasi-static ionosphere was assumed, so that temporal gradients were equivalent to spatial (IPP separation) gradients. If the same ionospheric storm front was near Boston on the afternoon of 6 April 2000, and then was near Washington, D.C., 1.5 hours later that day, then to first order its velocity was 110 m/s southward. Over this same time interval, the IPPs associated with ZBW-SVN 24 and ZDC-SVN 40 were moving primarily northward with ground speeds of 7 km/110 s = 63 m/s and 15 km/150 s = 100 m/s, respectively. The velocity of the storm front is non-negligible compared to the IPP velocities. Since the velocities were directed roughly opposite to each other, the effect of the addition of the relative velocities would make the spatial gradient in the ionosphere appear to be a factor of two or more worse than it actually was. For example, recall that, for the LOS ZDC-SVN 40, over a span of 110 s the IPP traversed 7 km, and the difference in vertical ionospheric delay was 6 m. During that 110 s interval, assuming the front had a ground speed of 110 m/s, the storm front would have traveled 12 km. In the time that the IPP moved north 7 km, the ionospheric front moved south 12 km. This means that the purely spatial gradient of the ionosphere was more likely 6 m vertical difference over a 19 km range than over 7 km. A change in delay of 6 m over 19 km corresponds to 315 mm/km spatial rate of change.

5.6 Summary

A method of analyzing dual-frequency GPS data from nearby reference receivers was described in this chapter. It has been applied to nominal and even moderately stormy GPS data to show that typical spatial decorrelation is on the order of 5 mm/km [Lee *et al.*, 2006b].

In contrast, from WAAS supertruth and raw WRS data, it appears that the 315 mm/km spatial decorrelation estimated on 6 April 2000 is due to an actual ionospheric event. Over a span of a couple of hours, a wall running east-west with a large north-south gradient

moved southward. This occurrence is corroborated by colocated receivers exhibiting similar response, as well as independent lines of sight. The observation is unlikely to be an artifact of codeless L2 tracking because L1-only processing was affected identically.

The results of these estimates of the maximum spatial gradient observed using WAAS supertruth data have been further validated with CORS data from the October 2003 and November 2003 storms ([Ene *et al.*, 2005] and [Dehel *et al.*, 2004]). The ionosphere threat models for LAAS now include spatial rates of change up to 425 mm/km. These estimates of spatial decorrelation have been used to build an ionospheric model for the LAAS Integrity Monitoring Testbed (IMT) simulation [Luo *et al.*, 2003]. The ionosphere is modeled as a ramp in delay as a function of distance. The model is parameterized by the slope of the ramp, its width, and the ground speed at which it travels.

This chapter's analysis highlights the primary limitation of the time step method in analyzing supertruth data: that spatial and temporal variation effects are mixed together when relative speeds are comparable. Integrity Monitoring simulations can easily detect large, fast-moving events [Luo *et al.*, 2004a]. In some cases, though, an ionospheric anomaly, simulated with a speed comparable to IPP speeds or oriented to strike the user before reaching the LGF, cannot be detected.

Simulation of satellite constellation, aircraft position, LGF position, and ionosphere ramp position have shown that certain combinations of relative speeds and geometries can remain undetected and produce positioning errors of many meters [Luo *et al.*, 2004b]. An additional factor in the build-up of user ionosphere error is the lag introduced by the carrier smoothing of the code at the aircraft and at the LGF [Ko, 2000]. This has been further verified by using data from nearby (50–100 km) pairs of stations to compute differential corrections [Park *et al.*, 2007].

Users can be protected from these situations by inflating the protection bound that is broadcast to exclude geometries that would lead to intolerably large positioning errors [Lee *et al.*, 2006a]. Even though there is no evidence of such large gradients on nominal days, without some kind of storm detector, LAAS must assume that the ionosphere may be in a disturbed state at all times. As a result, disallowing geometries that would be unsafe during a storm when there may not actually be a storm trades off precision approach availability. A method for excluding geometries that achieves an acceptable level of availability is nearly finalized by the FAA.

Chapter 6

Challenge to WAAS: Localized Irregularities

6.1 Overview

Chapter 3 explained why irregularities that fall between SBAS measurements are an integrity threat. Chapter 4 introduced one of the worst storms of Solar Cycle 23, which occurred 29–31 October 2003. In this ionosphere storm an extremely localized and long-lasting enhancement occurred during local nighttime. The enhanced TEC region contained about 10 m higher delay than the nighttime background ionosphere TEC. The events of the ionospheric storm prior to this localized anomalous region are reviewed in Section 6.2. The localized enhancement was sampled by the WAAS network and therefore triggered the Irregularity Detector to protect users in the area. The horizontal area of the enhancement was typical of the area between WAAS measurements. What if such an anomaly existed in the ionosphere and the WRS network did *not* measure it? Safety requires that either this state must always be detected or this state must always be assumed to exist. Absent the storm detector, such high broadcast bounds (GIVEs) would be needed that LPV service would effectively never be available to users. Instead, the extreme storm detector has built into it several hours of hysteresis. The χ^2 goodness-of-fit ratio discussed in Chapter 4 must be below the threshold for eight hours before the GIVEs can be reset to low values.

The goal of this chapter is to understand where the electrons in the enhancement region are located, in three dimensions. It is a step toward estimating how long such an enhancement could persist without recombining. Recombination rates of ions and electrons

are governed by their densities, which are typically altitude-dependent. An estimate of the duration of such an enhancement can verify that the eight-hour hysteresis of the Extreme Storm Detector is sufficient. With a much greater understanding of the phenomenon — why it lasts for so many hours and why it is ground-fixed — it may even be possible to reduce the duration of the hysteresis in the future, improving precision navigation service availability.

The challenge in developing a data-driven three-dimensional model is that the ground-based TEC measurements discussed in Section 6.3, while sensitive to horizontal variations, are insensitive to vertical variations. For this reason, space-based TEC data are used as well. This work reports TEC measurements taken by two satellites, Jason and SAC-C. Jason passed over the enhancement at its orbital altitude of 1300 km at 00:00 EST on 31 October 2003. Using the dual-frequency altimeter on board Jason, Section 6.4.1 shows that nearly all of the electron content is below 1300 km. SAC-C passed directly through the feature at an altitude of about 700 km at 22:30 EST on 30 October 2003. GPS measurements shown in Section 6.4.2 from the receiver on board SAC-C indicate that some portion of the electron content exists above the orbit altitude of SAC-C. Section 6.5 investigates how consistent this feature is with nighttime density profiles from the International Reference Ionosphere model, when the peak density and peak height are constrained to be consistent with ground data.

6.2 A Series of Unfortunate Events?

On 29 October 2003 at 6:13 UT, the first of a sequence of coronal mass ejections (CMEs) from the sun arrived at Earth, initiating a worldwide geomagnetic and ionospheric disturbance lasting from 29–31 October 2003, known as the "Halloween storm of 2003" [Balch *et al.*, 2004]. Significant plasma uplift of a dayside storm-enhanced density (SED) during this storm was reported by Mannucci et al. [2005], and for other large geomagnetic storms during daytime [Tsurutani *et al.*, 2004] and at night [Greenspan *et al.*, 1991]. A general summary of observations made by SOHO, ACE, and the GOES satellites is found at [Balch *et al.*, 2004] and reviewed below. Such energetic input to Earth's space environment is known to have an impact on power systems, HF radio communications, satellite operations, and navigation. As a GPS navigation aid, the FAA's Wide Area Augmentation System (WAAS) was no exception [Doherty *et al.*, 2004].

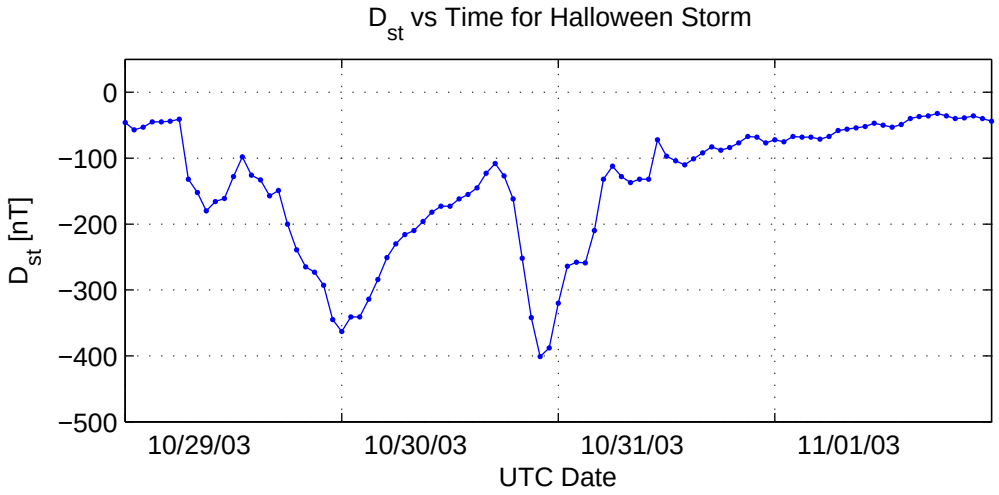

Figure 6.1: D_{st} index 29–31 October 2003.

A second CME released from the sun at 20:49 UT on 29 October impacted the geomagnetic field at around 16:00 UT on 30 October. The geostationary satellites GOES 10, 11, and 12 observed the magnetopause boundary for several hours. The B_z component of the interplanetary magnetic field (IMF) as measured by the ACE satellite turned and remained southward at 15–30 nanoTesla (nT) for several hours subsequently. It is known that geomagnetic activity is associated with periods of southward B_z [Tascione, 1994]. However, the direct relationship, due to magnetic reconnection, is not completely understood. As B_z turns southward, the magnetic field lines of the solar wind connect with the field lines of Earth's geomagnetic field, resulting in particle and energy input to the near-Earth environment. One effect of southward B_z is an increase in the ring current, which effectively reduces the strength of the geomagnetic field. This field strength reduction is measured by ground-based magnetometers and recorded as a drop in the hourly measure, D_{st}, of the Disturbance, storm-time. The D_{st} measurements for the Halloween storm are shown in Figure 6.1. Shortly after the SED swept westward past the southeastern United States on 30 October, at 23:00 UT (18:00 EST) a localized TEC enhancement appeared. This is during the main phase of the storm, following the second sudden storm commencement at the end of UT October 30th.

The enhancement remained many TEC units (TECU) higher than the background ionosphere for several hours. This led to the hypothesis that the feature consisted of plasma at

higher altitudes than surrounding regions, where recombination rates are reduced [Schunk and Nagy, 2000]. Plasma uplift is a plausible mechanism for maintaining large TEC values at night, although the localized nature of the enhancement requires further explanation.

6.3 Evolution of the Enhancement

To study the localized TEC region ground-based measurements from nearly 400 receivers in the US and Mexico from both the CORS network and the IGS network are used. In addition data from the FAA's WAAS network and the CANAPE network are available. The processing for these data is described in Chapter 2. A sequence of TEC maps combining all these dual frequency GPS measurements is shown in Figure 6.2.

These maps are snapshots of the equivalent vertical ionospheric delay in meters at L1 in the eastern US and the Caribbean. The color scale varies from blue (0 m) to red (10 m). Ionospheric pierce points (IPPs), assuming a 500 km shell height, are marked with very small black dots, and line segments point from the dots in the direction of the ground station making the measurement. The shell height was chosen based on results by Mannucci et al. [2005] demonstrating that most of the dayside storm enhanced density (SED) observed during the Halloween storm existed above about 400 km altitude, based on CHAMP satellite GPS data. The color variation on the maps is generated by bi-linearly interpolating the equivalent vertical delay within each set of three nearest IPPs and shading the triangle corresponding to the values of that plane, as described in Section 2.3.2.

At 22:00 UT, or 17:00 Eastern Standard Time (EST), the primary SED has already passed by eastern CONUS, as seen in red on the southwest corner of Figure 6.2(a). To the immediate east of the boundary of the SED, at (30° N, 85° W), is a region of lower TEC of about 4 m. The delay over Florida is lower than the SED at about 5–6 m, but to the east are observations of a higher 8–9 m delay. These are probably related to the higher TEC measurements in the Caribbean, but there are not enough IPPs to fill in the region within 20–25° N and 70–75° W.

At 23:00 UT (18:00 EST), shown in Figure 6.2(b), the region of high TEC has spread from the Caribbean northwest to Florida and the states bordering the Gulf of Mexico. It is still a distinct feature from the SED, because a region of low TEC stretching from east of the Yucatan peninsula up to Texas separates the Florida feature from the SED seen in the lower left part of the map.

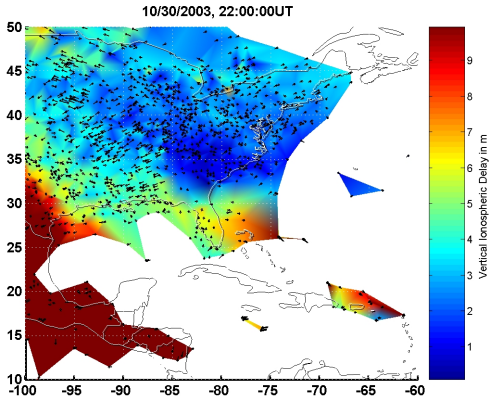

(a) 22:00 UT (17:00 EST).

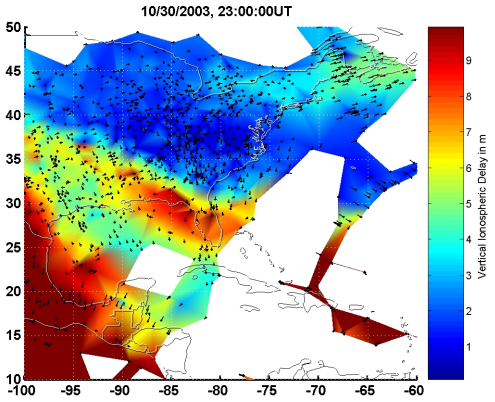

(b) 23:00 UT (18:00 EST).

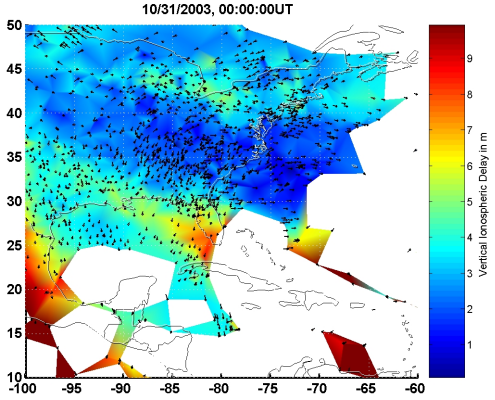

(c) 31 October, 00:00 UT (19:00 EST).

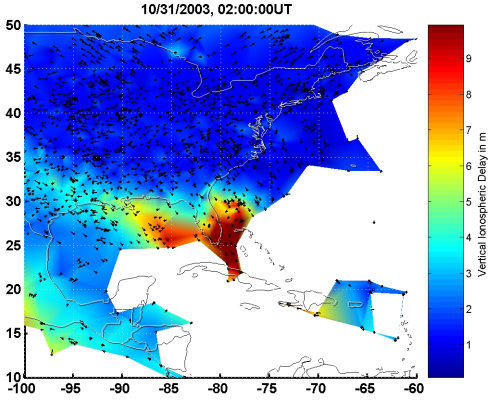

(d) 02:00 UT (21:00 EST).

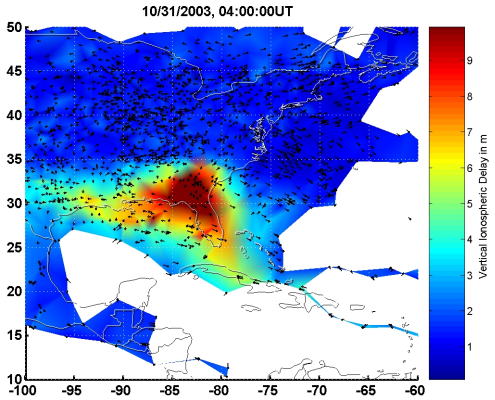

(e) 04:00 UT (23:00 EST).

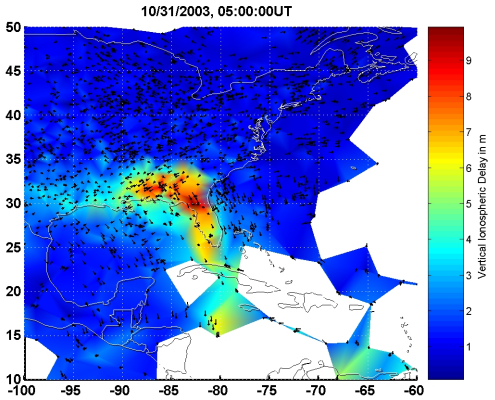

(f) 05:00 UT (31 October, 00:00 EST).

Figure 6.2: 30 October 2003, 22:00 UT – 31 October 2003, 05:00 UT.

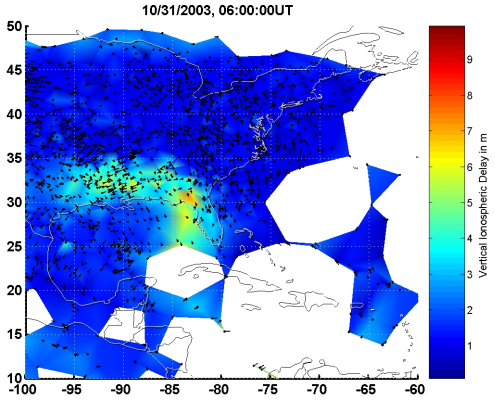

(g) 06:00 UT (01:00 EST).

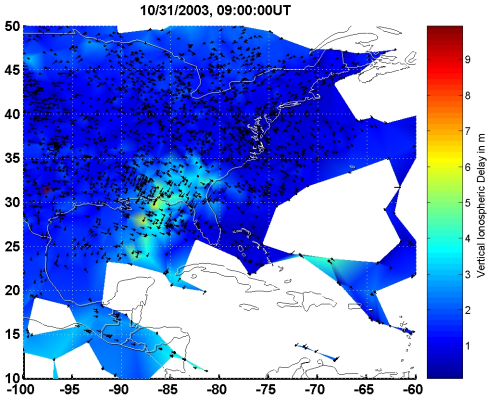

(h) 09:00 UT (04:00 EST).

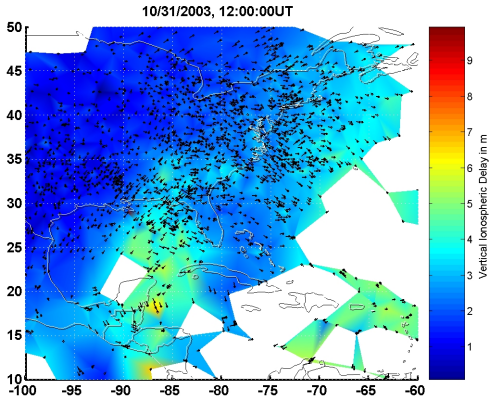

(i) 12:00 UT (07:00 EST).

Figure 6.2: 31 October 2003, 06:00 – 12:00 UT.

By 00:00 UT on 31 October (19:00 EST), the SED has moved west almost completely off the map of Figure 6.2(c), but the edges of the ionospheric feature of interest are still sampled and still located in the Caribbean. The feature continues to have the same orientation northwest-southeast as before. Also visible in this and the previous plot is evidence of the auroral region of higher TEC stretching from the Great Lakes east to New England, though the auroral delays are only a couple meters higher than the background ionization.

Two hours later at 02:00 UT (21:00 EST) on Figure 6.2(d), the auroral region of enhanced TEC has all but disappeared, the background level of nighttime ionization has dropped slightly to about 1 m, and the SED has moved west off the map. However, the localized enhancement (red) remains around the tip of Florida. Due to a lack of data over Cuba, how far south and east it extends is not clear, but measurements over Puerto Rico and Haiti are only around 3 m, indicating that the feature is no longer in that area.

Figure 6.2(e) is a map at 04:00 UT (23:00 EST). The sampling near Cuba seems to indicate that the high density enhancement is confined to the Florida-Georgia region. The measurements in the Caribbean are all around 3 m, lending support to the idea that the feature is now localized to a few degrees of latitude and longitude. However, none of the measurements plotted at Cuba are actually taken overhead at Cuba. Instead these measurements are from other sites viewing low elevation satellites. For this reason it is possible that the feature still extends southward but is not being sampled because the available lines of sight pass under the high-TEC region.

Figure 6.2(f) corresponds to 05:00 UT (local midnight) and is a more detailed version of the map shown in Figure 3.6 of Chapter 3. The feature is fading, as the delays associated with it are declining. It is smaller in apparent extent, confined to Florida and the southern parts of Mississippi, Alabama, and Georgia. As with the previous plot, the apparent localization may be due in part to a lack of GPS ground stations in Cuba. Between Figures 6.2(e) and 6.2(f), the feature appears to have changed shape a bit, but has not moved noticeably.

In Figure 6.2(g), a snapshot of 06:00 UT (01:00 EST), the feature has continued to fade to about 5 m maximum vertical delay compared to the background 1 m. It has similar apparent shape to an hour before (Figure (f)), but has moved slightly to west of the Florida peninsula. Over the next few hours, the density changes shape a bit more and continues to fade, as seen in Figure 6.2(h). However, it does not move out of the Gulf of Mexico area and never fades completely into the background ionization level. In Figure 6.2(i), by noon

UT (07:00 EST), the feature is still about 5 m in delay and better sampling gives it the appearance of being somewhat larger in spatial extent, stretching south to the Yucatan. It is also distinct spatially from the diurnal rise in TEC due to solar ionizing radiation that is just starting to be detectable in the Atlantic.

In summary, the major observations to be made about the enhancement, based on the data throughout CONUS, Mexico, and the Caribbean are that: 1) the high density region convects north and west from equatorial latitudes to southeast CONUS (Figures 6.2(a) – (c)); 2) the feature is part of a larger structure, at least initially, as seen in the Caribbean data; 3) Earth initially rotates under the high density ionosphere, as seen by the apparent westward motion of the SED as it remains in the dusk sector; 4) the feature is relatively stationary after reaching southeast CONUS, implying it co-rotates with Earth (Figures 6.2(d) – (i)); and 5) the feature persists from 17:00 EST through local midnight to the next day. The TEC gradually decreases throughout the night but does not appear to reach the background ionosphere level completely.

6.4 Space-Based Observations

6.4.1 Jason

The Jason satellite, described in Section 2.3.3, orbits at an altitude of about 1300 km and has onboard a downward-pointing dual-frequency altimeter. Measuring the two-way transit time of its dual-frequency signals, the altimeter estimates the vertical TEC in a similar method to dual-frequency GPS. Jason passes over the Gulf of Mexico at local midnight, when the Florida feature is observed from the ground network as illustrated in Figure 6.3(a). The color scale on this map ranges from 0 (blue) to 12 m (red). The ground track of the satellite as it passes from south to north is shown as a shadowed black line. The TECU measurements during this time are shown in Figure 6.3(b). The multiple gaps in the data occur when the satellite passes over land, where its radar altimeter measurements are scattered rather than reflected. The position of Jason and the delay measurement it made at that time are marked at one-minute intervals with a square, triangle, and circle, respectively, on Figures 6.3(a) and (b).

For most of the pass through the northern mid-latitudes, the TEC is around 2–3 m. However, a spike occurs around 05:02:15 UT and decreases afterward. The measurements end abruptly as the satellite passes over Florida. The fact that the measurements rise

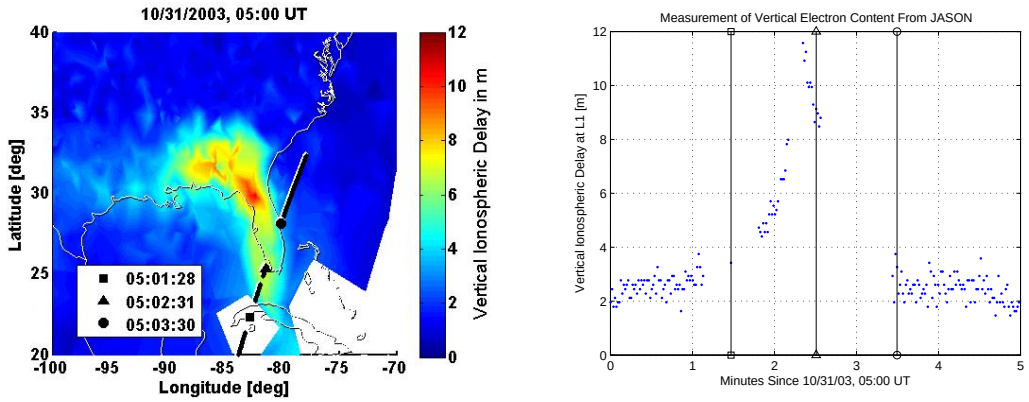

(a) Ground track of Jason satellite from 05:00–05:05 UT on 31 October 2003.

(b) Jason vertical TEC measurements as a function of time.

Figure 6.3: Jason ground track and measurements of TEC 05:00–05:05 UT.

consistently indicate that Jason is not providing spurious data, but is tracing a real TEC enhancement. The peak value of 11.6 m recorded by Jason occurs at geographic latitude and longitude (25° N, 82° W). On the map in Figure 6.3(a), this location is in the Gulf of Mexico west of Miami, essentially at the point marked with the triangle. This is higher than the ground station delay measurements shown in color. Any bias leveling of Jason cannot be greater than 1–2 m since TEC must be non-negative. At most, the Jason peak could be reduced to 10 m. Meanwhile, the ground estimates of delay, based on interpolation between nearby measurements, are around 7–8 m at the Jason location.

It is physically impossible for colocated measurements of TEC between Jason altitude (1300 km) and the ground to be higher than the TEC between the GPS orbit altitude (20000 km) and the ground stations. The bias between Jason and the ground network is most likely due to a number of factors: the fact that the Jason and ground measurements are not colocated, a mapping error due to the assumption of an ionospheric shell and shell height in using Equation (2.29) to convert the ground measurements from slant to equivalent vertical TEC, and the planar interpolation between nearby ground measurements to estimate equivalent vertical delay where there is no data.

Despite this bias between data sets, the Jason vertical measurements of the ionosphere indicate that the vast majority of the enhancement at local midnight is below 1300 km. This is consistent with other findings that the daytime TEC enhancement is above 400 km [Mannucci *et al.*, 2005] and with a super-fountain effect. However, the super-fountain does not predict the co-rotation of the Florida feature that was observed in Figures 6.2(e) – (i).

6.4.2 SAC-C

SAC-C orbits at about 700 km altitude and has a dual-frequency GPS receiver onboard, as described in Section 2.3.3. On 31 October 2003 between 03:25 and 03:35 UT, the SAC-C satellite passed from south to north directly over Florida, as shown with a shadowed solid black line in Figure 6.4(b). The position of SAC-C at 03:30, 03:32, and 03:34 UT are marked with a square, triangle, and circle, respectively. From 03:25–03:35 UT SAC-C tracked several GPS satellites. Shadowed broken line segments point from the position of SAC-C at 03:32 UT toward the six highest GPS satellites, identified by their PRN identification numbers: 4, 5, 7, 10, 17, and 24.

Since the GPS satellites' ground tracks repeat every 23 hours and 56 minutes and SAC-C is sun-synchronous, at 03:40–03:50 UT on 29 October (see Figure 6.4(a)) all satellites were located very near their Earth-referenced positions on 31 October, 03:25–03:35 UT. The SAC-C ground track is indicated with a shadowed solid black line, and its position at 03:42:30, 03:44:30, and 03:46:30 UT are marked with a square, triangle, and circle, respectively. These are the positions nearest to the corresponding positions marked on Figure 6.4(b). Shadowed black broken lines point from SAC-C's position at 03:44:30 UT to the GPS satellites 4, 5, 7, 10, 17, and 24.

The equivalent vertical delay maps based on estimates of $\tilde{I}_v$ from the CORS, IGS, and WAAS ground networks for 29 October 2003 at 03:45 UT and for 31 October 2003 at 03:30 UT are shown in Figures 6.4(a) and (b). The color scale varies from 0–15 m. At 03:45 UT on 29 October, the CME had not yet reached Earth, so the mid-latitude TEC was a nominal nighttime value of about 1–2 m in 6.4(a). Map 6.4(b) shows that the TEC enhancement is localized over Florida in a 700 km by 700 km region. The maximum equivalent vertical TEC in this region is almost 14 m (red) at this time compared to 2–3 m in surrounding regions.

Figure 6.5 shows the slant TEC, $\tilde{I}_s$, in meters of delay at L1, along the lines of sight (LOS) to PRNs 4, 5, 7, 10, 17, and 24. The measurements in Figure 6.5(a) occur from 03:40–03:50 UT on 29 October before storm onset. Figure 6.5(b) plots the measurements made at 03:25–03:35 UT on 31 October. In Figure 6.5(a) the measurements at 03:42:30, 03:44:30, and 03:46:30 UT are marked by vertical lines with squares, triangles, and circles, respectively, at the endpoints. The position of SAC-C at these times is denoted with the corresponding symbol on the TEC map in Figure 6.4(a). The SAC-C slant delay observations on 29 October show no enhancement or rapid change in TEC over the southeastern US on this

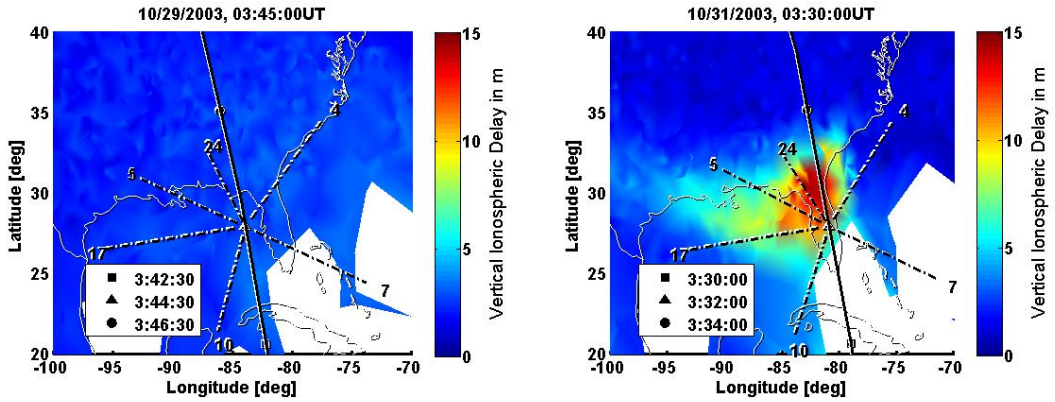

(a) 29 October 2003, 03:40–03:50 UT (b) 31 October 2003, 03:25–03:35 UT

Figure 6.4: SAC-C satellite ground track and ground network measurements of TEC. Black broken line segments point in the direction of the GPS satellites (PRN numbers shown).

night, only background nighttime ionosphere.

In contrast, the SAC-C ionosphere measurements to these same six GPS satellites on 31 October are shown in Figure 6.5(b). Vertical lines denote 03:30, 03:32, and 03:34 UT, with a square, triangle, and circle, respectively. The measurements at these times were taken by SAC-C at the positions marked on Figure 6.4(b). PRNs 5, 10, and 17 are to the west, south, and southwest, respectively. Each of these shows a change of about 4-5 m as SAC-C passes through the feature. The measurements of delay looking northeast to PRN 4 (thin blue dashed line) begin after SAC-C has entered the enhancement region, shortly before 03:30 UT. It shows almost a 2 m drop and has exited the enhancement by 03:34 UT. As SAC-C travels into and out of the feature, it measures a 1.5 m rise to PRN 7 to the southeast at 03:30, travels through the feature, and has dropped 1.5 m again by 03:34.

PRN 24 is at the highest elevation from 03:31 UT onward, at more than 50° and to the northwest during SAC-C passage through the enhancement. As on 29 October, there are no data to PRN 24 from 03:28–03:33 UT during SAC-C passage over Florida. Also, the dual-frequency measurements to PRN 4 to the northeast begin only shortly before passage over Florida. These data outages common to both days indicate possible occultation of the LOS due to SAC-C's own physical apparatus. The similar satellite geometries present on October 29 and October 31 suggest that the measurement differences seen between Figures 6.5(a) and (b) are due to the TEC increase on October 31 and not due to different slant paths from day to day.

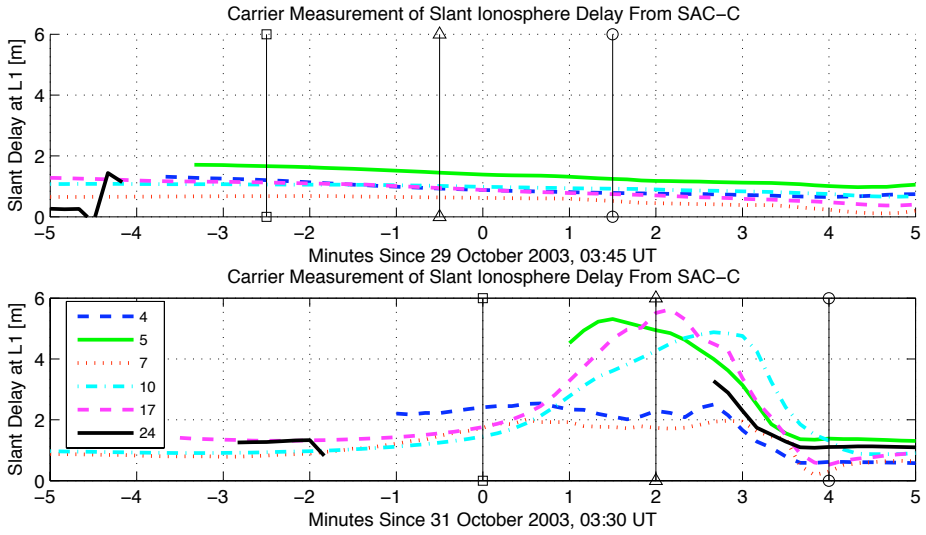

Figure 6.5: SAC-C carrier phase measurements of the ionosphere delay to GPS PRNs 4, 5, 7, 10, 17, and 24 as a function of time on (a) 29 October 2003, 03:40–03:50 UT, and (b) 31 October 2003, 03:25–03:35 UT.

6.5 Three-Dimensional Model of N_e

Under nominal conditions the F2 layer of the ionosphere has a peak density height between 350–450 km. In this section standard electron density profile shapes are used to determine whether the combination of ground and space-borne data are consistent with a high-peak-altitude electron density profile within the enhanced TEC feature over Florida. Recent modeling studies have suggested that ionospheric uplift does not significantly alter profile shapes ([Verkhoglyadova *et al.*, 2006], and [Schunk and Nagy, 2000]). Therefore, it is reasonable to use the International Reference Ionosphere (IRI) as a baseline model for this study in the vicinity of the enhancement even if uplift is a factor contributing to enhanced TEC. The IRI model is a global climatological model that produces electron density profiles for a specified place and time [Bilitza, 2001]. Additional inputs may be used to constrain the model: the maximum electron density (as given by the F2 critical frequency, f_{0F2}) and height, h_{mF2}, at which this peak density occurs. Examples of typical IRI model density profiles were shown in Chapter 1 in Figure 1.5.

A simplified model of the feature is built as follows. A horizontal region of latitude and longitude in which the enhancement occurs is the anomalous region, designated "Region A." A single IRI density profile is chosen to represent this region. The remaining area is

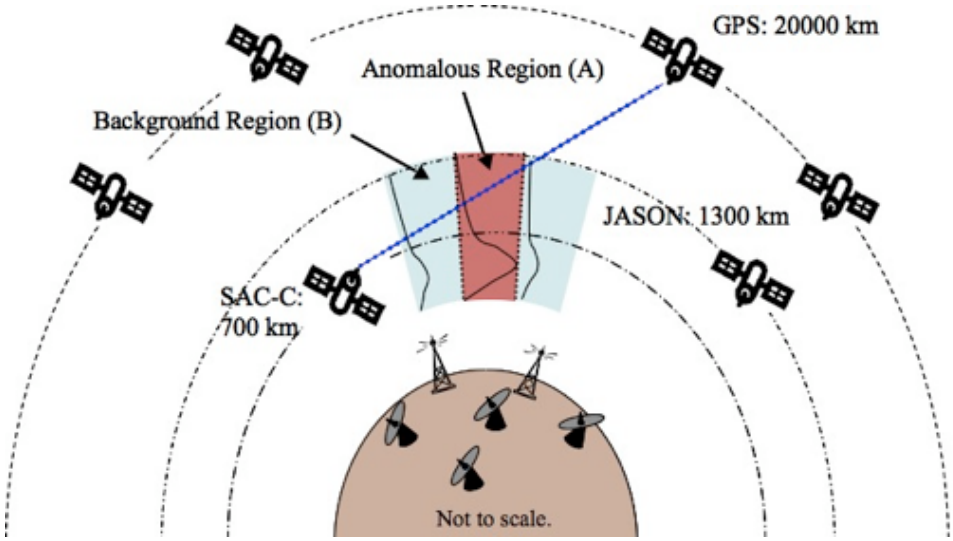

Figure 6.6: Side view of regional three-dimensional electron density model. Not to scale.

the background, "Region B," defined by another IRI density profile. For each SAC-C LOS whose measurements are shown in Figure 6.5(b), the electron density can be integrated along the raypath to predict the SAC-C delay. Figure 6.6 illustrates this method.

Due to SAC-C's altitude, GPS satellites can be tracked at elevations as low as -20 degrees. Raypaths to GPS satellites that are below 0 degrees elevation pass through the ionosphere twice. To avoid the additional complexity this would add, particularly for regions where there are no ground data at all, electron content is integrated only for a GPS satellite whose elevation is greater than 0.

The relationship between ionospheric altitude and IPP location provides a way to estimate the boundary between Regions A and B. For a raypath of given azimuth and elevation angle, higher ionospheric shells produce IPPs farther from the receiver than low ionospheric altitudes. For a given altitude, the horizontal area of a convex region enclosing the enhancement is computed. The IPPs whose equivalent vertical delay, $\tilde{I}_v$, exceeds 7 m are considered to be part of the anomalous region. Figure 6.7 illustrates a side view of this method. The horizontal area of the enhancement region is the horizontal distance between the red IPPs in this one-dimensional cartoon. The area enclosed by the red IPPs gradually decreases with height h_{iono1} as the feature "comes into focus," reaches a minimum near h_{iono2} of 490

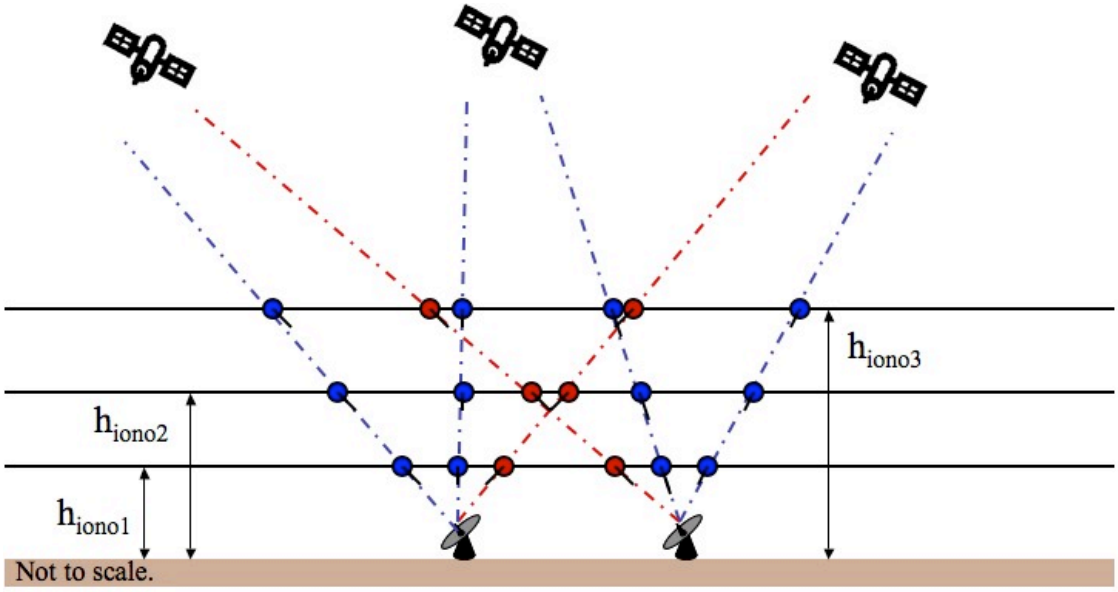

Figure 6.7: Cartoon of how the boundary between regions is selected. The boundary is chosen to enclose the anomalous (red) IPPs such that the area is minimized. This occurs near h_{iono2} in this example.

km altitude, and then increases again for h_{iono3}. The feature is most in "focus" at the ionospheric altitude for which the enhancement area is minimum. In this context, "ionospheric altitude" represents an average altitude or centroid for the profile, which will typically be slightly above the F2 peak density due to the asymmetry of the vertical profile about the peak.

The geographic area included within Region A is outlined on the map in Figure 6.8 as a black line. This is the region defined by all ground measurements whose equivalent vertical delays, $\tilde{I}_v$, are greater than 7 m, plus a vertex at (20° N, 77 ° W). This is a reasonable addition to Region A because Figure 6.2 showed that the feature was elongated north-south later in the night. The addition of this region was found upon iteration to produce greater model accuracy, so the lack of data at this epoch is compensated with knowledge of the feature shape at later epochs.

The next step is to assign possible density profiles to the two regions. For Region A, the integrated electron content of the profile should be on the order of about 14 m of delay to be consistent with the ground station measurements. To get IRI profiles that are close to this, the optional parameter of F2 layer critical frequency, f_{0F2}, must be specified. Nearby

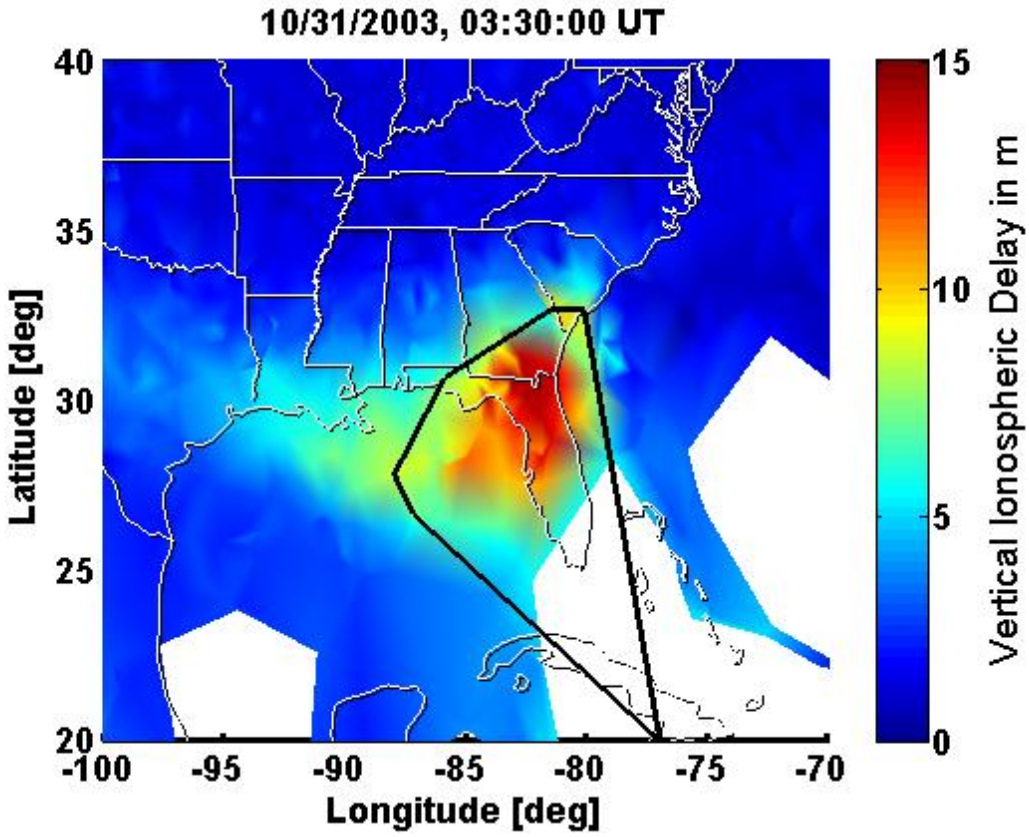

Figure 6.8: Boundary between Regions A (anomalous) and B (background).

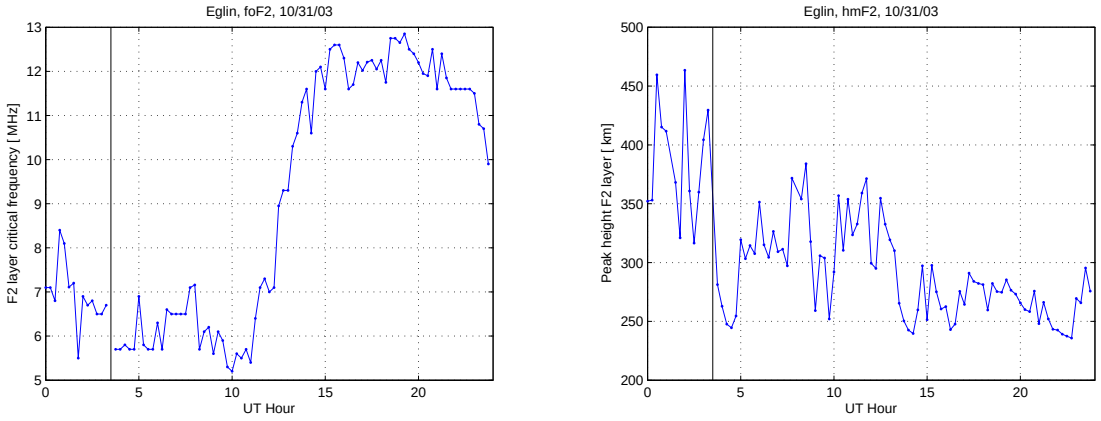

(a) Critical frequency f_{0F2}

(b) Estimated peak height h_{mF2}

Figure 6.9: 31 October 2003, Eglin AFB ionosonde data.

ionosondes can give an estimate of f_{0F2}.

The nearest ionosonde is at Eglin Air Force Base (AFB) at (30.4° N, 86.7° W), as mentioned in Section 2.2. The measurements of f_{0F2} and h_{mF2} on 31 October 2003 are shown in Figure 6.9. A vertical line marks 03:30 UT, the time of interest; there are no data at this time. The values of f_{0F2} measured at times near 03:30 UT are around 6–7 MHz. When used to generate an IRI profile, the 6–7 MHz critical frequencies yield vertical delays of only a few meters. It is also unclear whether Eglin is sensing the anomalous region or background region at this time.

The next ionosonde considered is at Ramey AFB near Arecibo, Puerto Rico. From Figure 6.2(b) the enhancement appears to be above Puerto Rico from 22:00–23:00 UT on 30 October 2003. The Puerto Rico ionosonde data for 30 October shown in Figure 6.10 are noisy, but its reported value of $f_{0F2} = 18.5$ at 22:45 UT, marked with a vertical line, produces an IRI model that gives the same vertical delay as the maximum I_v measured by our ground network, at about 14 m. Thus, a value of $f_{0F2} = 18.5$ MHz is input to the IRI model for Region A.

The height of maximum density, h_{mF2}, is also a parameter that can be input to the IRI model. A range of values for both the peak height and f_{0F2} are evaluated in addition to those indicated by the ionosonde data. The profiles evaluated for Region A are shown in Figure 6.11. The electron density is indicated in cm^{-3} on the horizontal axis and the altitude in km on the vertical.

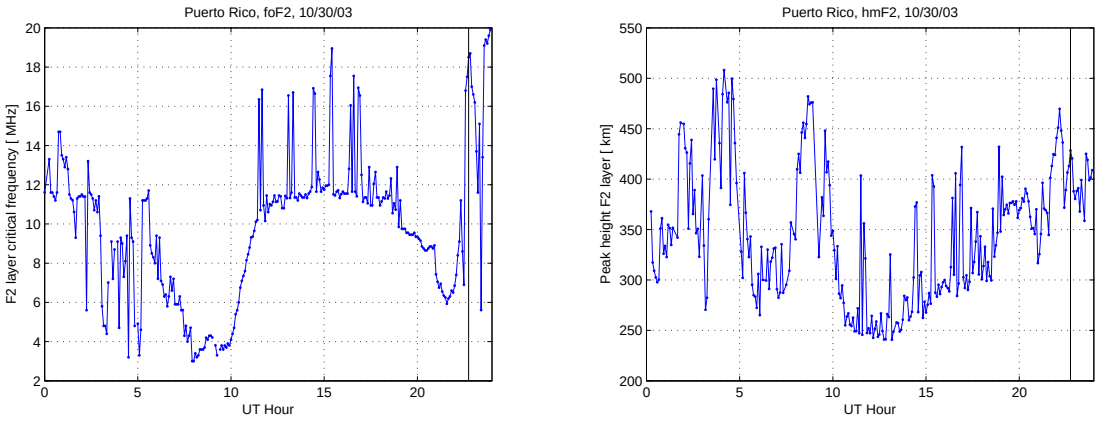

(a) Critical frequency f_{0F2}

(b) Estimated peak height h_{mF2}

Figure 6.10: 30 October 2003, Ramey AFB ionosonde data.

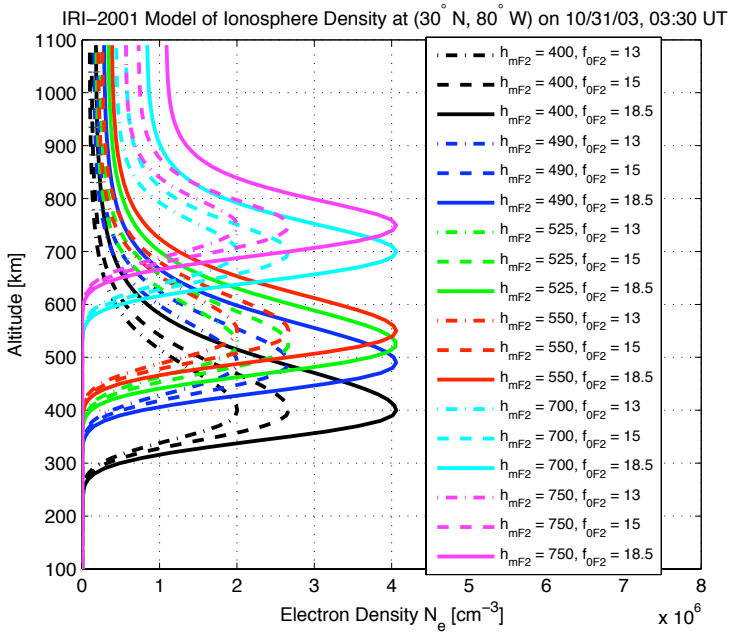

Figure 6.11: International Reference Ionosphere (IRI) electron density models for Region A for different peak heights, h_{mF2}, and densities, corresponding to f_{0F2}, as a function of altitude.

For Region B (background) the height of maximum density and the peak density are specified according to ionosonde measurements at Eglin AFB on 29 October 3:45 UT, before the CME arrived at Earth. The vertical delay produced by an IRI profile generated based on these measurements, about 1 m, agrees with the nighttime delays, $\tilde{I}_v$, measured outside of the TEC enhancement on 31 October. This single profile is used for Region B with each Region A profile tested.

6.6 Analysis

In the previous section, several density profiles were generated for testing against the SAC-C measurements. The predicted SAC-C slant path delay for each line of sight can be computed by integrating through the model, choosing one profile for Region A at a time. Electron density is integrated over altitude, but since the raypath is not always directly vertical, the path length at each point of integration is accounted for by using the obliquity factor in Equation (2.29). For the SAC-C space-borne receiver, R_E becomes Earth's radius plus the altitude of SAC-C, $R_E + h_{sac-c}$, and h_{iono} is taken to be the difference in height between the point of integration on the ray and h_{sac-c}.

Figure 6.12 shows the mean squared error (MSE) on a log scale as a function of time for each of these profiles. The same Region B profile is used in all cases. Every model shows the same MSE before 03:29 UT, when the lines of sight enter the enhancement region, and after they exit at 03:34 UT. The lowest MSEs occur for certain profiles with 490, 525, and 550 km peak heights.

A three-dimensional surface plot of the log of the MSE as a function of h_{mF2} and f_{0F2} over all time is shown in Figure 6.13. The color and the z-axis both indicate the log(MSE). There is no well-defined global minimum. This is to be expected, since vertical density variations are not easily observable with ground GPS measurements. However, there is a shallow minimum for a Region A profile having $h_{mF2} = 490$ km and $f_{0F2} = 18.5$ MHz. The Region A profile that gives this minimum MSE is shown in Figure 6.14 as a black broken line. The blue dashed line shows the Region B profile.

The SAC-C measured slant delays over time are shown in Figure 6.15(a). The predicted delays for each LOS using the electron density model that had the minimum MSE of the ones tested are shown in Figure 6.15(b). Given the simplicity of the model, this figure shows surprising fidelity. The general rise and fall of the delay as SAC-C passes through

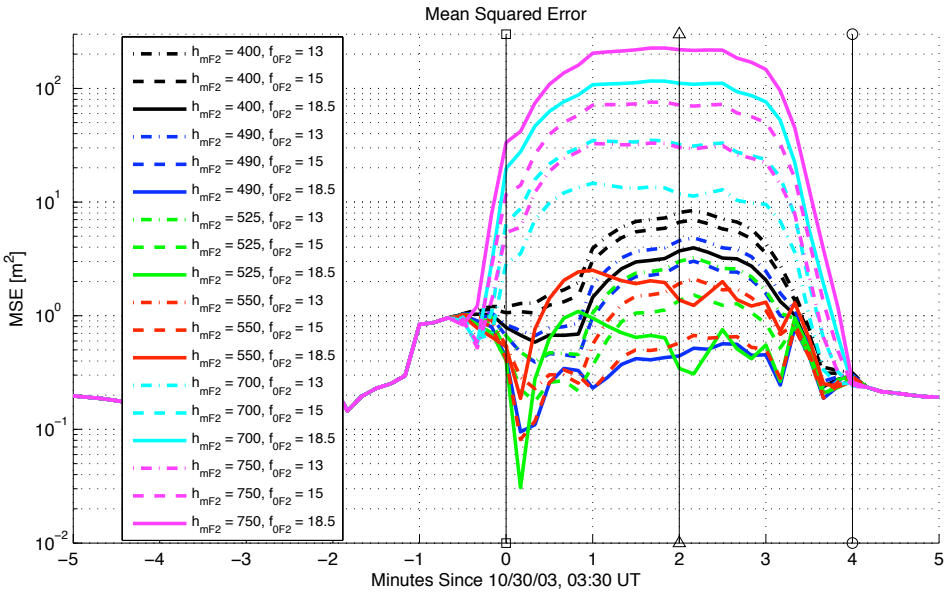

Figure 6.12: Mean squared error as a function of time for Region A density profiles shown in Figure 6.11.

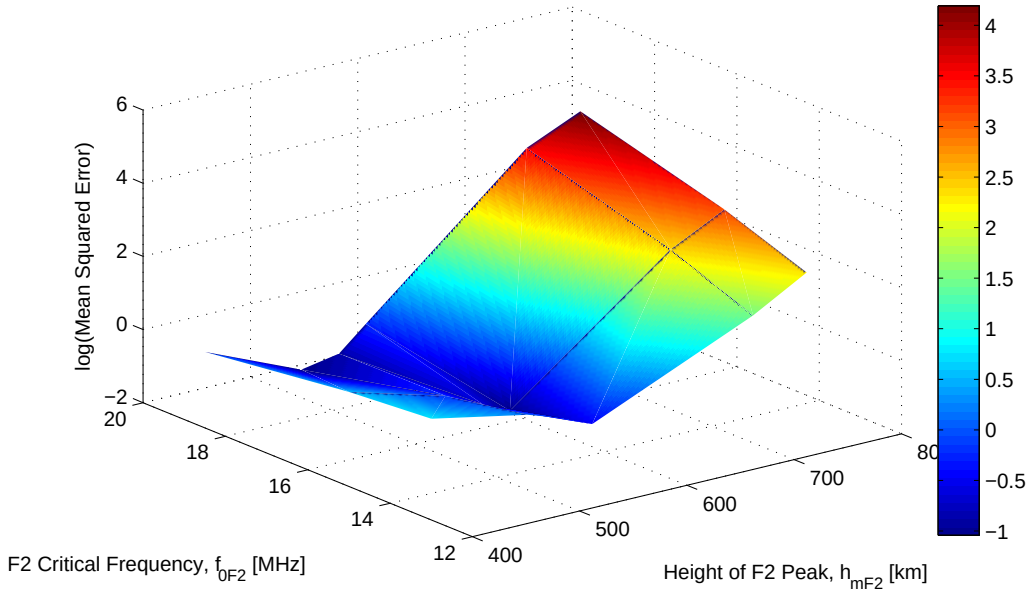

Figure 6.13: Mean squared error as a function of peak height, h_{mF2}, and density, corresponding to f_{0F2}, for Region A density profiles shown in Figure 6.11.

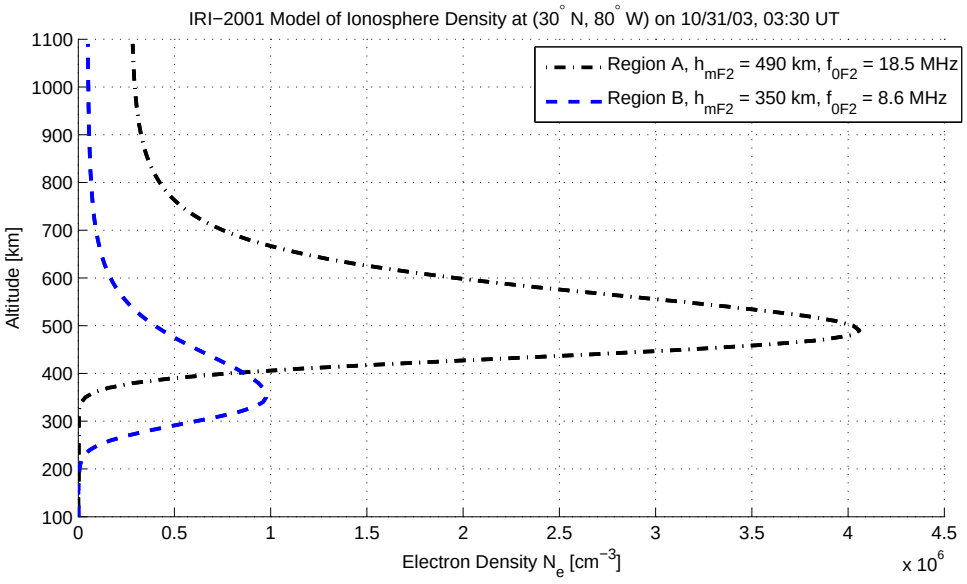

Figure 6.14: IRI models for Region A and Region B that give lowest mean squared error.

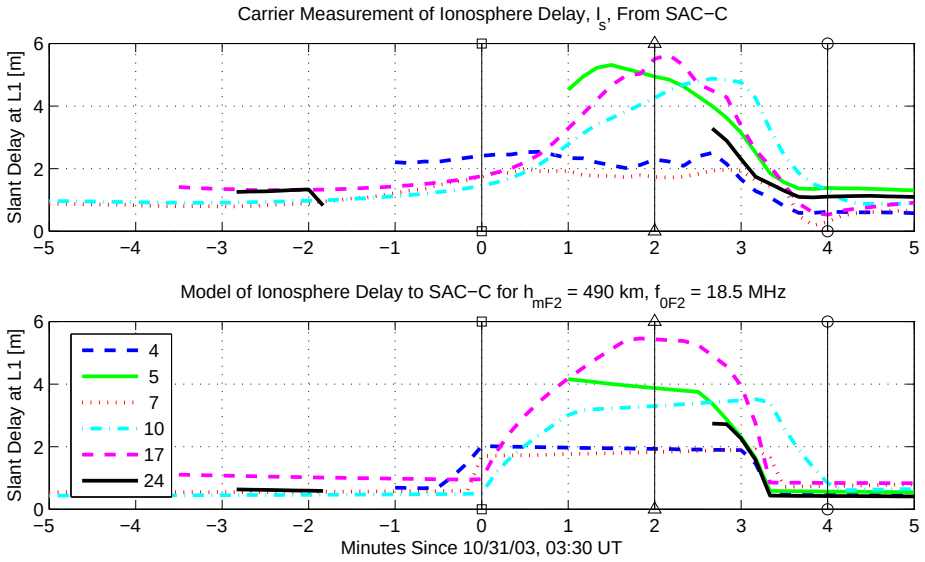

Figure 6.15: (a) SAC-C measured slant delays $\tilde{I}_s$. (b) Integrated electron content predicted by model with $h_{mF2} = 490$ km.

the feature is predicted within the correct time period. The 5 m peak measured on the LOS to PRN 17 (located to the southwest) at 03:32 UT is reproduced, as well as the drop in slant delay to background values for PRN 24. The measurement peak observed on PRN 5 is the correct amplitude but leads the measured value by a minute. The range delay to PRN 10 (south) is underpredicted by the model, although they are within about 1 m for the duration. The model overestimates the delays measured to the eastward PRNs 4 and 7 by about 0.5 m each. The smooth curvature of the data tracks is not reproduced since the model is discontinuous at the borders of the polygon shown in Figure 6.8.

6.7 Summary

This chapter investigated the spatial and temporal extent of a highly localized TEC enhancement occurring on the night of 30-31 October 2003. The enhancement is an example of the integrity threats that the WAAS Extreme Storm Detector is designed to protect users from. The Extreme Storm Detector requires that TEC be regionally well-modeled by a plane for a minimum of eight hours after an extreme storm is detected. The goal of the study is to estimate the vertical distribution of electrons as a first step in explaining the duration of the enhancement and conservatism of the eight hours of ESD hysteresis.

With a combination of CORS, IGS, WAAS, and CANAPE dual-frequency GPS network data in the southeastern US, Mexico, and the Caribbean, this localized enhancement is observed to begin as part of a larger structure coming north and west from the equatorial region at local dusk. After convecting separately from the main daytime TEC enhancement, the feature then appears to be confined to a geographic region about the size of Florida, although this may be due to a lack of sampling in Cuba. During this time it rotates with Earth, or co-rotates, over Florida and the eastern Gulf of Mexico and gradually dissipates. The TEC does not seem to recombine to background ionization levels by the time of the daily TEC rise next day.

The super-fountain effect is a possible mechanism for this amount of uplift [Tsurutani *et al.*, 2004], since ground observations indicate convection from the equatorial South Atlantic region. However, the super-fountain effect does not explain the late night co-rotation of the Florida feature.

Jason satellite data measurements of the electron content between the sea surface and 1300 km altitude constrain the altitude of the majority of the electrons of the Florida feature

to lie below 1300 km. Even though plasmaspheric processes involving hydrogen ions occur as low as 1000 km, the bound of the Jason satellite data may be evidence that oxygen is likely the dominant ion in the Florida features evolution.

Space-based GPS measurements from SAC-C that pierce the localized enhancement of 31 October 2003 exhibit a direction-dependent rise and fall of 1.5-5 m slant delay. The data from SAC-C are reasonably consistent with a model composed of two vertical density profiles that are piecewise constant horizontally. Further tuning and a more sophisticated model of this feature may yield higher accuracy, but the results of this work suggest that the TEC enhancement has an electron density profile with larger peak density and altitude compared to the surrounding nighttime region. A 500 km peak height is in agreement with both ground and space measurements. In contrast, the peak height cannot be close to the 700 km altitude of the SAC-C satellite if it is to be consistent with both the ground and the SAC-C measurements.

It is plausible that the elevated peak altitude of the feature is a factor in the TEC enhancement. Further physics-based modeling would be required to determine whether the altitude estimated is sufficiently high to explain the magnitude and duration of the TEC enhancement. An estimate of the ion composition and recombination rates at this altitude would be needed. The current value of eight hours of hysteresis in the ESD covers much of the nighttime period after a daytime storm-enhanced-density.

Even if the feature lasts longer than the 8 hours, it seems unlikely to be completely unsampled by the WAAS monitoring stations. Gaps in ionosphere pierce points do not remain for more than a few minutes at a time. The current duration of hysteresis is sufficiently conservative. More work or evidence would be needed to revise the period downward.

Chapter 7

Conclusion

7.1 Overview

The future of aviation guidance lies in the use of GPS with integrity monitoring for safety. The Federal Aviation Administration has paved the way for GPS-based navigation with its Wide Area Augmentation System and Local Area Augmentation System. These systems provide bounds on GPS error sources, in particular the ionosphere, for user safety.

The goal of this work was to identify cases of ionospheric irregularities that would pose an integrity risk to the user. Data-based modeling of electron density from total electron content measurements provided insight into the following questions.

7.2 WHO is affected by the ionosphere?

The ionosphere causes single-frequency GPS users the largest and most variable positioning error by refracting the signal as it propagates from the satellite to the user. Augmentation systems can correct for this error by providing differential corrections to the user. In addition, the augmentation system bounds the errors with high confidence to ensure user safety. If the electron density in the ionosphere varies greatly over space, then even if the augmentation system does not sample the disturbed region of the ionosphere, it must protect user safety. LAAS and WAAS achieve this through their respective ionospheric threat models.

7.3 WHAT ionosphere behavior has been observed?

From ground-based observations of some of the most severe storms of Solar Cycle 23, a few types of integrity threats were illustrated in Chapter 3. Users of Ground-Based Augmentation Systems such as LAAS must be protected from steep spatial gradients in total electron content that could fall beyond the view of the LAAS reference receiver by an ionospheric threat model. For Space-Based Augmentation Systems such as WAAS, irregularities in the ionosphere that fall between the measurements of the widely spaced reference GPS receivers can trick the SBAS into finding the ionosphere to be smooth when it is not. WAAS protects against this condition with its Extreme Storm Detector and ionosphere undersampling threat model.

7.4 WHEN can integrity threats occur?

In Chapter 4, the WAAS Irregularity Detector's measure of ionospheric disturbance, χ_r^2, was shown to have moderate correlation (-0.55) with the log of the hourly D_{st} index of storm-time geomagnetic activity. The rise of χ_r^2 over the Storm Detector's threshold was linked to loss of LPV navigation service availability. A regional disturbance reduces LPV availability locally, which then reduces coverage: the percent of the country receiving LPV service for some minimum amount (e.g., 95%) of time. Using records of LPV 95% availability, and computing χ^2 for the days when coverage values were unavailable, it was shown that during half of a solar cycle (1856 days), there were 59 stormy days. Nine of these 59 days were extreme storms, spread over five stormy periods. A D_{st} threshold that would detect all storms would have a 30% false alarm rate. However, to detect all the extreme storms, a D_{st} threshold around -285 nT would only give false alarms 0.16% of the time. The extremely negative values of D_{st} tend to produce the most extreme ionospheric irregularities. Solar Cycle 23 had a disproportionate share of the most extreme D_{st} days, compared with the post-solar-max years of the previous four solar cycles. The storms of Solar Cycle 23 are expected to represent near-worst-case irregularities.

7.5 HOW much can ionosphere error vary between a LAAS reference station and a user?

In Chapter 5, one of the extreme storms of the cycle was analyzed to identify severe spatial rates of change in TEC in development of the LAAS ionosphere threat model. The LAAS reference station tracking a GPS satellite suffers an ionospheric delay that will differ slightly from that of a user a few kilometers away tracking the same satellite. Studies prior to and after this work have shown that during nominal or even moderately disturbed times this delay difference will be fewer than 10 mm of difference in delay per kilometer of receiver separation.

From the evidence of static receivers separated by 250 km or more, this work provided the first evidence that during stormy periods the spatial gradients in delay could be as much as 300 mm/km. To deduce this magnitude gradient, it was observed that an identifiable plasma structure in the ionosphere was moving with speeds comparable to the IPP speed. The gradient is two orders of magnitude higher than nominal and has since instigated the development of the LAAS ionospheric threat model that includes both large gradients and a range of velocities relative to the IPP. The subsequent studies have confirmed events as high as 425 mm/km, and have shown that the impact on a user, if unmitigated, could yield tens of meters of position error. The mitigation techniques, nearly finalized, depend on making unavailable the satellite geometries that, combined with anomalous ionosphere, could yield such unacceptably high position errors.

7.6 WHERE are the electrons in a TEC enhancement that could be unsampled by WAAS reference stations?

The innovation in Chapter 6 was in using both ground- and space-based data to analyze the electron variation in a nearly stationary localized TEC enhancement observed during the nighttime period of another extreme storm in the solar cycle. The fundamental challenge of tomographic reconstruction of the ionosphere from ground measurements is the lack of diversity in lines of sight. For this reason, a simple three-dimensional static model of the ionosphere was developed to avoid conditioning problems in inversion. Also, space-based GPS data provide a significant advantage. In this case, TEC measurements from the SAC-C satellite were compared to the prediction for variable model parameters. The altitude of

the peak electron density was resolved to be 500 km with a horizontal extent of about 700 km in latitude and longitude.

The recombination rate and duration of the enhancement may have implications for the period of hysteresis built into the WAAS Extreme Storm Detector. Currently set at eight hours, the hysteresis is sufficiently conservative because features that last even longer than the case study are not likely to remain unsampled for eight hours.

7.7 Looking Ahead

Issues for the GPS aviation community involving the ionosphere were shown in this work. They can provide useful directions for space weather research. Evidence from other storms suggests that the case study of localized high-amplitude disturbances is not an isolated incident or statistical fluke. TEC maps in Appendix B of GPS dual-frequency data early on UT dates 30 October 2003, 7 April 2000, and 16 July 2000 indicate that the feature may occur on other active dates during local evening in the southeastern US. Moreover, the evidence of [Dehel, 2005] suggests that such a feature may occur on less severely disturbed nights. However, the exact time, location, and evolution of each of these cases varies. The consistency of geographic location suggests that the feature may be causally linked to the South Atlantic Anomaly. Future work in both data analysis and modeling will help further illuminate this phenomenon.

Modeling of the mid-latitude E and B fields in a manner similar to Hanson and Moffett [Hanson and Moffett, 1966] would provide insight into the TEC uplift and drift if the super-fountain effect is the driving process. Given the ion and neutral densities at only a slightly higher altitude than usual, the electron peak density of the localized enhancement should recombine within a few hours' time. The insights of atmospheric science could feed back into the aviation community again by allowing the ESD hysteresis period to be reduced downward. A reduction in the duration of hysteresis or geographic coverage of the WAAS Extreme Storm Detector would improve precision approach service availability to WAAS users.

Another example of the connection between GPS as both a navigation tool and a remote sensing tool includes concerns about scintillation. With the advent of a second civil frequency in a protected band and the launch of Galileo (Europe), Beidou (China), and QZSS (Japan), the primary performance measure of Augmentation Systems affected by a

disturbed ionosphere will shift from integrity to continuity. Loss of one frequency would cause a reversion to the current, single-frequency operational mode. Navigation service is anticipated to be better and better with refinements to algorithms and extension of service to many other parts of the world. The anticipated advances in navigation and atmospheric science will owe a great deal of their success to Global Navigation Satellite Systems such as GPS.

Appendix A

Acronyms

ACE	Advanced Composition Explorer
AFB	Air Force Base
CANAPE	Caribbean-North American Plate Experiment
CHAMP	Challenging Minisatellite Payload satellite
CME	Coronal Mass Ejection
CONAE	National Commission on Space Activities, Argentina
CONUS	Conterminous United States
CORS	Continuously Operating Reference Stations
CST	Central Standard Time
ENU	East-North-Up
ESD	Extreme Storm Detector
EST	Eastern Standard Time
FAA	Federal Aviation Administration
GBAS	Ground Based Augmentation System
GEO	GEOstationary satellite
GIM	Global Ionospheric Mapping software
GIVE	Grid Ionosphere Vertical Error
GNSS	Global Navigation Satellite System
GOES	Geostationary Operational Environmental Satellite
GPS	Global Positioning System
HAL	Horizontal Alert Limit

ICAO	International Civil Aviation Organization
IGD	Ionosphere Grid Delays
IGP	Ionosphere Grid Point
IGS	International GNSS Service
IMF	interplanetary magnetic field
INPE	National Institute for Space Research, Brazil
JPL	Jet Propulsion Laboratory
LAAS	Local Area Augmentation System
LGF	LAAS Ground Facility
LNAV	Lateral Navigation
LPV	Lateral Precision with Vertical guidance
LOS	line of sight
MSE	mean squared error
NASA	National Aeronautics and Space Administration
NGDC	National Geophysical Data Center
NOAA	National Oceanic and Atmospheric Administration
PAN	WAAS Performance Analysis Report
PRN	pseudo random number
RF	radio frequency
RINEX	receiver-independent exchange GPS data format
SAC-C	Satellite for Scientific Applications - C, Argentina
SARPs	Standards And Recommended Practices
SBAS	Satellite Based Augmentation System
SI	System International units
SOHO	Solar and Heliospheric Observatory
SPIDR	Space Physics Interactive Data Resource
SVN	satellite vehicle number
TEC	Total Electron Content
TEC	Total Electron Content units
UT	Universal Time
UV	ultraviolet

VAL	Vertical Alert Limit
VDB	VHF Data Broadcast
VNAV	Vertical Navigation
WAAS	Wide Area Augmentation System
WRS	WAAS Reference Station
WMS	WAAS Master Station
ZBW	WRS at Boston, Massachusetts
ZDC	WRS at Washington, D. C.

Appendix B

Maps of Vertical TEC during Storms 2000–2005

Dual frequency GPS data were used to map the ionosphere over CONUS at two-hour intervals for the days during Solar Cycle 23 that had $D_{st} \leq -250nT$. These dates are shown in Table B.1. The data sets used are indicated as: 1) WAAS; 2) CORS; 3) IGS; and 4) CANAPE. The processing for these data is detailed in Section 2.3.1. For the periods during which only WAAS data are used (Set 1), IPPs have been drawn on the maps as circles, with line segments pointing toward the receiver making the measurement. This processing is described in Section 2.3.2. The color ranges from 0 m (blue) to 10 m (red) of equivalent vertical delay at L1. For all of the maps, an ionosphere shell height of $h_{iono} = 350$ km has been used. In the case of 30–31 October 2003, the estimate of the peak height was shown in Chapter 6 to be closer to 500 km. The shell height used by the WAAS real-time ionosphere model algorithm was chosen for comparing the storm days.

Table B.1: Days of maps included in Appendix B.

Fig.	Year	Mon (mm)	Day (dd)	Data Used	D_{st} (nT)	Cvg. %
B.1	2000	04	06	1,2,3	-287	low
B.2	2000	04	07	1,2,3	-288	low
B.3	2000	07	15	1,2,3	-289	low
B.4	2000	07	16	1,2,3	-301	low
B.5	2001	03	31	1	-387	low
B.6	2001	04	11	1	-271	low
B.7	2001	11	06	1	-292	84
B.8	2003	10	29	1,2,3,4	-345	0
B.9	2003	10	30	1,2,3,4	-401	0
B.10	2003	10	31	1,2,3,4	-320	0
B.11	2003	11	20	1,2,3	-472	0
B.12	2003	11	21	1	-320	55
B.13	2004	11	08	1	-373	0
B.14	2004	11	10	1	-289	90

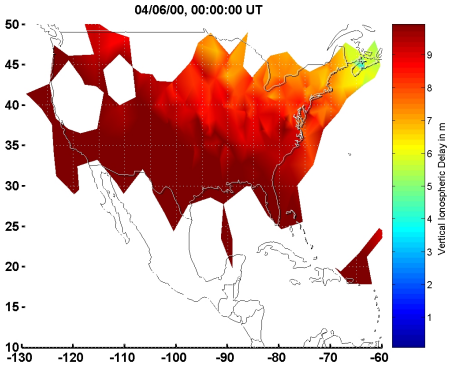

(a) 00:00 UT

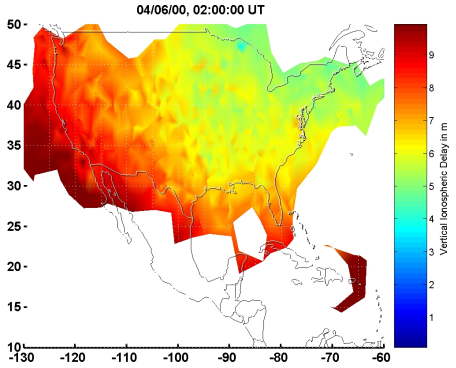

(b) 02:00 UT

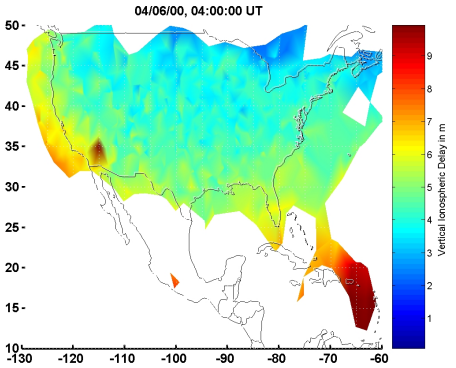

(c) 04:00 UT

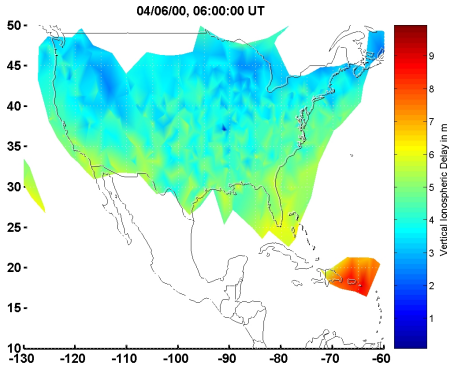

(d) 06:00 UT

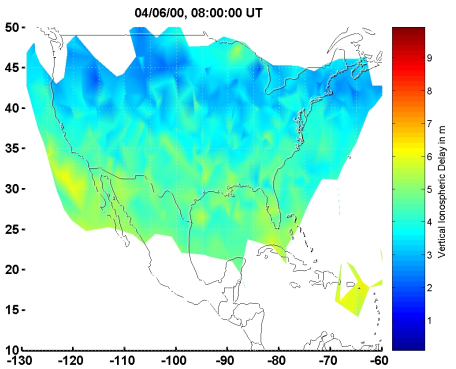

(e) 08:00 UT

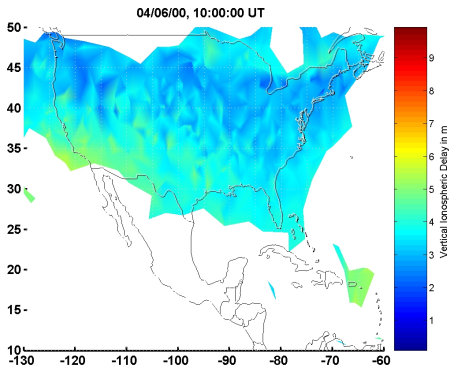

(f) 10:00 UT

Figure B.1: 6 April 2000, 00:00–10:00 UT.

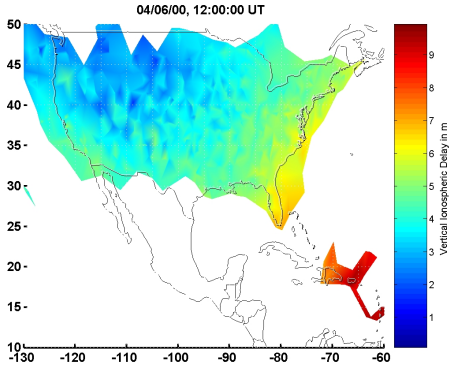

(g) 12:00 UT

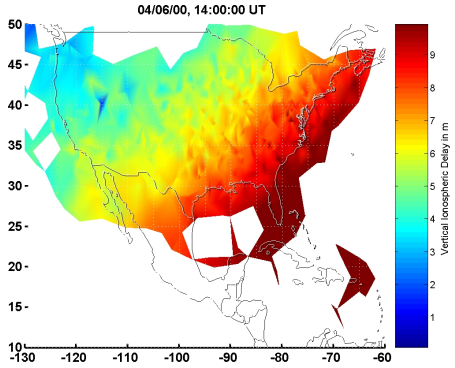

(h) 14:00 UT

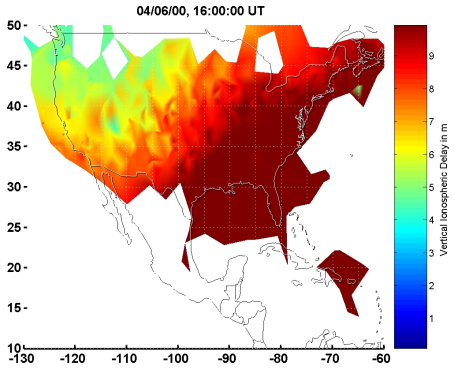

(i) 16:00 UT

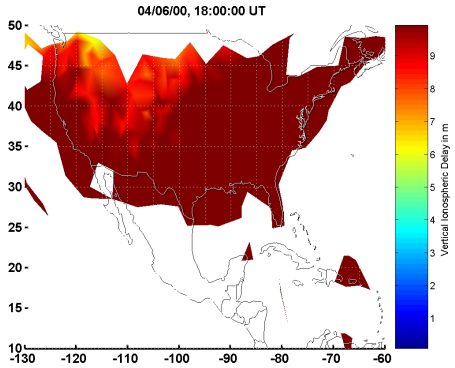

(j) 18:00 UT

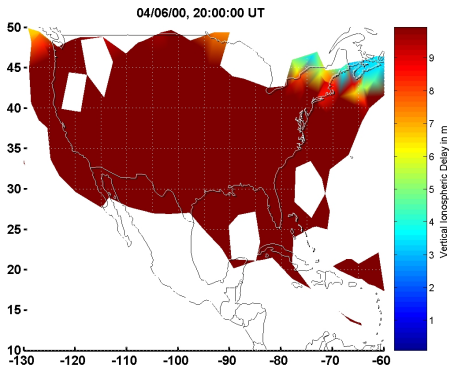

(k) 20:00 UT

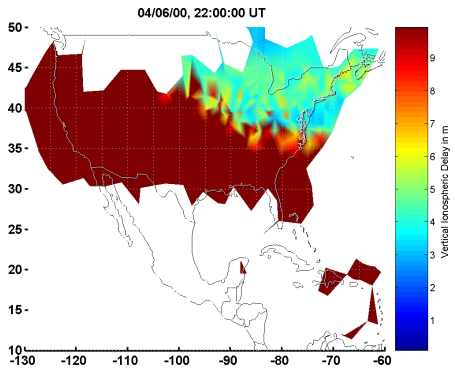

(l) 22:00 UT

Figure B.1: 6 April 2000, 12:00–22:00 UT.

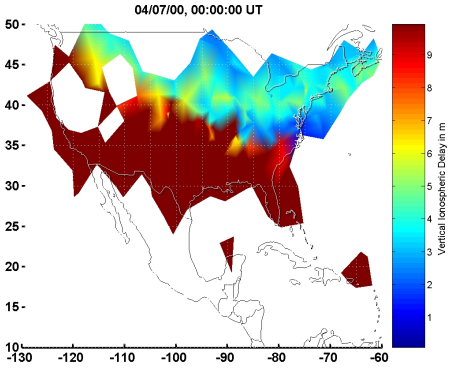

(a) 00:00 UT

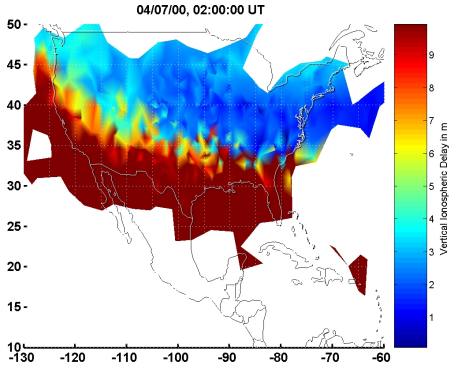

(b) 02:00 UT

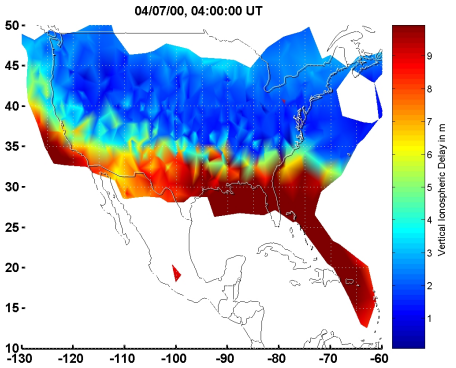

(c) 04:00 UT

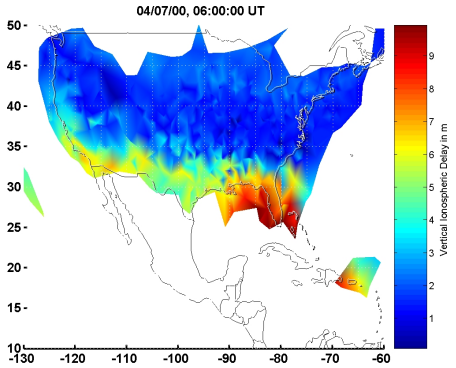

(d) 06:00 UT

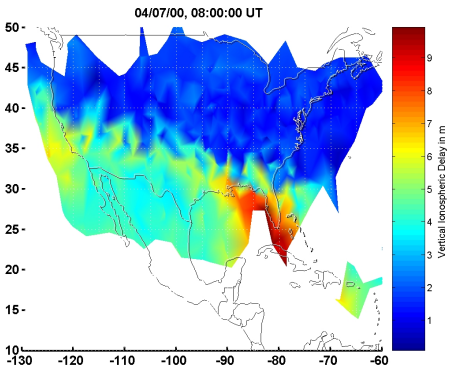

(e) 08:00 UT

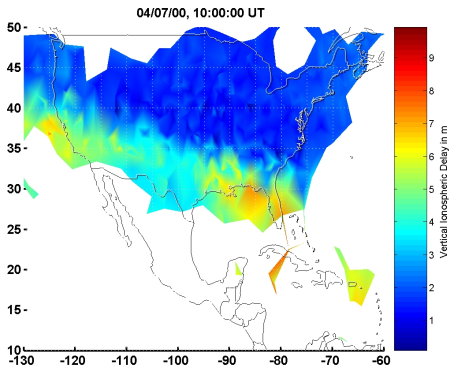

(f) 10:00 UT

Figure B.2: 7 April 2000, 00:00–10:00 UT.

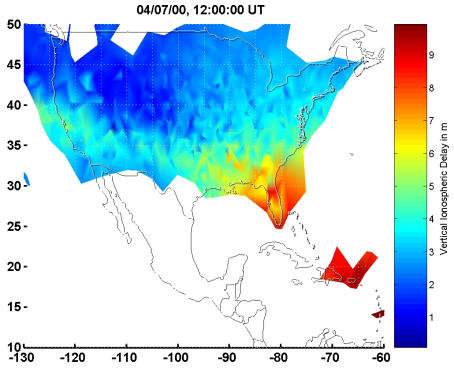

(g) 12:00 UT

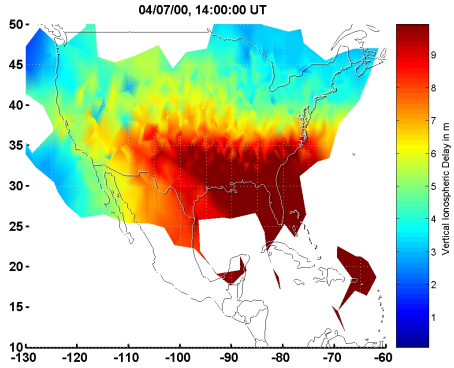

(h) 14:00 UT

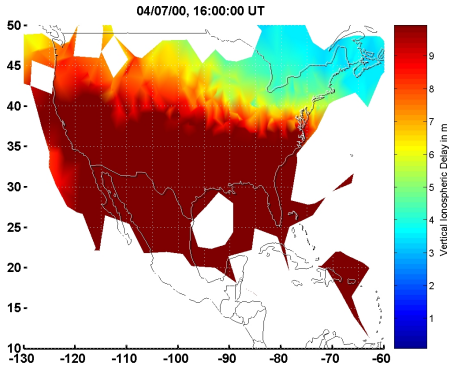

(i) 16:00 UT

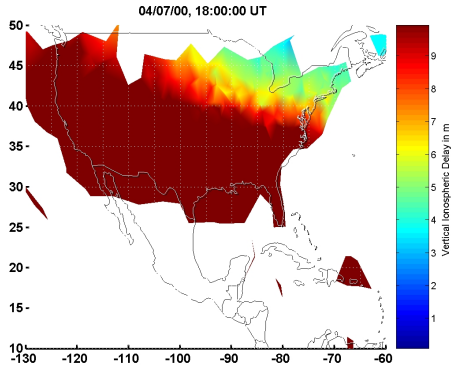

(j) 18:00 UT

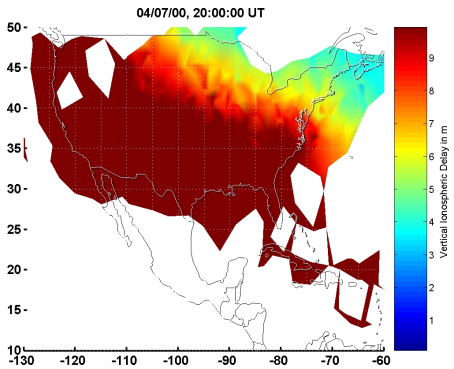

(k) 20:00 UT

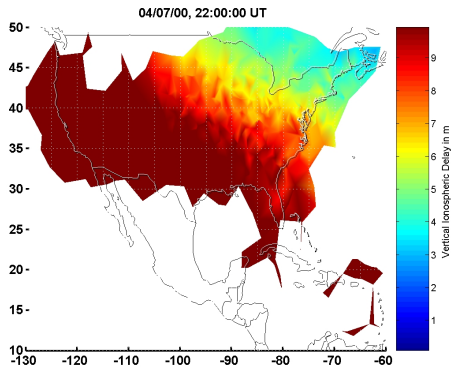

(l) 22:00 UT

Figure B.2: 7 April 2000, 12:00–22:00 UT.

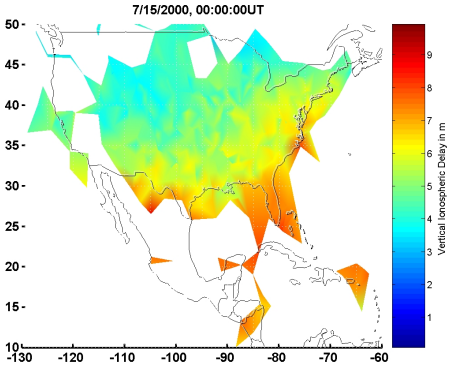

(a) 00:00 UT

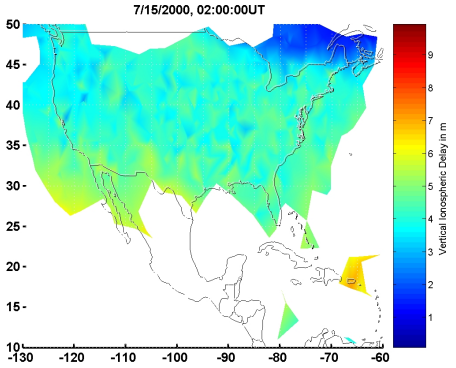

(b) 02:00 UT

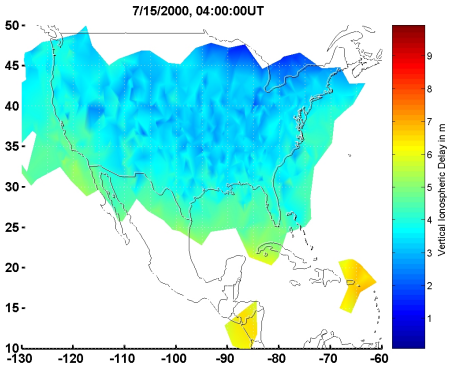

(c) 04:00 UT

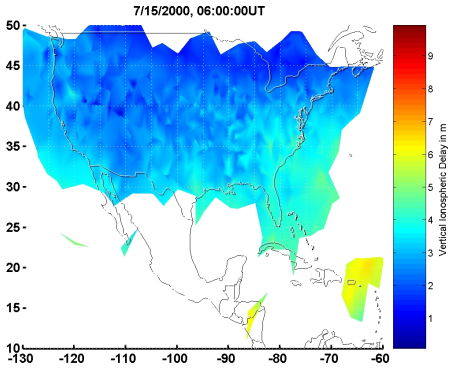

(d) 06:00 UT

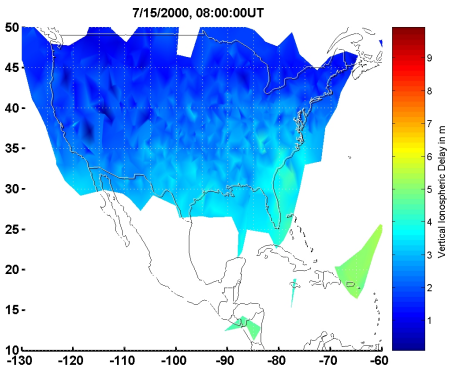

(e) 08:00 UT

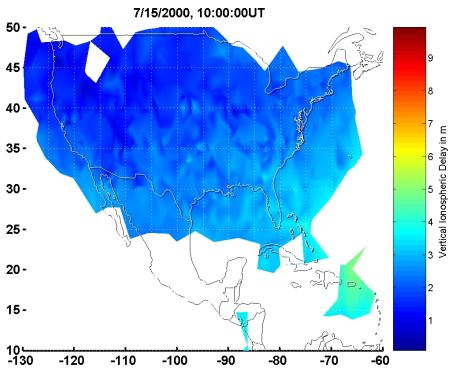

(f) 10:00 UT

Figure B.3: 15 July 2000, 00:00–10:00 UT.

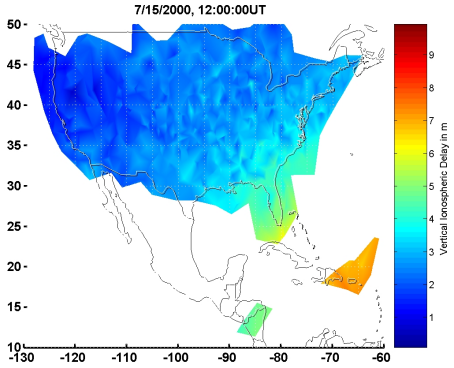

(g) 12:00 UT

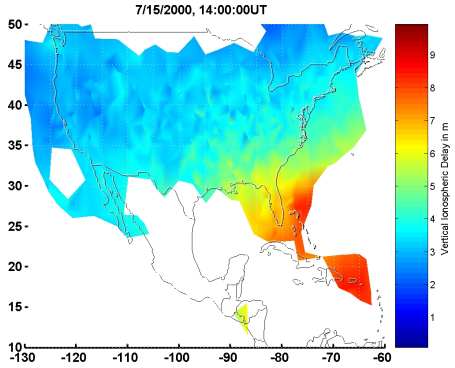

(h) 14:00 UT

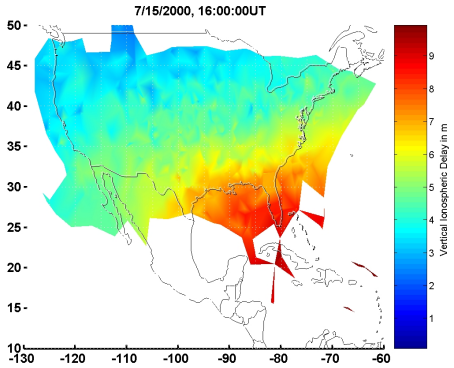

(i) 16:00 UT

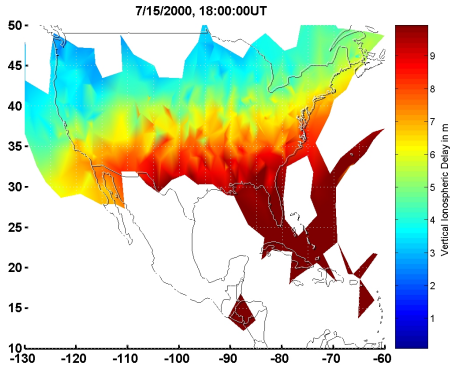

(j) 18:00 UT

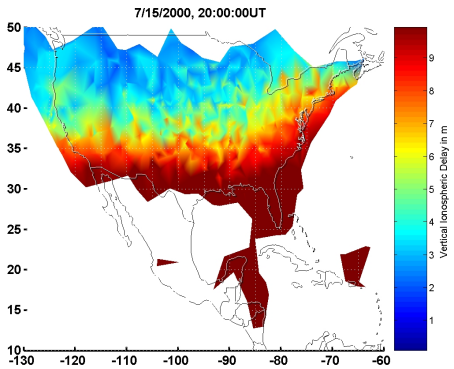

(k) 20:00 UT

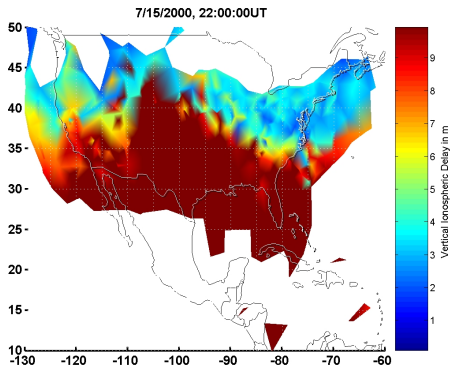

(l) 22:00 UT

Figure B.3: 15 July 2000, 12:00–22:00 UT.

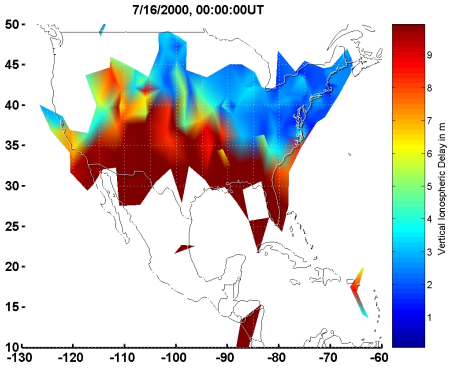

(a) 00:00 UT

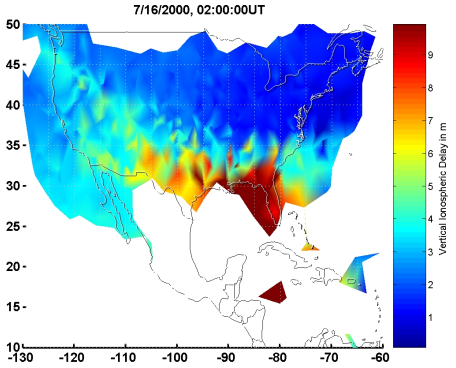

(b) 02:00 UT

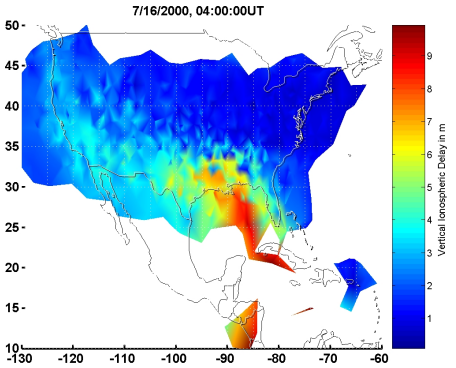

(c) 04:00 UT

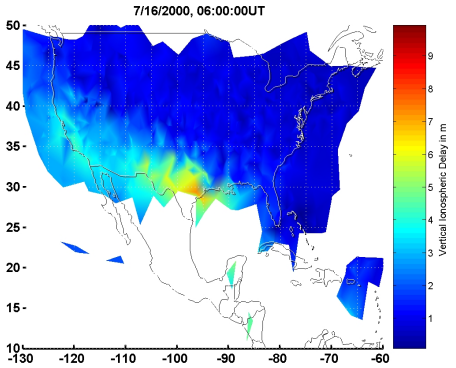

(d) 06:00 UT

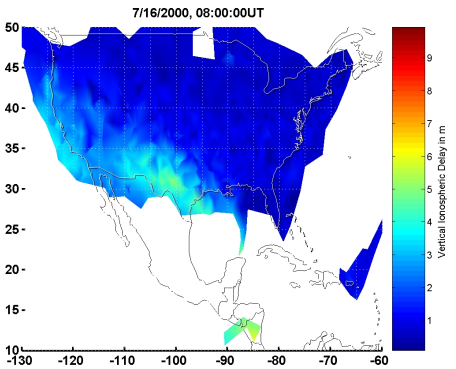

(e) 08:00 UT

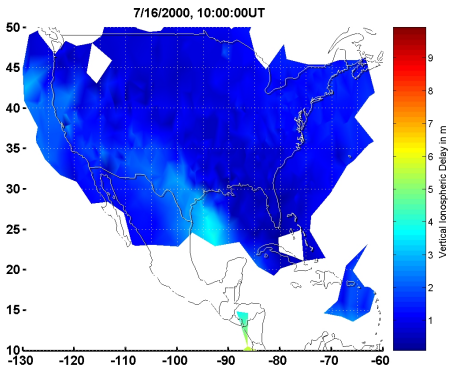

(f) 10:00 UT

Figure B.4: 16 July 2000, 00:00–10:00 UT.

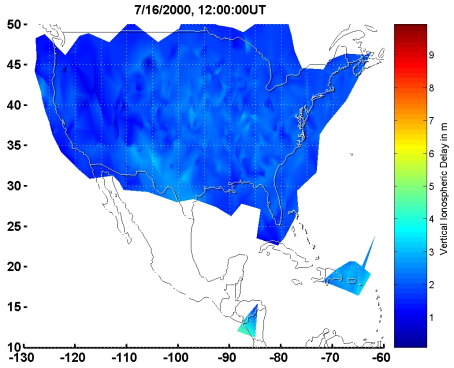

(g) 12:00 UT

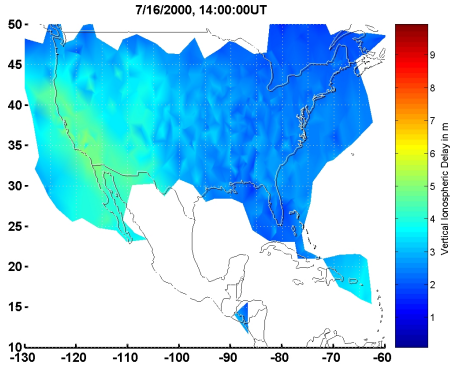

(h) 14:00 UT

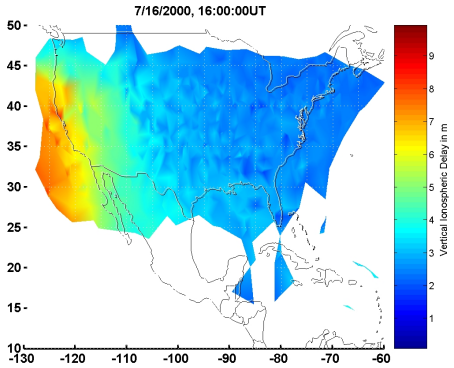

(i) 16:00 UT

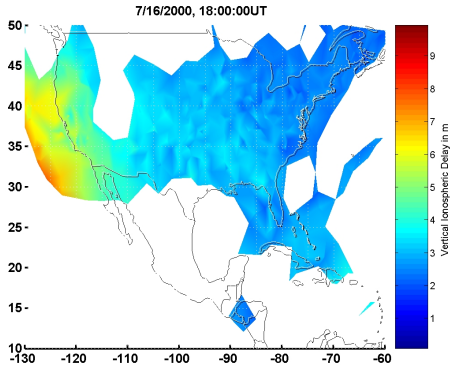

(j) 18:00 UT

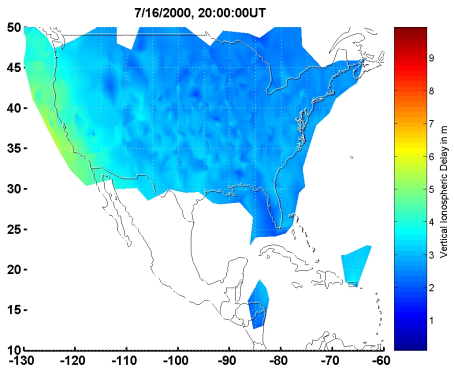

(k) 20:00 UT

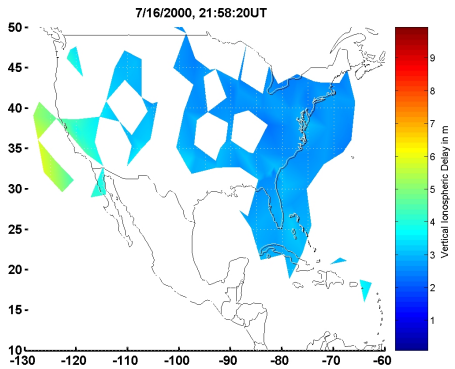

(l) 22:00 UT

Figure B.4: 16 July 2000, 12:00–22:00 UT.

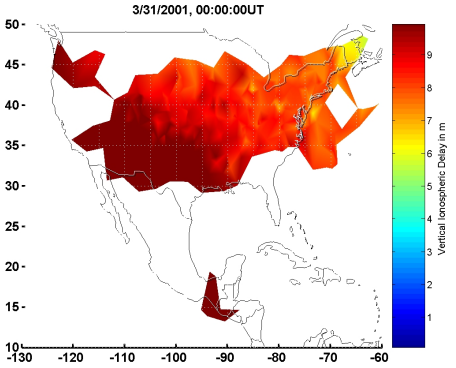

(a) 00:00 UT

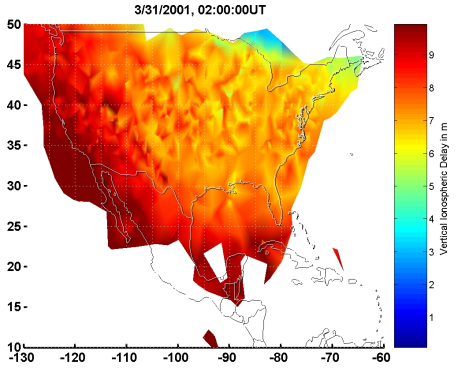

(b) 02:00 UT

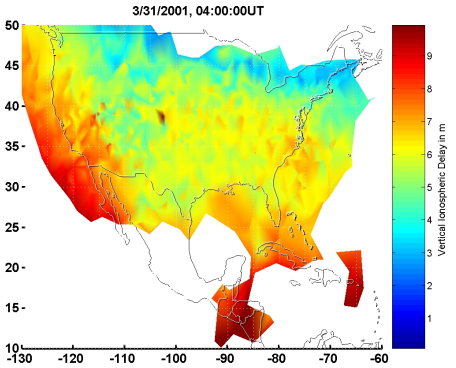

(c) 04:00 UT

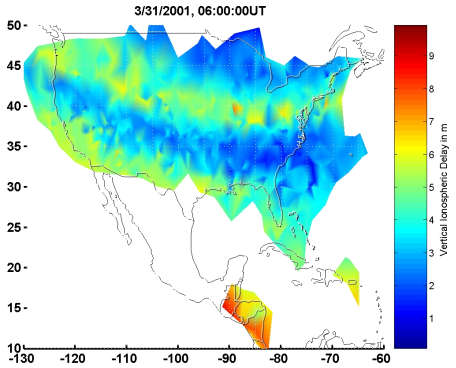

(d) 06:00 UT

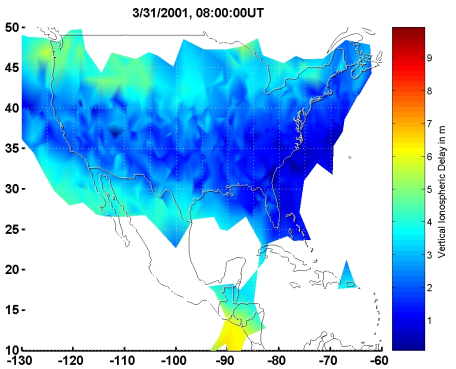

(e) 08:00 UT

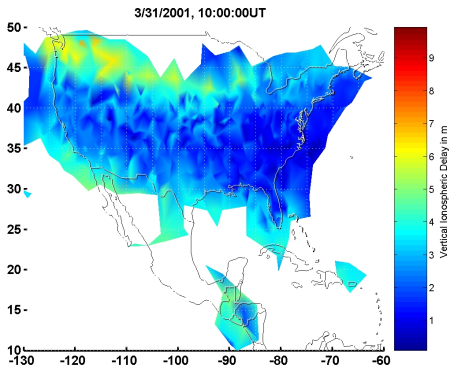

(f) 10:00 UT

Figure B.5: 31 March 2001, 00:00–10:00 UT.

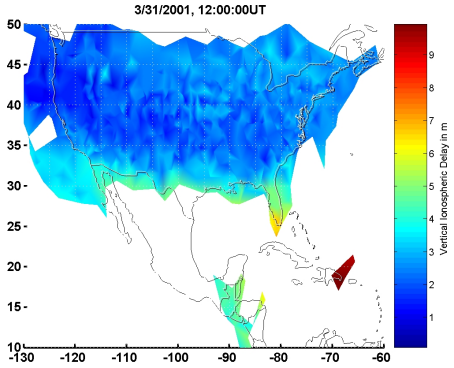

(g) 12:00 UT

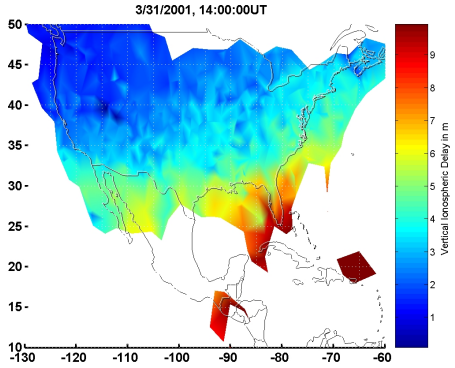

(h) 14:00 UT

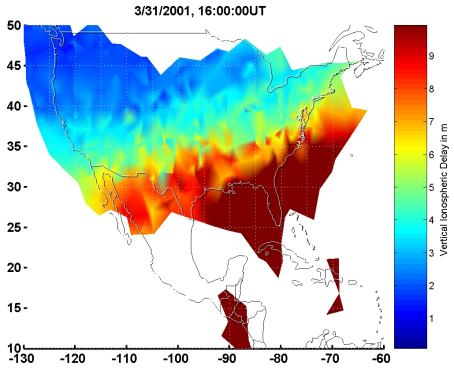

(i) 16:00 UT

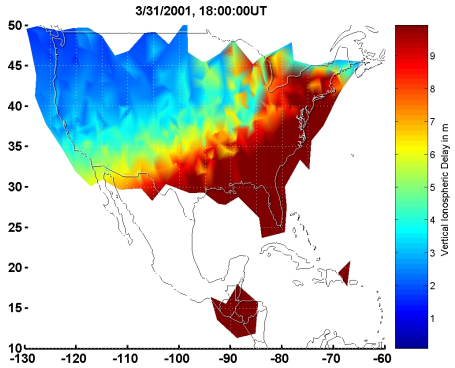

(j) 18:00 UT

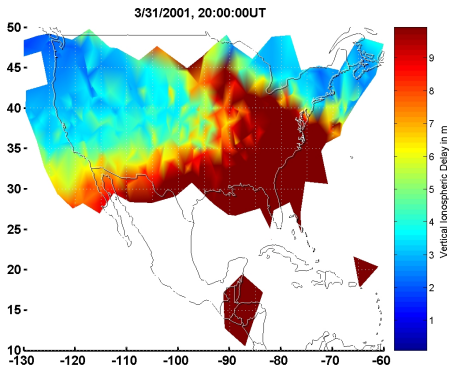

(k) 20:00 UT

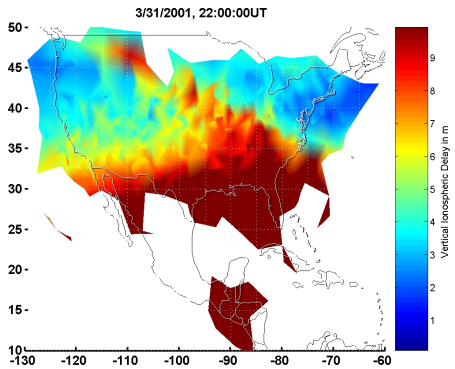

(l) 22:00 UT

Figure B.5: 31 March 2001, 12:00–22:00 UT.

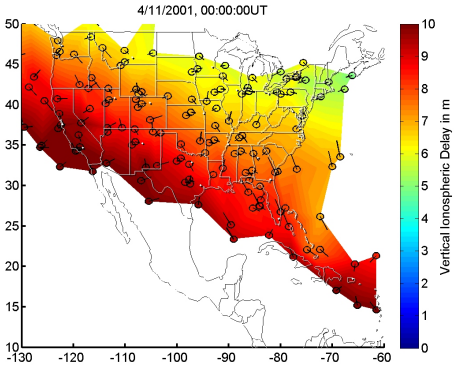

(a) 00:00 UT

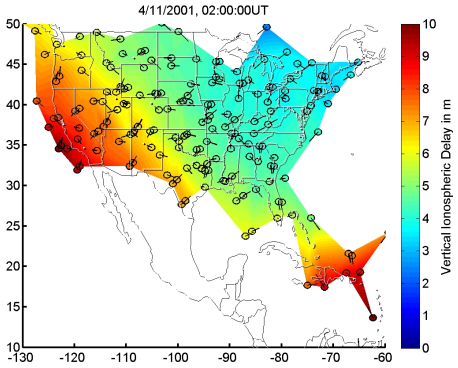

(b) 02:00 UT

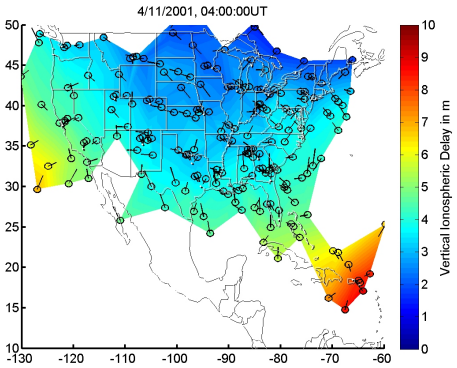

(c) 04:00 UT

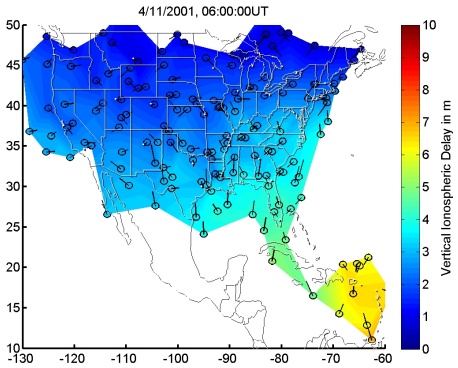

(d) 06:00 UT

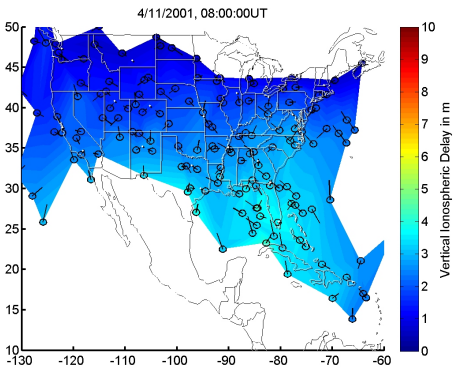

(e) 08:00 UT

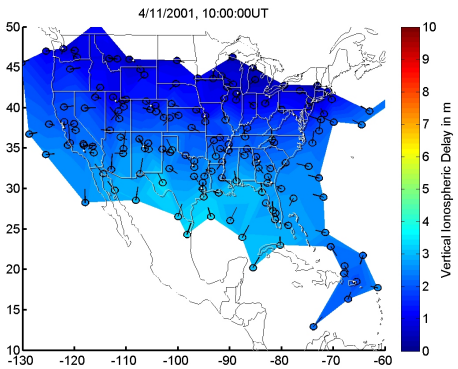

(f) 10:00 UT

Figure B.6: 11 April 2001, 00:00–10:00 UT.

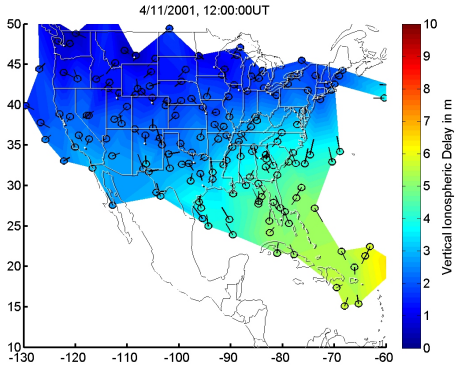

(g) 12:00 UT

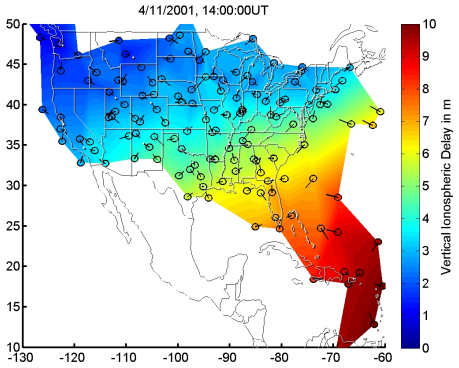

(h) 14:00 UT

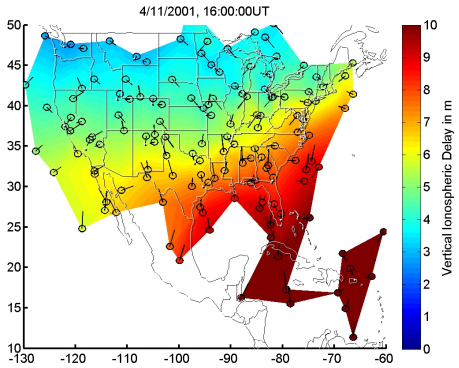

(i) 16:00 UT

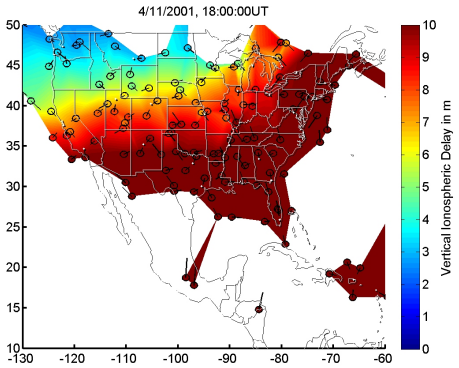

(j) 18:00 UT

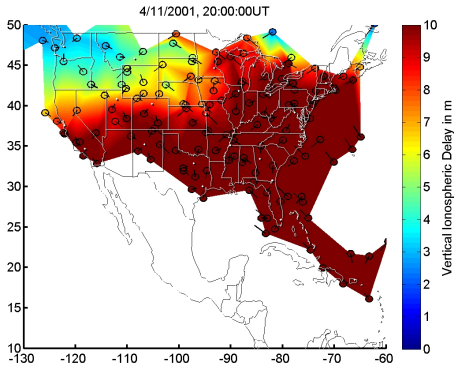

(k) 20:00 UT

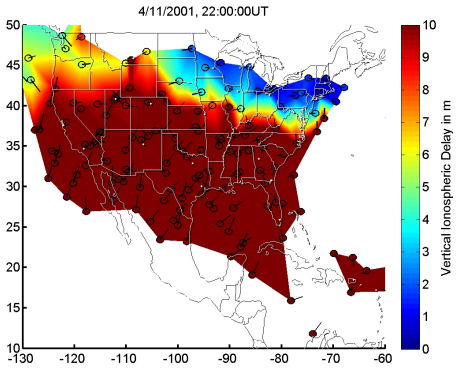

(l) 22:00 UT

Figure B.6: 11 April 2001, 12:00–22:00 UT.

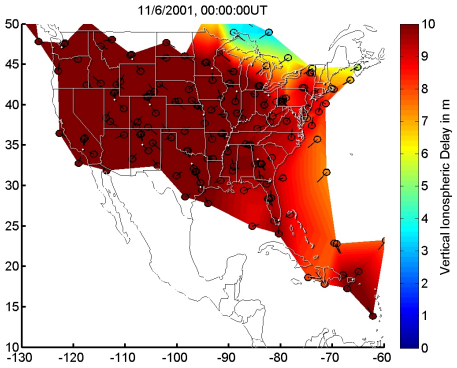

(a) 00:00 UT

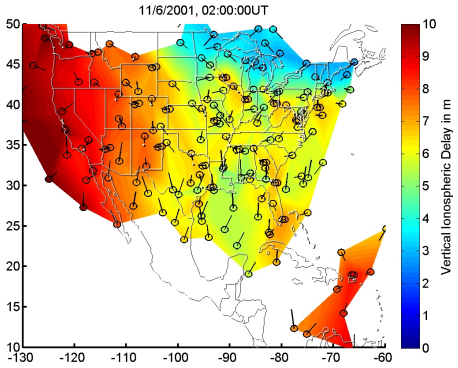

(b) 02:00 UT

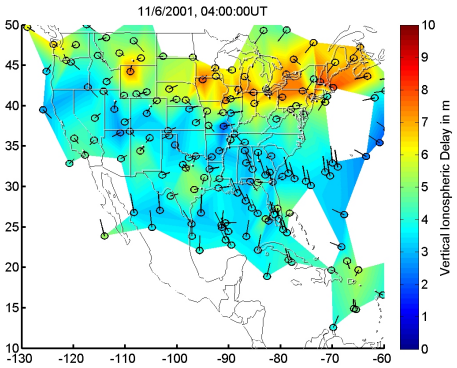

(c) 04:00 UT

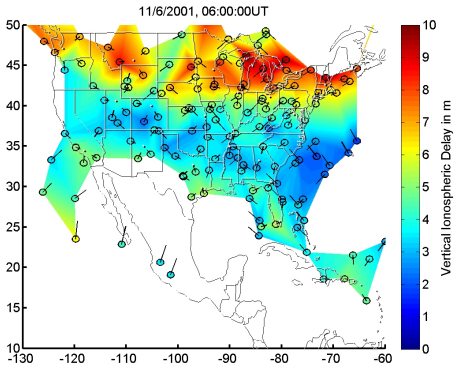

(d) 06:00 UT

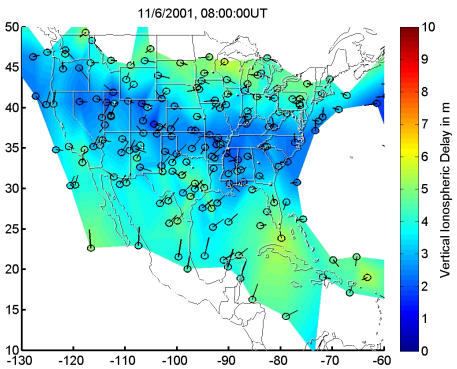

(e) 08:00 UT

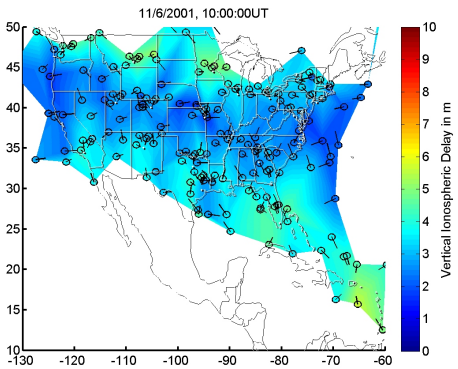

(f) 10:00 UT

Figure B.7: 6 November 2001, 00:00–10:00 UT.

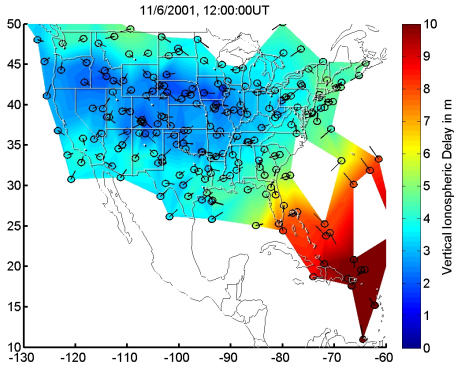

(g) 12:00 UT

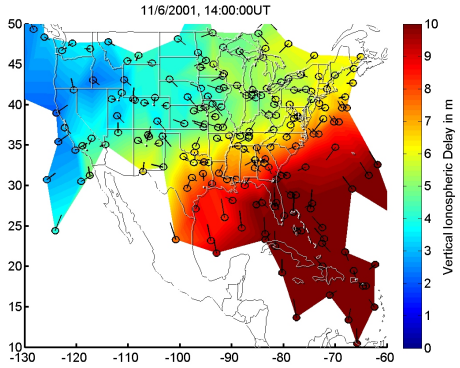

(h) 14:00 UT

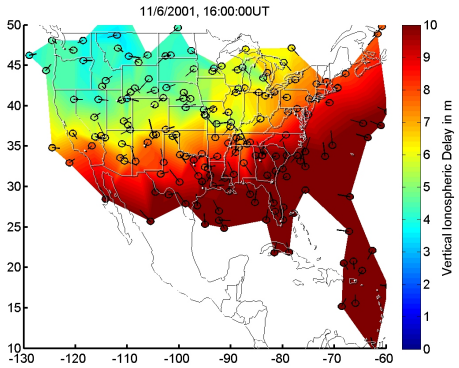

(i) 16:00 UT

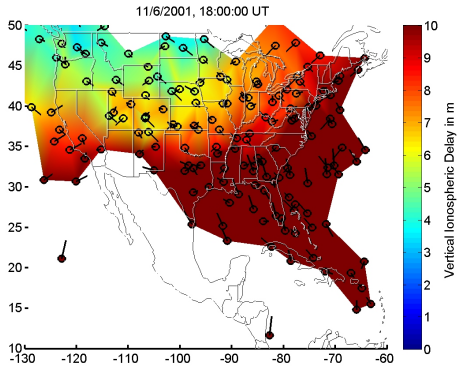

(j) 18:00 UT

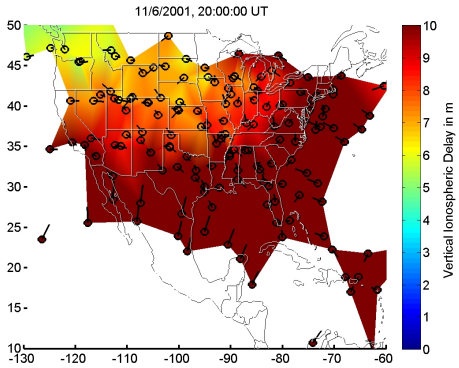

(k) 20:00 UT

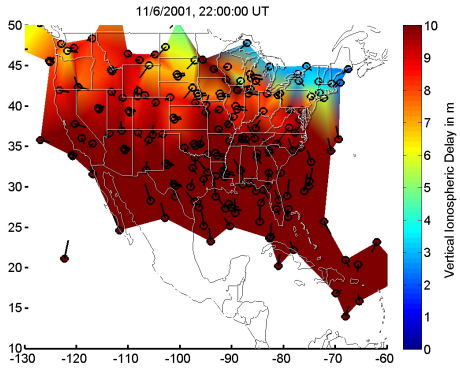

(l) 22:00 UT

Figure B.7: 6 November 2001, 12:00–22:00 UT.

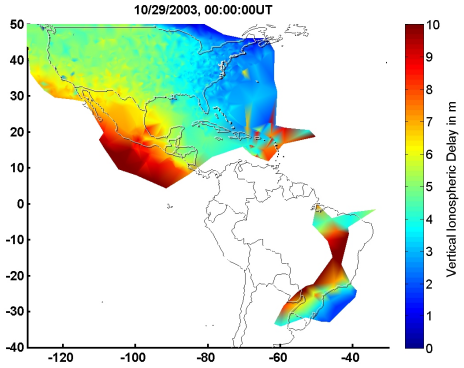

(a) 00:00 UT

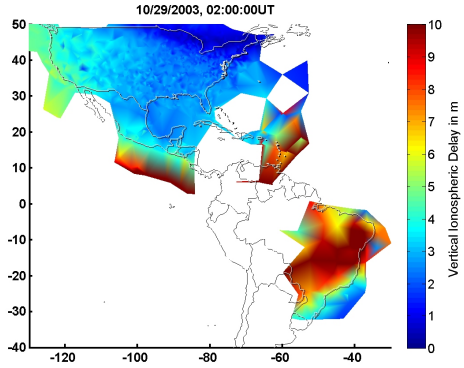

(b) 02:00 UT

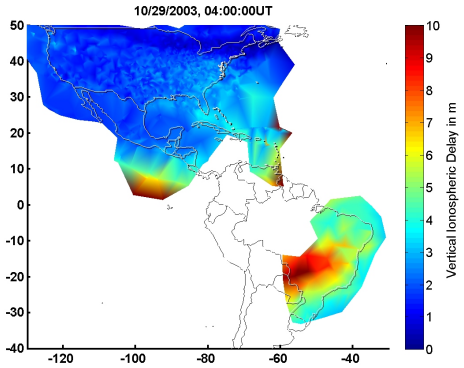

(c) 04:00 UT

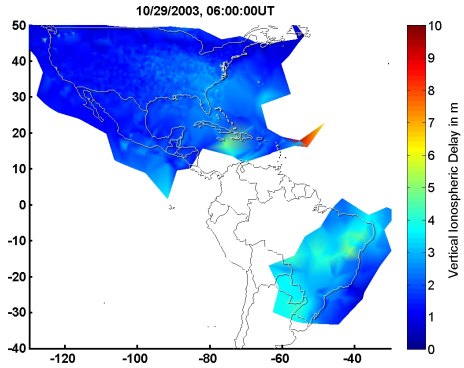

(d) 06:00 UT

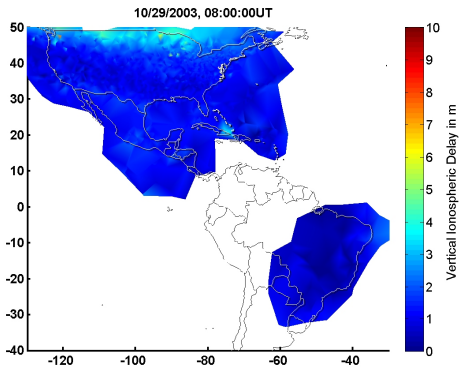

(e) 08:00 UT

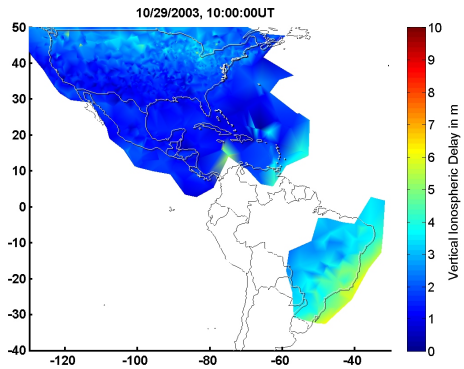

(f) 10:00 UT

Figure B.8: 29 October 2003, 00:00–10:00 UT.

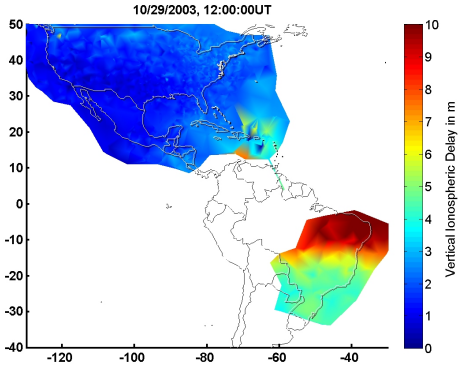

(g) 12:00 UT

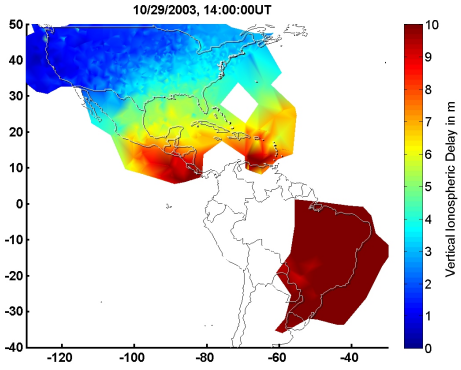

(h) 14:00 UT

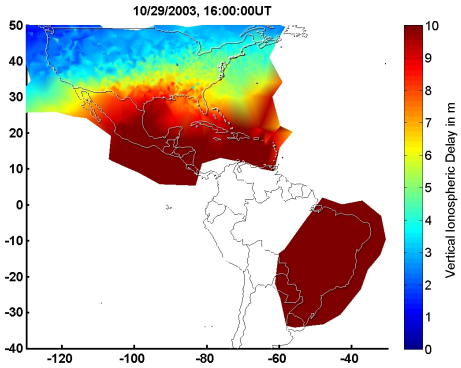

(i) 16:00 UT

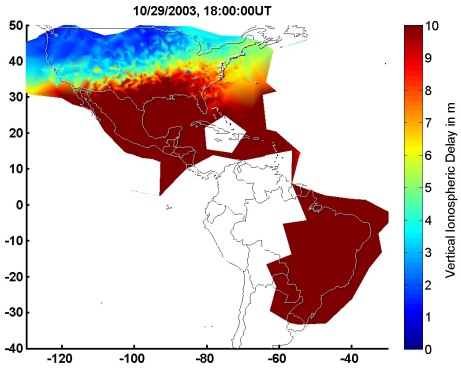

(j) 18:00 UT

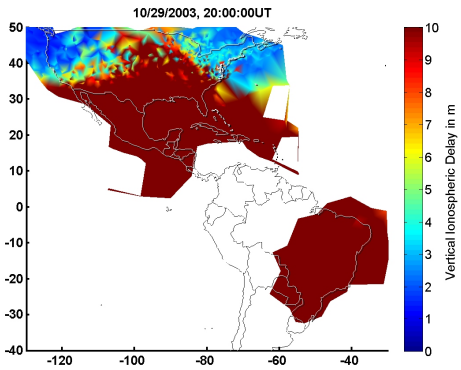

(k) 20:00 UT

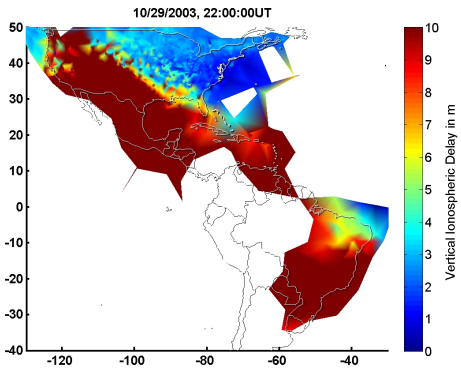

(l) 22:00 UT

Figure B.8: 29 October 2003, 12:00–22:00 UT.

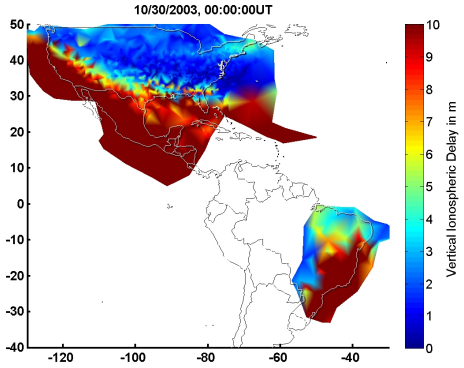

(a) 00:00 UT

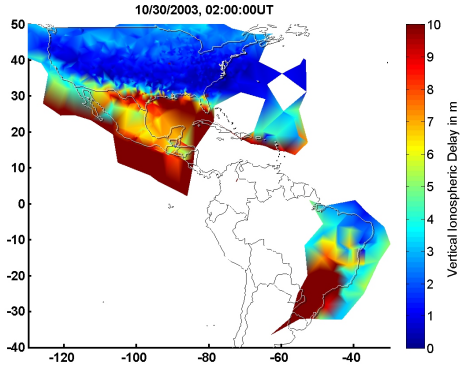

(b) 02:00 UT

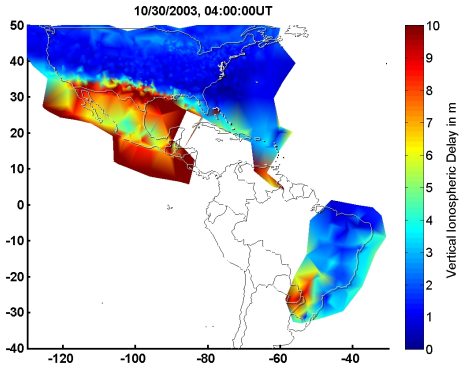

(c) 04:00 UT

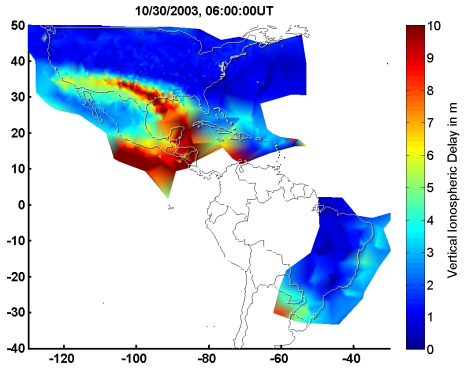

(d) 06:00 UT

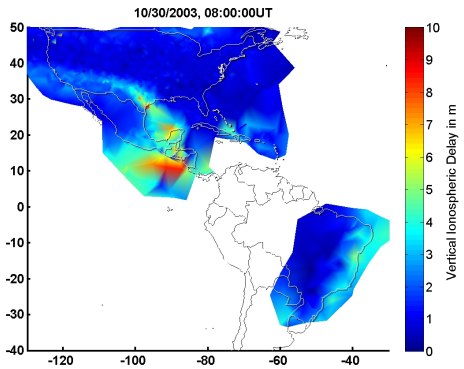

(e) 08:00 UT

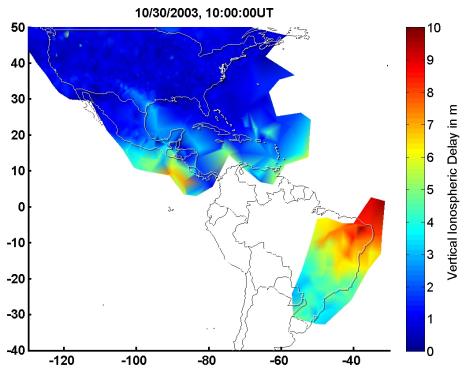

(f) 10:00 UT

Figure B.9: 30 October 2003, 00:00–10:00 UT.

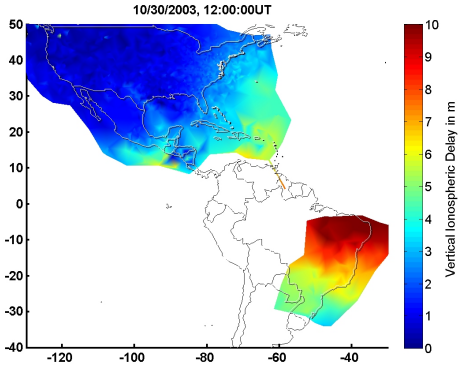

(g) 12:00 UT

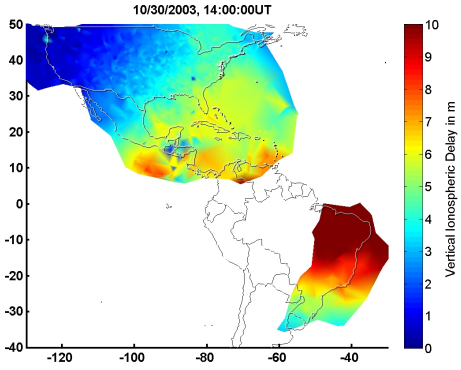

(h) 14:00 UT

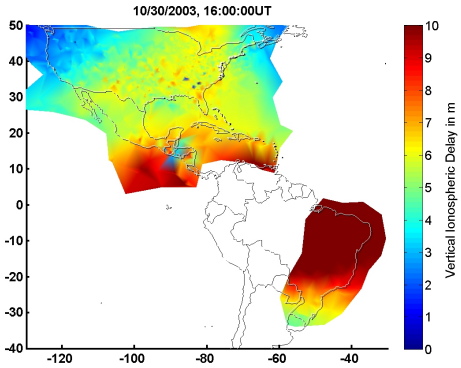

(i) 16:00 UT

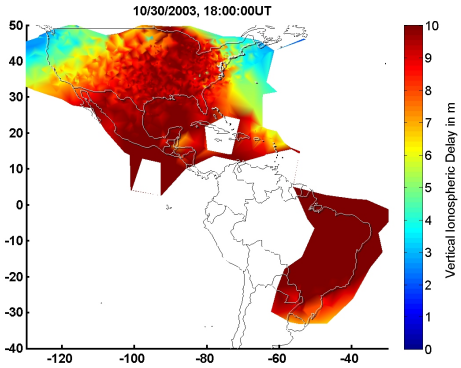

(j) 18:00 UT

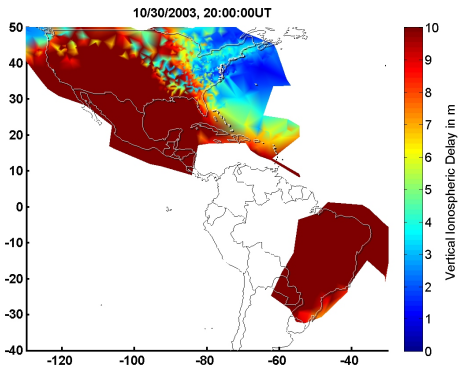

(k) 20:00 UT

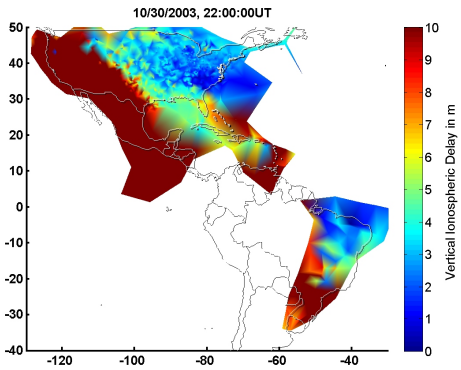

(l) 22:00 UT

Figure B.9: 30 October 2003, 12:00–22:00 UT.

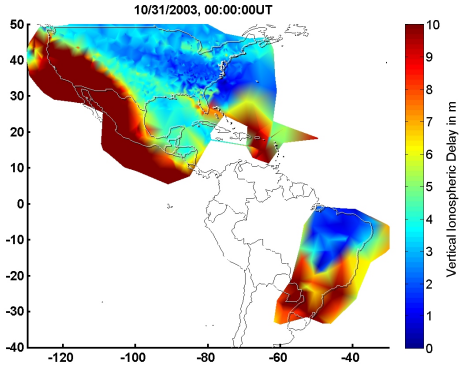

(a) 00:00 UT

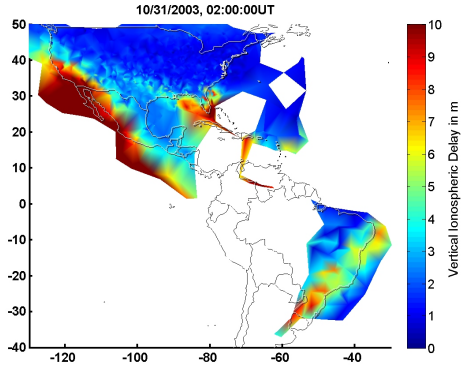

(b) 02:00 UT

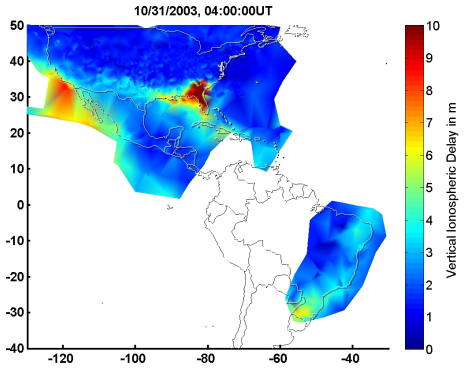

(c) 04:00 UT

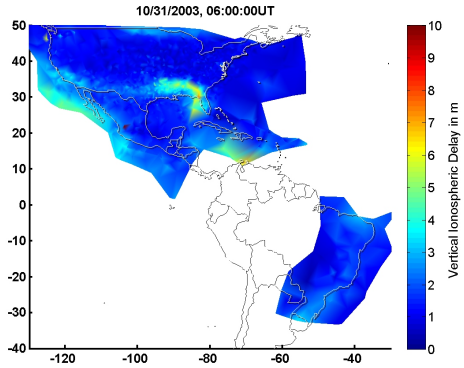

(d) 06:00 UT

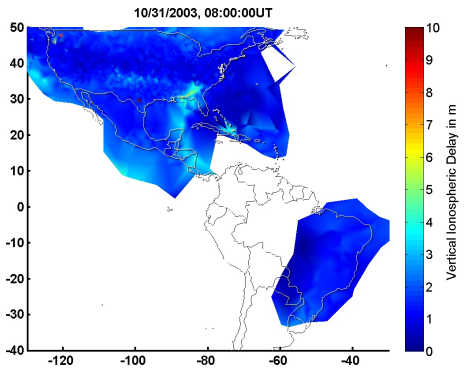

(e) 08:00 UT

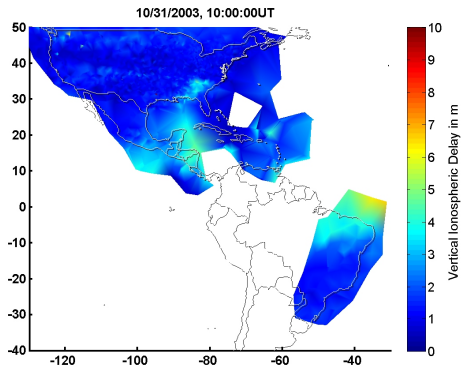

(f) 10:00 UT

Figure B.10: 31 October 2003, 00:00–10:00 UT.

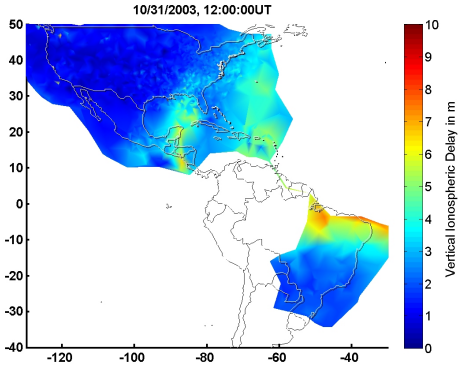

(g) 12:00 UT

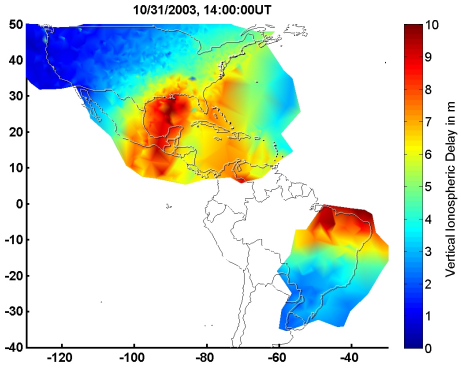

(h) 14:00 UT

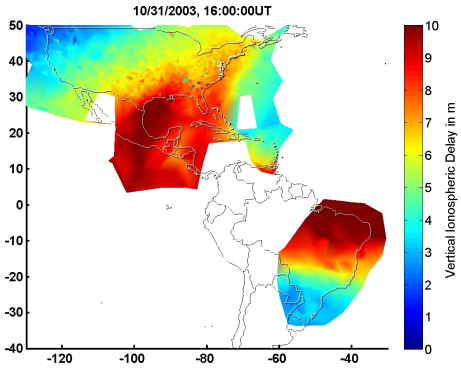

(i) 16:00 UT

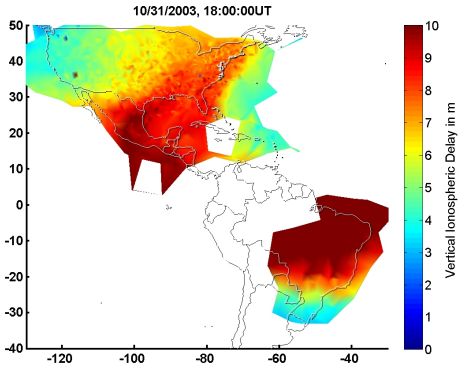

(j) 18:00 UT

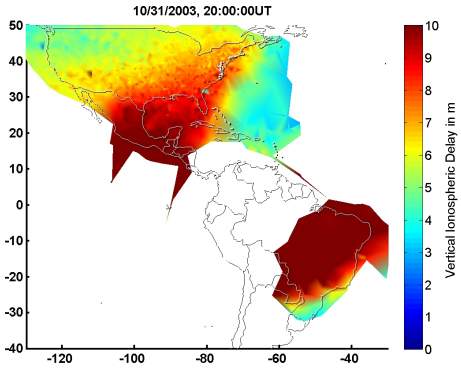

(k) 20:00 UT

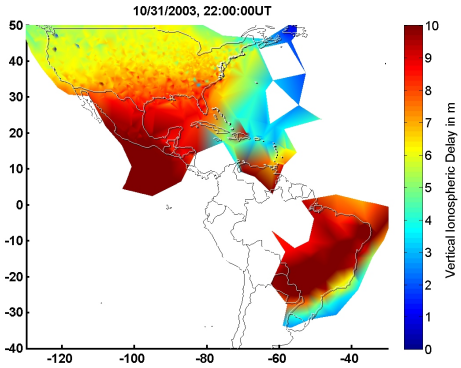

(l) 22:00 UT

Figure B.10: 31 October 2003, 12:00–22:00 UT.

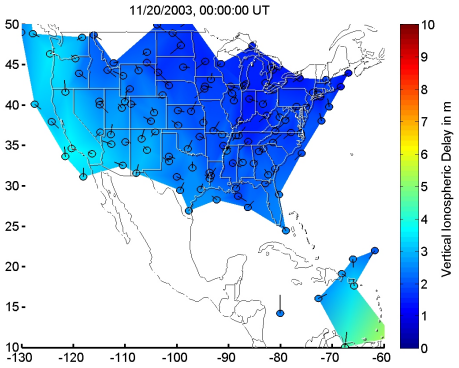

(a) 00:00 UT

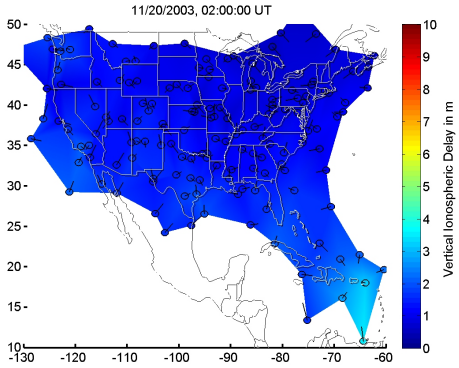

(b) 02:00 UT

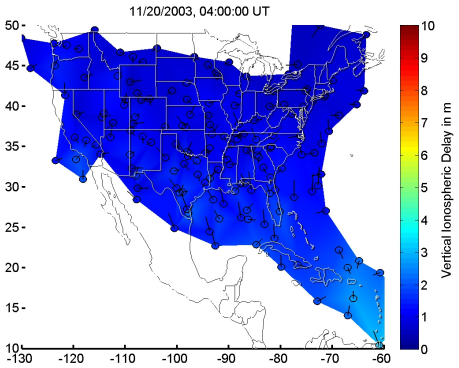

(c) 04:00 UT

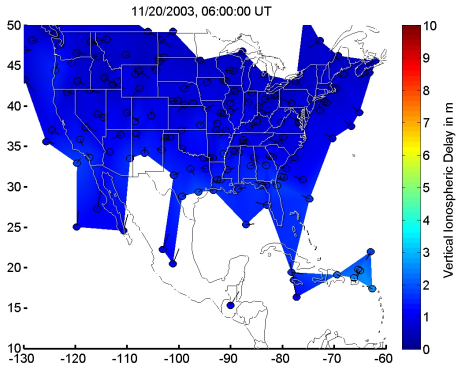

(d) 06:00 UT

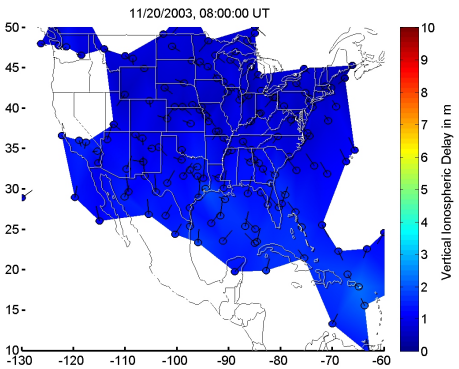

(e) 08:00 UT

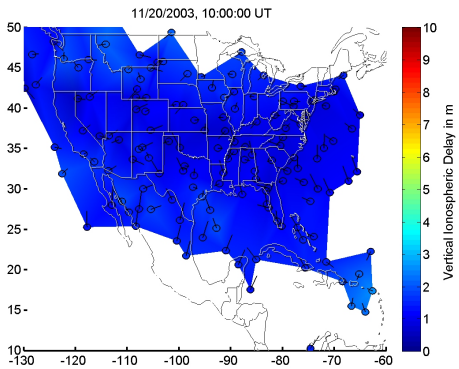

(f) 10:00 UT

Figure B.11: 20 November 2003, 00:00–10:00 UT.

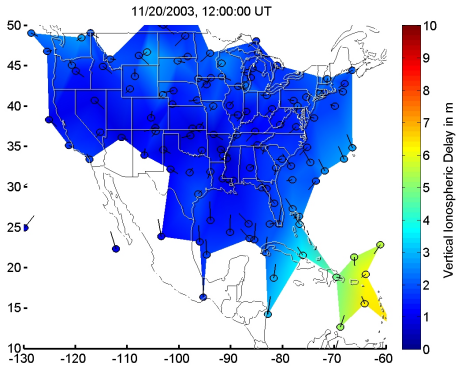

(g) 12:00 UT

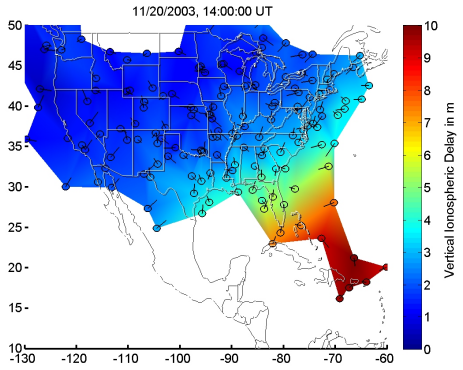

(h) 14:00 UT

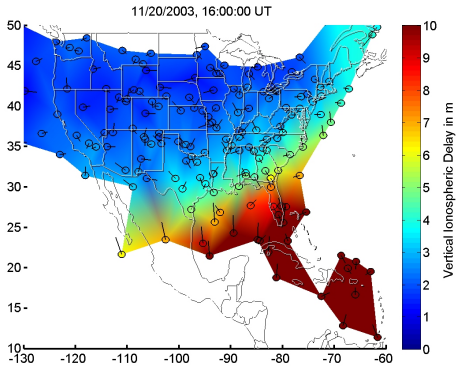

(i) 16:00 UT

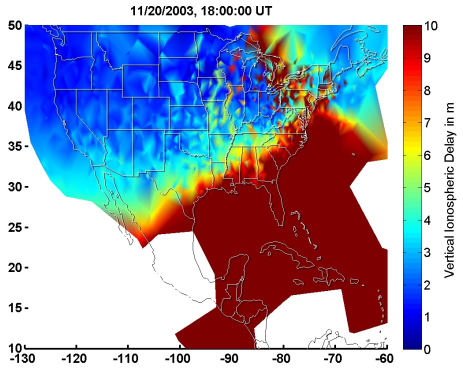

(j) 18:00 UT

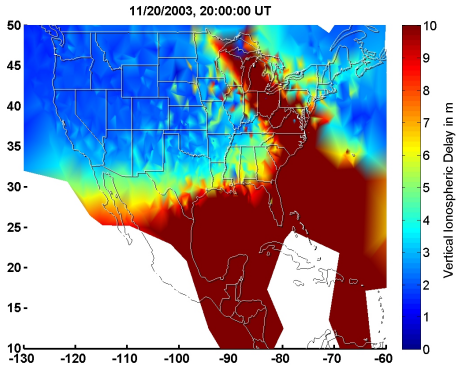

(k) 20:00 UT

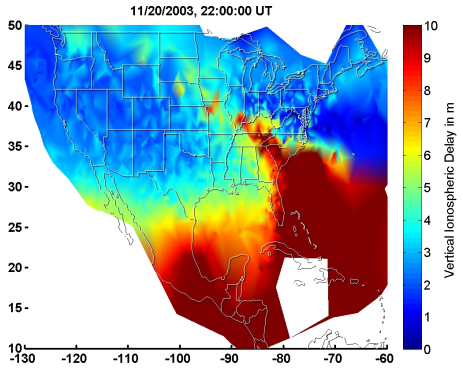

(l) 22:00 UT

Figure B.11: 20 November 2003, 12:00–22:00 UT. For Figures (j)–(l), CORS and IGS data were available and also plotted.

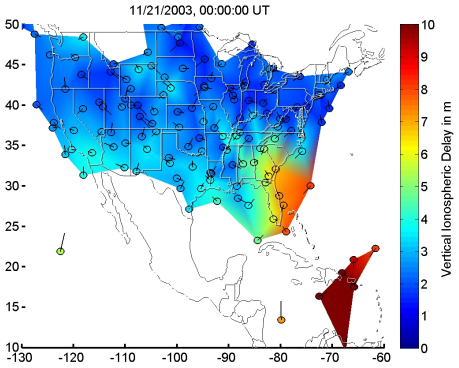

(a) 00:00 UT

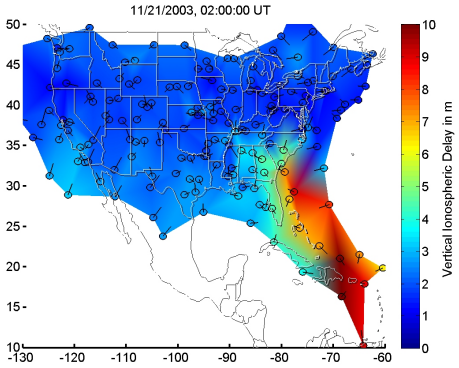

(b) 02:00 UT

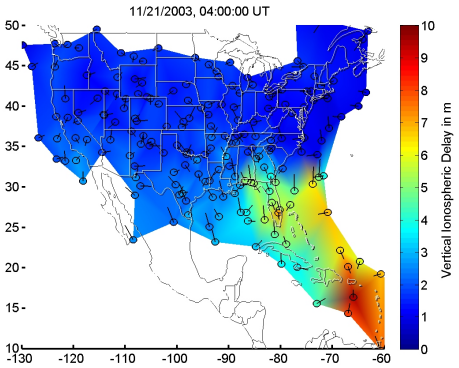

(c) 04:00 UT

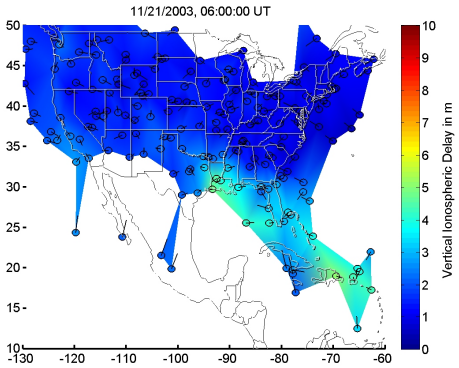

(d) 06:00 UT

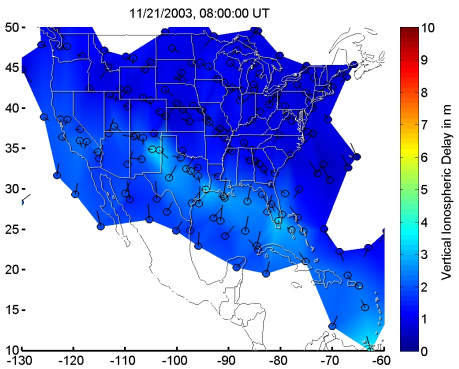

(e) 08:00 UT

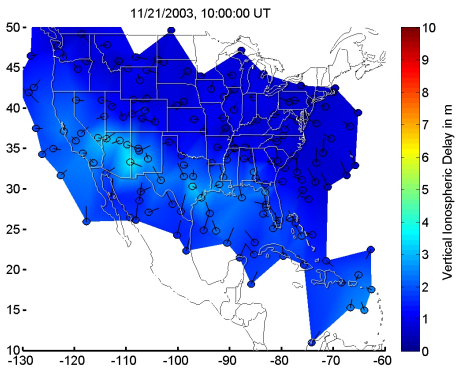

(f) 10:00 UT

Figure B.12: 21 November 2003, 00:00–10:00 UT.

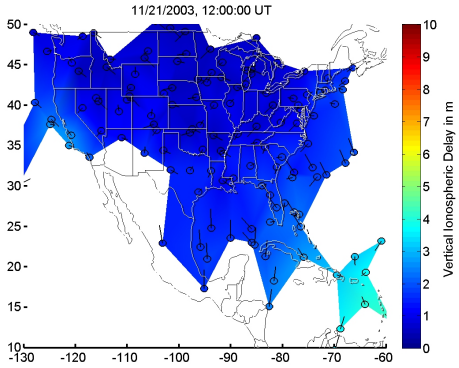

(g) 12:00 UT

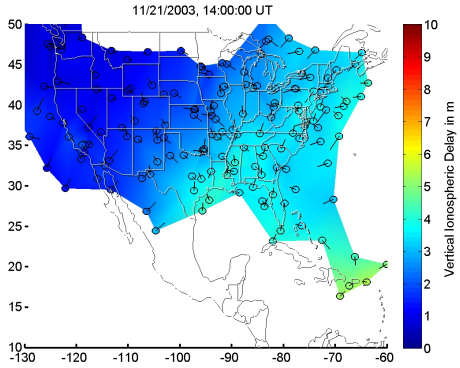

(h) 14:00 UT

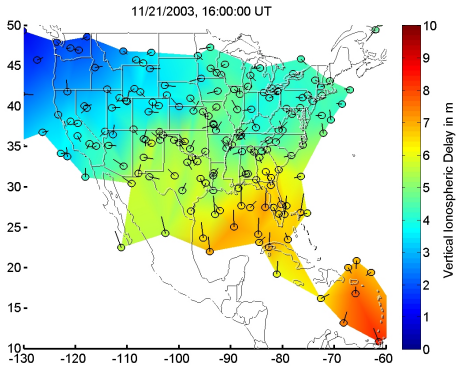

(i) 16:00 UT

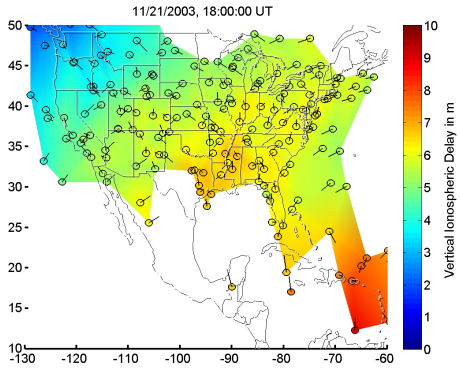

(j) 18:00 UT

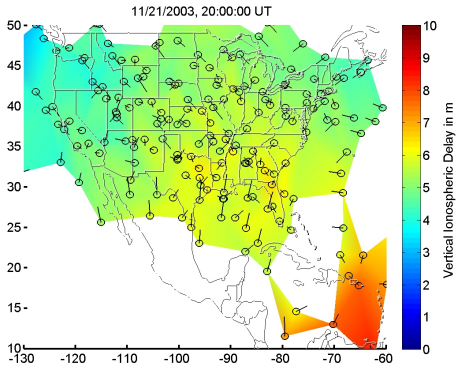

(k) 20:00 UT

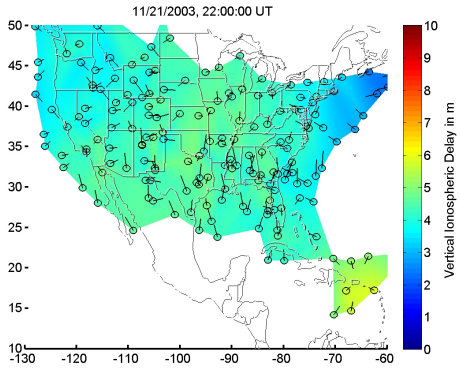

(l) 22:00 UT

Figure B.12: 21 November 2003, 12:00–22:00 UT.

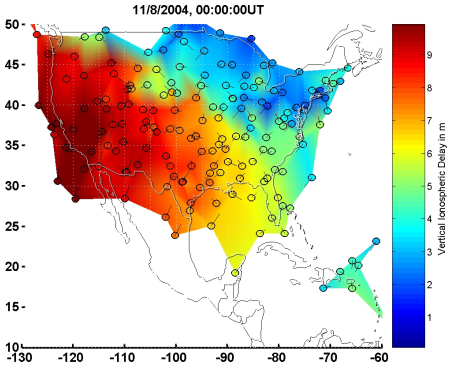

(a) 00:00 UT

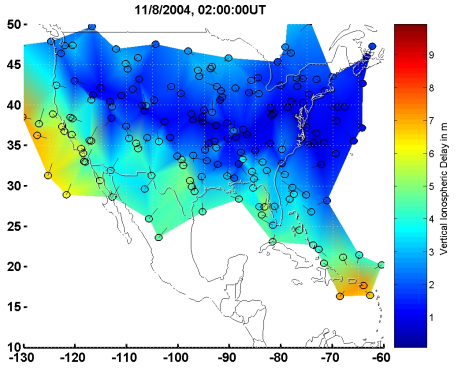

(b) 02:00 UT

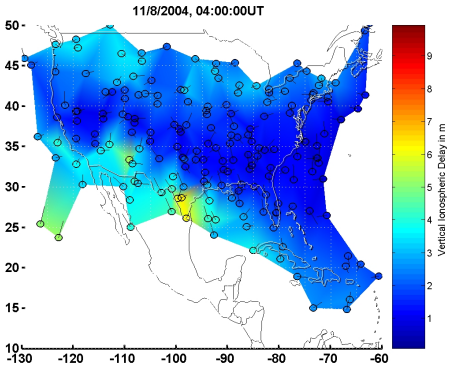

(c) 04:00 UT

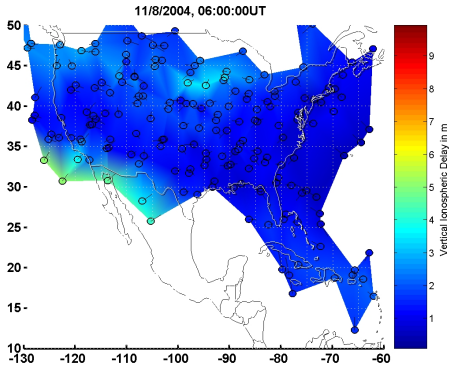

(d) 06:00 UT

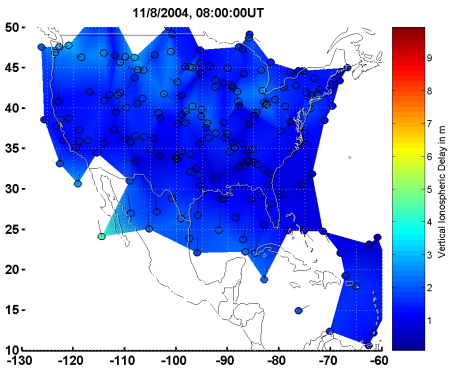

(e) 08:00 UT

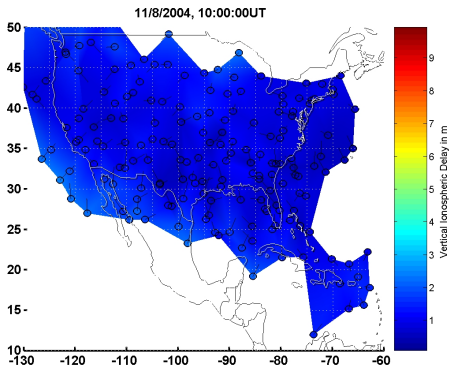

(f) 10:00 UT

Figure B.13: 8 November 2004, 00:00–10:00 UT.

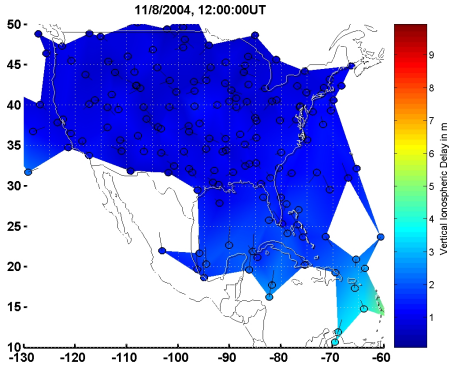

(g) 12:00 UT

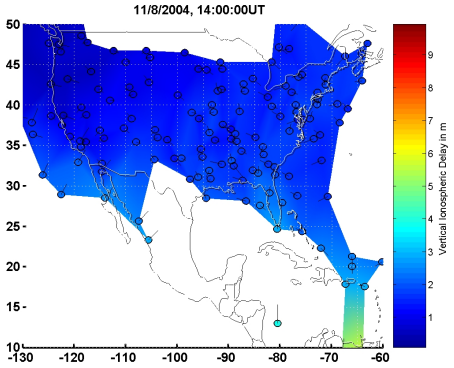

(h) 14:00 UT

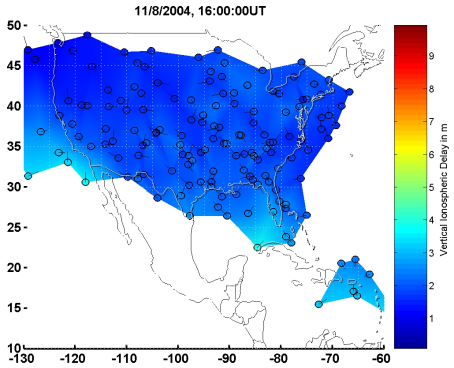

(i) 16:00 UT

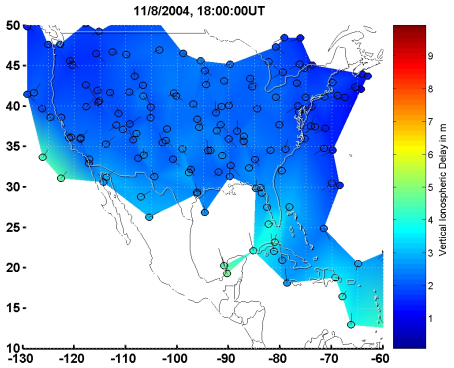

(j) 18:00 UT

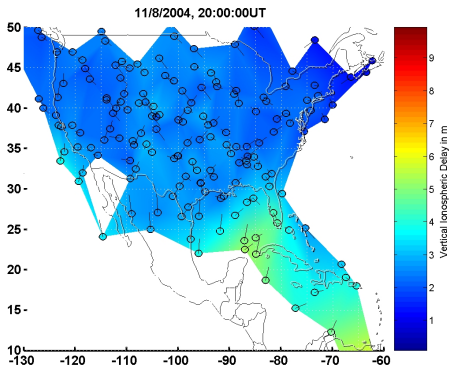

(k) 20:00 UT

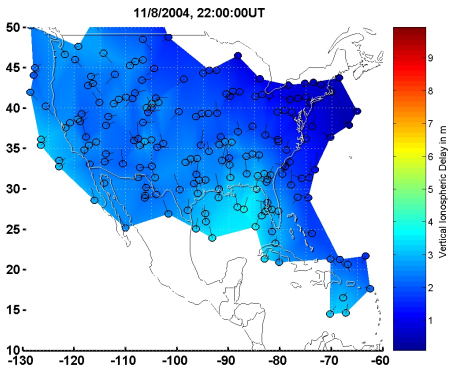

(l) 22:00 UT

Figure B.13: 8 November 2004, 12:00–22:00 UT.

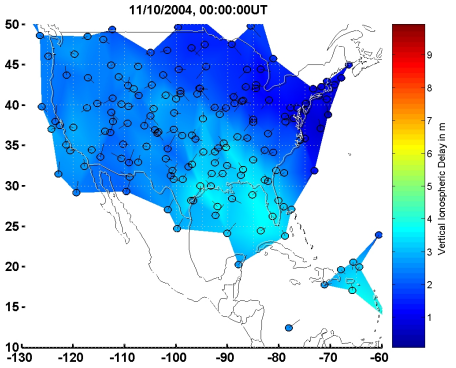

(a) 00:00 UT

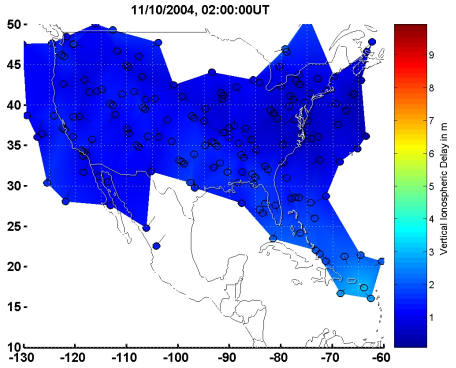

(b) 02:00 UT

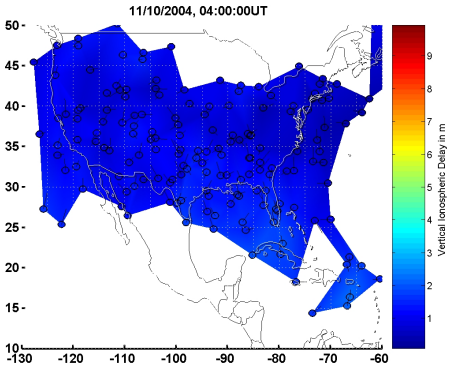

(c) 04:00 UT

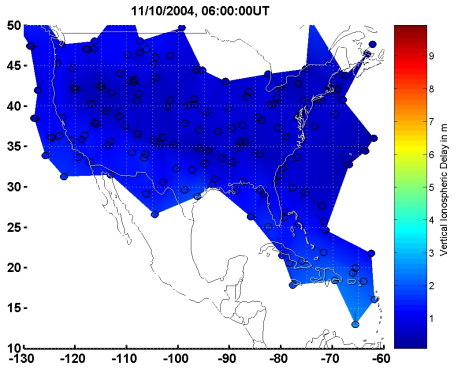

(d) 06:00 UT

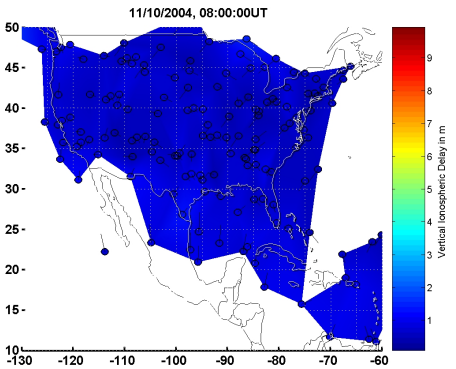

(e) 08:00 UT

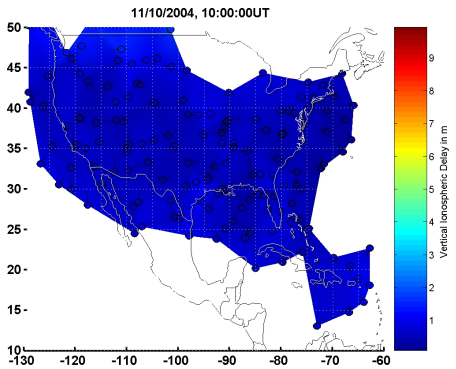

(f) 10:00 UT

Figure B.14: 10 November 2004, 00:00–10:00 UT.

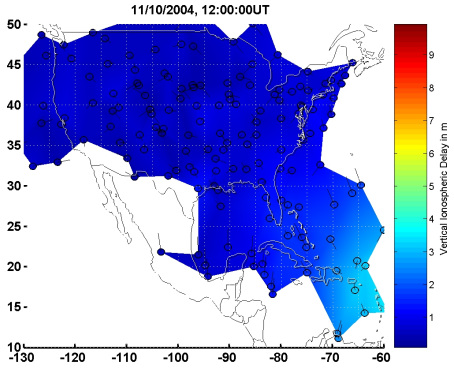

(g) 12:00 UT

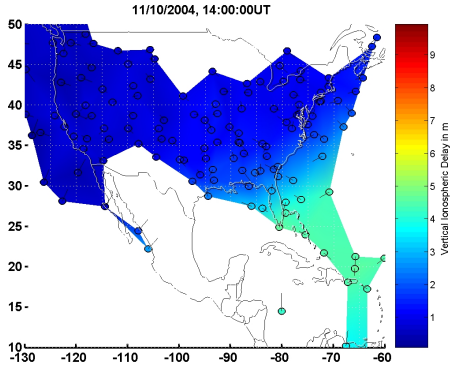

(h) 14:00 UT

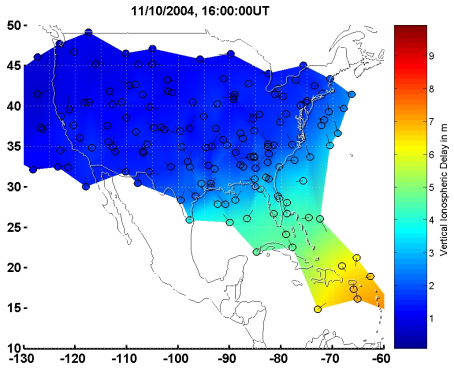

(i) 16:00 UT

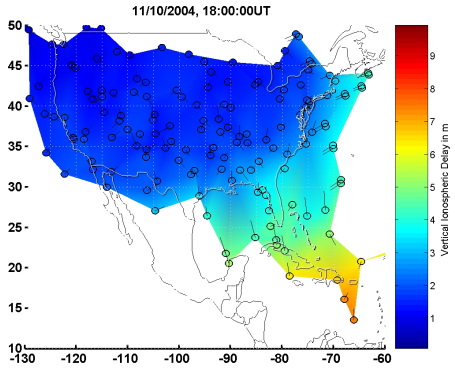

(j) 18:00 UT

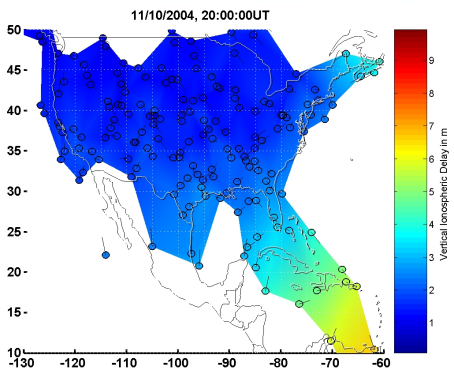

(k) 20:00 UT

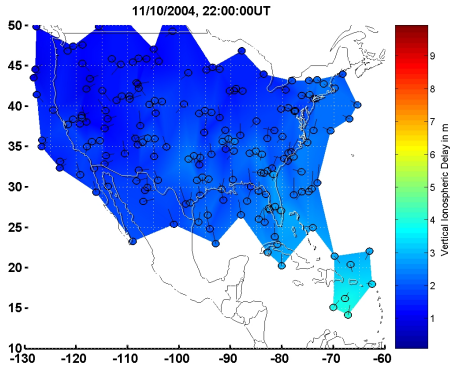

(l) 22:00 UT

Figure B.14: 10 November 2004, 12:00–22:00 UT.

Bibliography

[Alonso *et al.*, 2000] C. Alonso, R. Colomb, G. Comeyne, J. LaBrecque, A. Ocampo, and managers B. Wilson. Sac-c satellite. Fact Sheet FS-2000-11-012-GSFC, National Aeronautics and Space Administration Goddard Space Flight Center, Greenbelt, Maryland, 2000. accessed online 23 Oct 2007, http://www.nasa.gov/centers/goddard/about/fact_sheets.html#space.

[Balch *et al.*, 2004] C. Balch, D. Biesecker, L. Combs, M. Crown, K. Doggett, J. Kunches, H. Singer, and D. Zezula. Halloween space weather storms of 2003. Technical Memorandum OAR SEC-88, National Oceanic and Atmospheric Administration, Boulder, Colorado, June 2004. M. Weaver and William Murtagh, eds.

[Basu *et al.*, 2001] Su. Basu, S. Basu, C. E. Valladares, H.-C. Yeh, S.-Y. Su, E. MacKenzie, P. J. Sultan, J. Aarons, F. J. Rich, P. Doherty, K. M. Groves, and T. W. Bullett. Ionospheric effects of major magnetic storms during the international space weather period of september and october 1999: Gps observations, vhf/uhf scintillations, and in situ density structures at middle and equatorial latitudes. *J. Geophys. Res.*, 106(A12):30389–30414, 2001.

[Bilitza, 2001] D. Bilitza. International reference ionosphere 2000. *Radio Science*, 36(2):261–275, March/April 2001.

[Bittencourt, 2004] J. A. Bittencourt. *Fundamentals of Plasma Physics*. Springer, New York, 3rd edition, 2004.

[Brunner and Gu, 1991] F. K. Brunner and M. Gu. An improved model for the dual frequency ionospheric correction of gps observations. *Manuscripta Geodaetica*, 16:205–214, 1991.

[Buchau *et al.*, 1993] J. Buchau, T. W. Bullett, A. E. Ronn, K. D. Scro, and J. L. Carson. The digital ionospheric sounding system network of the u.s. air force air weather service. In *Proceedings of Session G6 at the XXIVth General Assembly of URSI* [1993]. accessed 13 July 2007, http://www.ips.gov.au/IPSHosted/INAG/uag-104/text/bullett1.html.

[Buonsanto, 1999] M. J. Buonsanto. Ionospheric storms — a review. *Space Science Reviews*, 88:563–601, 1999.

[Bust *et al.*, 2007] G. S. Bust, G. Crowley, T. W. Garner, T. L. Gaussiran II, R. W. Meggs, C. N. Mitchell, P. S. J. Spencer, P. Yin, and B. Zapfe. Four-dimensional gps imaging of space weather storms. *Space Weather*, 5(S02003), 2007.

[Campbell, 1996] W. H. Campbell. Geomagnetic storms, the dst ring-current myth and lognormal distributions. *Journal of Atmospheric and Terrestrial Physics*, 58(10):1171–1187, 1996.

[Carrano and Groves, 2007] C. Carrano and K. Groves. Effects of the december 2006 solar radio bursts on the gps receivers of the afrl-scinda network. In *Proceedings of the International Beacon Satellite Symposium* [2007].

[Cerruti, 2006] A. Cerruti. Observed gps and waas signal-to-noise degradation due to solar radio bursts. In ION GNSS [2006].

[Christie *et al.*, 1999] J. R. I. Christie, P.-Y. Ko, A. Hansen, D. Dai, S. Pullen, B. Pervan, and B. Parkinson. The effects of local ionospheric decorrelation on laas: Theory and expreimental results. In *Proceedings of the Institute of Navigation National Technical Meeting*, pages 769–777, 1999.

[Clinton, 1998] W. J. Clinton. Presidential decision directive/nsc-63: Critical infrastructure protection. Washington, D. C.: The White House, 1998.

[Coster *et al.*, 2003] A. Coster, J. Foster, and P. Erickson. Monitoring the ionosphere with gps: Space weather. *GPS World*, pages 42–49, May 2003.

[Daglis *et al.*, 1999] I. A. Daglis, R. M. Thorne, W. Baumjohann, and S. Orsini. The terrestrial ring current: Origin, formation, decay. *Rev. Geophys.*, 37(4):407–438, 1999.

[Datta-Barua *et al.*, 2006] S. Datta-Barua, T. Walter, J. Blanch, and P. Enge. Bounding higher order ionosphere errors for the dual frequency gps user. In ION GNSS [2006].

[Dehel *et al.*, 2004] T. Dehel, F. Lorge, and J. Warburton. Satellite navigation vs. the ionosphere: Where are we, and where are we going? In ION GNSS [2004], pages 375–386.

[Dehel, 2005] T. Dehel. Suspected relationship of tec change in a 'trough-like depletion' with prior measurements of o+ outflow. private correspondence, 16 May 2005.

[Doherty *et al.*, 2004] P. Doherty, S. Delay, T. Walter, T. McHugh, and D. Bunce. Space weather effects on waas: A performance and status report. In *Proceedings of the International Beacon Satellite Symposium*, 2004.

[Doherty, 2007] Patricia Doherty, editor. *Proceedings of the International Beacon Satellite Symposium*, Chestnut Hill, Massachusetts, 11–15 June 2007. Boston College.

[Dow *et al.*, 2005] J. M. Dow, R. E. Neilan, and G. Gendt. The international gps service (igs): Celebrating the 10th anniversary and looking to the next decade. *Adv. Space Res.*, 36(3):320–326, 2005.

[Eldridge, 2005] H. Eldridge. Storm days. private correspondence, 2 September 2005.

[Ene *et al.*, 2005] A. Ene, D. Qiu, M. Luo, S. Pullen, and P. Enge. A comprehensive ionosphere storm data analysis method to support laas threat model development. In *Proceedings of the Institute of Navigation National Technical Meeting*, pages 110–130, 2005.

[Enge *et al.*, 1996] P. Enge, T. Walter, S. Pullen, C. Kee, Y. C. Chao, and Y. J. Tsai. Wide area augmentation of the global positioning system. *Proceedings of the IEEE*, 84(8):1063–1088, August 1996.

[Enge, 1999] P. Enge. Local area augmentation of gps for the precision approach of aircraft. *Proceedings of the IEEE*, 87(1):111–132, January 1999.

[Feess and Stephens, 1987] W. A. Feess and S. G. Stephens. Evaluation of gps ionospheric model. *IEEE Transactions on Aerospace and Electronic Systems*, AES–23(3):332–338, 1987.

[Franke *et al.*, 2003] S. J. Franke, K. C. Yeh, E. S. Andreeva, and V. E. Kunitsyn. A study of the equatorial anomaly ionosphere using tomographic images. *Radio Science*, 38(1):1011, 2003.

[GIVE-ADD, 2001] GIVE-ADD. Algorithm description document for the grid ionospheric vertical error (give) monitor of the wide area augmentation system (give add). Technical Report CDRL Sequence No. A014–006, WAAS Integrity Performance Panel, El Segundo, California, 22 January 2001.

[Greenspan *et al.*, 1991] M. E. Greenspan, C. E. Rasmussen, W. J. Burke, and M. A. Abdu. Equatorial density depletions observed at 840 km during the great magnetic storm of march 1989. *J. Geophys. Res-Space Phys.*, 96(A8):13931–13942, 1991.

[Hansen *et al.*, 2000] A. Hansen, E. Peterson, T. Walter, and P. Enge. Correlation structure of ionospheric estimation and correlation for waas. In *Proceedings of the Institute of Navigation National Technical Meeting*. Institute of Navigation, 2000.

[Hansen, 2002] A. J. Hansen. *Tomographic Estimation of the Ionosphere Using Terrestrial GPS Sensors*. PhD thesis, Stanford University, March 2002.

[Hanson and Moffett, 1966] W. B. Hanson and R. J. Moffett. Ionization transport effects in the equatorial f region (continuity equation for electrons in f-2 layer obtained for region near geomagnetic equator at noon including photoionization, recombination, drift, etc). *J. Geophys. Res.*, 71:5559–5572, 1 December 1966.

[ICD-GPS-200C, 1993] ICD-GPS-200C. Navstar gps space segment / navigation user interface. Technical report, Arinc Research Corporation, El Segundo, California, 10 October 1993.

[ION GNSS, 2004] Institute of Navigation. *Proceedings of the Institute of Navigation GNSS Meeting*, Long Beach, California, 21–24 September 2004.

[ION GNSS, 2006] Institute of Navigation. *Proceedings of the Institute of Navigation GNSS Meeting*, Fort Worth, Texas, 26–29 September 2006.

[ION GPS/GNSS, 2003] Institute of Navigation. *Proceedings of the Institute of Navigation GPS/GNSS Meeting*, Portland, Oregon, 9–12 September 2003.

[ION NTM, 2004] Institute of Navigation. *Proceedings of the Institute of Navigation National Technical Meeting*, San Diego, California, 26–28 January 2004.

[Jackson, 1999] J. D. Jackson. *Classical Electrodynamics*. John Wiley & Sons, New York, 3rd edition, 1999.

[Jan, 2003] S.-S. Jan. *Aircraft Landing Using a Modernized Global Positioning System and the Wide Area Augmentation System*. PhD thesis, Stanford University, May 2003.

[Kelly and Davis, 1994] R. J. Kelly and J. M. Davis. Required navigation performance (rnp) for precision approach and landing gnss application. *Navigation, Journal of the Institute of Navigation*, 41(1), Spring 1994.

[Klobuchar and Kunches, 2000] J. A. Klobuchar and J. M. Kunches. Eye on the ionosphere: The spatial variability of ionospheric range delay. *GPS Solutions*, 3(3):70–74, 2000.

[Klobuchar *et al.*, 1993] J. A. Klobuchar, P. H. Doherty, and M. B. El-Arini. Potential ionospheric limitations to wide-area differential gps. In *Proceedings of ION GPS-93*, pages 1245–1254, Salt Lake City, Utah, September 1993. Institute of Navigation.

[Klobuchar, 1996] J. A. Klobuchar. Ionospheric effects on gps. In B. W. Parkinson and J. J. Spilker, editors, *Global Positioning System: Theory and Applications*, volume 1, chapter 12. American Institute of Aeronautics and Astronautics, Washington, D. C., 1996.

[Ko, 2000] P.-Y. Ko. *GPS-Based Precision Approach and Landing Navigation*. PhD thesis, Stanford University, Department of Aeronautics and Astronautics, May 2000.

[Komjathy *et al.*, 2002] A. Komjathy, L. Sparks, A. J. Mannucci, and X. Pi. An assessment of the current waas ionospheric correction algorithm in the south american region. In *Proceedings of the Institute of Navigation GPS Meeting*, pages 1286–1296. Institute of Navigation, 2002.

[Komjathy *et al.*, 2003] A. Komjathy, L. Sparks, A. J. Mannucci, and X. Pi. On the ionospheric impact of recent storm events on satellite-based augmentation systems in middle and low-latitude sectors. In ION GPS/GNSS [2003], pages 2769–2776.

[Komjathy, 2005] A. Komjathy. Automated daily processing of more than 1000 ground-based gps receivers for studying intense ionospheric storms. *Radio Science*, 40(RS6006), 2005.

[Kunches and Klobuchar, 2002] J. M. Kunches and J. A. Klobuchar. Eye on the ionosphere: Tracking geomagnetic storms. *GPS Solutions*, 5(3):94–95, 2002.

[Ledvina *et al.*, 2002] B. M. Ledvina, J. J. Makela, and P. M. Kintner. First observations of intense gps l1 amplitude scintillations at midlatitude. *Geophys. Res. Lett.*, 29(14):1659, 2002.

[Lee *et al.*, 2006a] J. Lee, M. Luo, S. Pullen, Y. S. Park, P. Enge, and M. Brenner. Position-domain geometry screening to maximize laas availability in the presence of ionosphere anomalies. In ION GNSS [2006], pages 393–408.

[Lee *et al.*, 2006b] J. Lee, S. Pullen, S. Datta-Barua, and P. Enge. Assessment of nominal ionosphere spatial decorrelation for laas. In *Proceedings of the Position Location and Navigation Symposium*. Institute of Navigation/ Institute of Electronics and Electrical Engineers, 2006.

[Lee, 2005] J. Lee. *GPS-Based Aircraft Landing Systems with Enhanced Performance Beyond Accuracy*. PhD thesis, Stanford University, Department of Aeronautics and Astronautics, March 2005.

[Liemohn *et al.*, 2001] M. W. Liemohn, J. U. Kozyra, M. F. Thomsen, J. L. Roeder, G. Lu, J. E. Borovsky, and T. E. Cayton. Dominant role of the asymmetric ring current in producing the stormtime dst*. *J. Geophys. Res.*, 106(A6):10883–10904, 2001.

[Luo *et al.*, 2003] M. Luo, S. Pullen, J. Dennis, H. Konno, G. Xie, T. Walter, S. Datta-Barua, and T. Dehel. Laas ionosphere spatial gradient threat model and impact of lgf and airborne monitoring. In ION GPS/GNSS [2003], pages 2255–2274.

[Luo *et al.*, 2004a] M. Luo, S. Pullen, A. Ene, D. Qiu, T. Walter, and P. Enge. Ionosphere threat to laas: Updated model, user impact, and mitigations. In ION GNSS [2004], pages 2771–2785.

[Luo *et al.*, 2004b] M. Luo, S. Pullen, T. Walter, and P. Enge. Ionosphere spatial gradient threat for laas: Mitigation and tolerable threat space. In ION NTM [2004], pages 490–501.

[Mannucci *et al.*, 2005] A. J. Mannucci, B. T. Tsurutani, B. A. Iijima, A. Komjathy, A. Saito, W. D. Gonzalez, F. L. Guarnieri, J. U. Kozyra, and R. Skoug. Dayside global ionospheric response to the major interplanetary events of october 29–30, 2003 halloween storms. *Geophys. Res. Lett.*, 32(L12S02), 2005.

[Misra and Enge, 2006] P. Misra and P. Enge. *Global Positioning System: Signals, Measurements, and Performance*. Ganga-Jamuna Press, Lincoln, Massachusetts, 2nd edition, 2006.

[National Geophysical Data Center, 2005] National Geophysical Data Center. Space physics interactive data resource. online, 2005. accessed 1 March, http://spidr.ngdc.noaa.gov/spidr/.

[Novatel, 1997] Inc. Novatel. Waas/gus receiver subsystem. Installation and Operation Manual OM–20000015, Novatel, Inc., 18 November 1997. Revision Level 2.0.

[NSTB/WAAS Test and Evaluation Team, 2003] NSTB/WAAS Test and Evaluation Team. Wide-area augmentation system performance analysis report. Technical Report 6, FAA/William J. Hughes Technical Center, Atlantic City, New Jersey, 31 October 2003. ftp://ftp.nstb.tc.faa.gov/pub/archive/REPORTS/waaspan6.pdf.

[NSTB/WAAS Test and Evaluation Team, 2004a] NSTB/WAAS Test and Evaluation Team. Wide-area augmentation system performance analysis report. Technical Report 7, FAA/William J. Hughes Technical Center, Atlantic City, New Jersey, 30 January 2004. ftp://ftp.nstb.tc.faa.gov/pub/archive/REPORTS/waaspan7.pdf.

[NSTB/WAAS Test and Evaluation Team, 2004b] NSTB/WAAS Test and Evaluation Team. Wide-area augmentation system performance analysis report. Technical Report 8, FAA/William J. Hughes Technical Center, Atlantic City, New Jersey, May 2004. ftp://ftp.nstb.tc.faa.gov/pub/archive/REPORTS/waaspan8.pdf.

[NSTB/WAAS Test and Evaluation Team, 2004c] NSTB/WAAS Test and Evaluation Team. Wide-area augmentation system performance analysis report. Technical Report 9, FAA/William J. Hughes Technical Center, Atlantic City, New Jersey, August 2004. ftp://ftp.nstb.tc.faa.gov/pub/archive/REPORTS/waaspan9.pdf.

[NSTB/WAAS Test and Evaluation Team, 2004d] NSTB/WAAS Test and Evaluation Team. Wide-area augmentation system performance analysis report. Technical Report 10, FAA/William J. Hughes Technical Center, Atlantic City, New Jersey, November 2004. ftp://ftp.nstb.tc.faa.gov/pub/archive/REPORTS/waaspan10.pdf.

[Pandya *et al.*, 2007] N. Pandya, M. Gran, and E. Paredes. Waas performance improvement with a new undersampled ionospheric gradient threat model. In *Proceedings of the Institute of Navigation National Technical Meeting*, pages 291–304, 2007.

[Park *et al.*, 2007] Y. S. Park, J. Lee, M. Luo, S. Pullen, and P. Enge. Data-replay analysis of laas safety during ionosphere storms. In *Proceedings of the Institute of Navigation GNSS Meeting*, 2007. in publication.

[Pervan, 1996] B. S. Pervan. *Navigation Integrity for Aircraft Precision Landing Using the Global Positioning System.* PhD thesis, Stanford University, Department of Aeronautics and Astronautics, 1996.

[Pullen *et al.*, 1998] S. Pullen, G. Opshaug, A. Hansen, T. Walter, P. Enge, and B. Parkinson. A preliminary study of the effect of ionospheric scintillation on waas user availability in equatorial regions. In *Proceedings of ION GPS 1998*, Nashville, TN, 15–18 September 1998.

[Rajagopal *et al.*, 2004] S. Rajagopal, T. Walter, S. Datta-Barua, J. Blanch, and T. Sakai. Correlation structure of the equatorial ionosphere. In ION NTM [2004], pages 542–550.

[Reinisch, 1986] B. W. Reinisch. New techniques in ground based ionospheric sounding and studies. *Radio Science*, 21:331–341, 1986.

[Reinisch, 1993] B. W. Reinisch. The digisonde network and databasing. In *Proceedings of Session G6 at the XXIVth General Assembly of URSI* [1993]. accessed 13 July 2007, http://www.ips.gov.au/IPSHosted/INAG/uag-104/text/bodo.html.

[Schunk and Nagy, 2000] R. W. Schunk and A. Nagy. *Ionospheres: Physics, Plasma Physics, and Chemistry.* Cambridge University Press, New York, 2000.

[Seo *et al.*, 2007] J. Seo, T. Walter, E. Marks, and P. Enge. Ionospheric scintillation effects on gps receivers in brazil during solar minimum. In *Proceedings of the International Beacon Satellite Symposium* [2007].

[Sparks *et al.*, 2001] L. Sparks, X. Pi, and A. J. Mannucci et al. The waas ionospheric threat model. In *Proceedings of the International Beacon Satellite Symposium*, pages 237–241, 2001.

[Sparks *et al.*, 2005] L. Sparks, A. Komjathy, A. J. Mannucci, E. Altshuler, T. Walter, J. Blanch, M. B. El-Arini, and R. Lejeune. Extreme ionospheric storms and their impact on waas. In *Proceedings of the Ionospheric Effects Symposium*, pages 4A2–1–4A2–9, 2005.

[Sugiura and Kamei, 1991] M. Sugiura and T. Kamei. Equatorial dst index 1957–1986. IAGA Bulletin 40, ISGI Publications Office, Saint-Maur-des-Fosses, France, 1991. accessed 4 December 2007, http://cdaw.gsfc.nasa.gov/geomag_cdaw/data/cdaw4/McPherronReferences/ SugiuraKamei_Dst_Derivation.pdf.

[Takalo and Mursula, 2001] J. Takalo and K. Mursula. A model for the diurnal universal time variation of the dst index. *J. Geophys. Res.*, 106(A6):10905–10914, 2001.

[Tascione, 1994] T. F. Tascione. *Introduction to the Space Environment*. Krieger Publishing Company, Malabar, Florida, 1994.

[Tsurutani *et al.*, 2004] B. T. Tsurutani, A. J. Mannucci, B. A. Iijima, M. A. Abdu, J. H. A. Sobral, W. D. Gonzalez, F. L. Guranieri, T. Tsuda, A. Saito, K. Yumoto, B. G. Fejer, T. Fuller-Rowell, J. U. O. Kozyra, J. C. Foster, A. J. Coster, and V. M. Vasyliunas. Global dayside ionospheric uplift and enhancement associated with interplanetary /electric fields. *J. Geophys. Res.*, 109(A08302), 2004.

[Verkhoglyadova *et al.*, 2006] O. P. Verkhoglyadova, B. T. Tsurutani, A. J. Mannucci, T. Araki, A. Saito, T. Tsuda, and K. Yumoto. O+ uplift and satellite drag effects during the october 30, 2003 daytime superfountain event. submitted to Geophysical Research Letters, 2006.

[Walt, 1994] M. Walt. *Introduction to Geomagnetically Trapped Radiation*. Cambridge University Press, New York, 1994.

[Walter *et al.*, 2000] T. Walter, A. Hansen, J. Blanch, P. Enge, A. J. Mannucci, X. Pi, L. Sparks, B. Ijima, B. El-Arini, R. Lejeune, M. Hagen, E. Altshuler, R. Fries, and A. Chu. Robust detection of ionospheric irregularities. In *Proceedings of the Institute of Navigation GPS Meeting*, pages 209–218, 2000.

[Walter *et al.*, 2004] T. Walter, S. Datta-Barua, J. Blanch, and P. Enge. The effects of large ionospheric gradients on single frequency airborne smoothing filters for waas and laas. In ION NTM [2004], pages 103–109.

[Wilkinson, 1993] Phil Wilkinson, editor. *Proceedings of the XXIVth General Assembly*, Kyoto, Japan, 25 August – 2 September 1993. International Union of Radio Scientists (URSI).

[Wilson *et al.*, 1999] B. D. Wilson, C. H. Yinger, W. A. Feess, and C. Shank. New and improved: The broadcast interfrequency biases. *GPS World*, pages 56–66, September 1999.

[Yin and Mitchell, 2005] P. Yin and C. Mitchell. Gps imaging showing the vertical dynamics of the storm-time ionosphere over europe and the usa. In *Proceedings of the Institute of Navigation Annual Meeting*, pages 417–424, 2005.